

**ISTANBUL TECHNICAL UNIVERSITY ★ GRADUATE SCHOOL OF SCIENCE**  
**ENGINEERING AND TECHNOLOGY**

**ADVANCED CONTROL SYSTEMS FOR GROUND VEHICLES**

**Ph.D. THESIS**

**Mümin Tolga EMİRLER**

**Department of Mechanical Engineering**

**Mechanical Engineering Programme**

**NOVEMBER 2014**



**ISTANBUL TECHNICAL UNIVERSITY ★ GRADUATE SCHOOL OF SCIENCE**  
**ENGINEERING AND TECHNOLOGY**

**ADVANCED CONTROL SYSTEMS FOR GROUND VEHICLES**

**Ph.D. THESIS**

**Mümin Tolga EMİRLER**  
**(503092042)**

**Department of Mechanical Engineering**

**Mechanical Engineering Programme**

**Thesis Advisor: Prof. Dr. Bilin AKSUN GÜVENÇ**

**NOVEMBER 2014**



**İSTANBUL TEKNİK ÜNİVERSİTESİ ★ FEN BİLİMLERİ ENSTİTÜSÜ**

**YOL TAŞITLARI İÇİN İLERİ KONTROL SİSTEMLERİ**

**DOKTORA TEZİ**

**Mümin Tolga EMİRLER  
(503092042)**

**Makina Mühendisliği Anabilim Dalı**

**Makina Mühendisliği Programı**

**Tez Danışmanı: Prof. Dr. Bilin AKSUN GÜVENÇ**

**KASIM 2014**



**Mümin Tolga EMİRLER**, a Ph.D. student of ITU Graduate School of Science Engineering and Technology 503092042 successfully defended the thesis entitled “**ADVANCED CONTROL SYSTEMS FOR GROUND VEHICLES**”, which he/she prepared after fulfilling the requirements specified in the associated legislations, before the jury whose signatures are below.

**Thesis Advisor :**     **Prof. Dr. Bilin AKSUN GÜVENÇ**     .....  
Istanbul Technical University

**Jury Members :**     **Assoc. Prof. Dr. Erdinç ALTUĞ**     .....  
Istanbul Technical University

**Prof. Dr. Haluk KÜÇÜK**     .....  
Marmara University

**Prof. Dr. Levent GÜVENÇ**     .....  
The Ohio State University

**Assoc. Prof. Dr. ÖZGEN AKALIN**     .....  
Istanbul Technical University

**Date of Submission :**    **24 September 2014**

**Date of Defense :**     **25 November 2014**



*To my family,*



## FOREWORD

First of all, I would like to thank my advisor Prof. Bilin Aksun Güvenç for her continued support, encouragement and guidance. She opened the doors to many opportunities for me, both academically and professionally. Also, I am grateful to Prof. Levent Güvenç who has contributed to my academic progress with numerous comments and suggestions.

I would also like to thank my monitoring committee, Prof. Erdinç Altuğ and Prof. Haluk Küçük, for taking their time to critique this thesis. Thanks also to Prof. Levent Güvenç and Prof. Özgen Akalın for accepting to be on my defense committee and reviewing my thesis.

I thank all the members of Mechatronics Research (Mekar) Labs, past and present; especially Prof. Ümit Sönmez, Burak Demirel, İsmail Meriç Can Uygan, İlker Altay, Kerim Kahraman and Mutlu Şentürk for their support, help and joint works over the years. I truly enjoyed the times I spent with many great friends here at Mekar Labs.

I would like to thank TÜBİTAK (The Scientific and Technological Research Council of Turkey) 2211 National Scholarship Programme to support my PhD works.

As always, my biggest debt is to my parents, who encouraged me to continue my journey in science and engineering, and have always been there to support me. I would also like to thank my brother Mert for their love and support in all the notable moments of my life.

September 2014

Mümin Tolga EMİRLER  
(Mechanical Engineer)



## TABLE OF CONTENTS

	<u>Page</u>
<b>FOREWORD</b> .....	ix
<b>TABLE OF CONTENTS</b> .....	xi
<b>ABBREVIATIONS</b> .....	xv
<b>LIST OF TABLES</b> .....	xvii
<b>LIST OF FIGURES</b> .....	xix
<b>SUMMARY</b> .....	xxiii
<b>ÖZET</b> .....	xxv
<b>1. INTRODUCTION</b> .....	1
<b>2. PARAMETER SPACE APPROACH BASED ROBUST PI DC MOTOR SPEED CONTROL AND PERFORMANCE IMPROVEMENTS USING DISTURBANCE OBSERVER</b> .....	7
2.1 Introduction .....	7
2.2 DC Motor Modeling and Uncertainties .....	9
2.3 Design Methodology by Mapping Multi-Objective Requirements into Parameter Space .....	11
2.3.1 Hurwitz stability .....	12
2.3.2 D-stability .....	13
2.3.3 Phase margin.....	14
2.3.4 Mapping mixed sensitivity (frequency domain) bounds .....	14
2.3.5 Application to robust PI DC motor speed control .....	17
2.4 Improvements on System Response using Disturbance Observer .....	20
2.4.1 Add-on disturbance observer structure.....	20
2.4.2 Disturbance observer design.....	23
2.5 Simulation Results .....	24
2.6 Experiments .....	25
2.6.1 Experimental set-up .....	25
2.6.2 Experimental results .....	27
2.7 Conclusion.....	27
<b>3. TIME DELAY COMPENSATION USING COMMUNICATION DISTURBANCE OBSERVER APPROACH AND ITS AUTOMOTIVE CONTROL APPLICATION</b> .....	29
3.1 Introduction .....	29
3.2 Communication Disturbance Observer Structure.....	30
3.2.1 Classical disturbance observer for disturbance estimation.....	31
3.2.2 Network disturbance concept .....	31
3.2.3 Communication disturbance observer .....	32

3.3 Communication Disturbance Observer based Time Delayed Integral Plant Control.....	33
3.4 Robust Stability Analysis in the case of Constant Time Delay .....	35
3.5 Robust Stability Analysis in the case of Bounded Time Varying Delay .....	38
3.6 Application to Yaw Stability Control over CAN Bus.....	40
3.7 Conclusion.....	45
<b>4. ROBUST PID STEERING CONTROL IN PARAMETER SPACE FOR HIGHLY AUTOMATED DRIVING.....</b>	<b>47</b>
4.1 Introduction .....	47
4.2 Vehicle Models and Model Validation .....	48
4.2.1 Vehicle steering model .....	48
4.2.2 Nonlinear vehicle model.....	50
4.2.3 Model validation.....	53
4.3 Robust PID Steering Controller Design using The Parameter Space Approach .....	55
4.3.1 Mapping D-stability requirements into the parameter space .....	55
4.3.2 Application to automatic steering control .....	56
4.4 Simulation Studies.....	58
4.5 Digital Map and GPS Measurements based Robust PID Steering Control....	60
4.5.1 High resolution digital map generation .....	61
4.5.2 Lateral deviation and yaw angle error calculations .....	64
4.5.3 Simulation results .....	66
4.6 Conclusion.....	67
<b>5. LATERAL STABILITY CONTROL OF FULLY ELECTRIC VEHICLES 69</b>	<b>69</b>
5.1 Introduction .....	69
5.2 ILSC System Structure .....	70
5.2.1 Desired value generation .....	72
5.2.2 Corrective yaw moment calculation based on scheduled LQR control..	73
5.2.3 Braking torque distribution algorithm .....	75
5.2.4 Electric motor torque reduction algorithm .....	77
5.2.5 Wheel slip controller .....	78
5.2.5.1 Slip ratio calculation .....	79
5.2.5.2 Desired slip ratio calculation based on scheduled LQR control.....	79
5.2.5.3 Hydraulic brake actuator model for calculation of tire brake pressures .....	80
5.3 RB-LSC System Structure.....	81
5.3.1 Bang-bang control based algorithm (RB-LSC1).....	81
5.3.2 PD control based algorithm (RB-LSC2) .....	82
5.4 Simulations .....	82
5.4.1 ILSC system simulation results .....	83
5.4.2 RB-LSC system simulation results.....	84
5.4.3 FMVSS No. 126 test simulation results .....	87
5.5 Conclusion.....	89
<b>6. CONCLUSIONS AND RECOMMENDATIONS.....</b>	<b>91</b>
<b>REFERENCES.....</b>	<b>95</b>

**CURRICULUM VITAE..... 104**



## ABBREVIATIONS

<b>4WD</b>	: Four Wheel Drive
<b>A/D</b>	: Analog to Digital
<b>ABS</b>	: Anti-lock Braking System
<b>ACC</b>	: Adaptive Cruise Control
<b>CA</b>	: Collision Avoidance
<b>CACC</b>	: Cooperative Adaptive Cruise Control
<b>CAN</b>	: Controller Area Network
<b>CDOB</b>	: Communication Disturbance Observer
<b>CG</b>	: Center of Gravity
<b>CRB</b>	: Complex Root Boundary
<b>CW</b>	: Collision Warning
<b>D/A</b>	: Digital to Analog
<b>DC</b>	: Direct Current
<b>DOB</b>	: Disturbance Observer
<b>EMF</b>	: Electromotive Force
<b>ESC</b>	: Electronic Stability Control
<b>FMVSS</b>	: Federal Motor Vehicle Safety Standards
<b>FPGA</b>	: Field Programmable Gate Array
<b>GNP</b>	: Gross National Product
<b>GPS</b>	: Global Positioning System
<b>ICE</b>	: Internal Combustion Engine
<b>ILSC</b>	: Integrated Lateral Stability Control
<b>IMU</b>	: Inertial Measurement Unit
<b>INS</b>	: Inertial Navigation System
<b>IRB</b>	: Infinite Root Boundary
<b>ISF</b>	: Input Shaping Filter
<b>LDW</b>	: Lane Departure Warning
<b>LKA</b>	: Lane Keeping Assistance
<b>LMI</b>	: Linear Matrix Inequality
<b>LQR</b>	: Linear Quadratic Regulator
<b>NHTSA</b>	: National Highway Traffic Safety Administration
<b>OPTC</b>	: Optimal Precision Tracking Control
<b>PM</b>	: Phase Margin
<b>PTC</b>	: Precision Tracking Control
<b>R&amp;D</b>	: Research and Development
<b>RB-LSC</b>	: Regenerative Braking based Lateral Stability Control
<b>RRB</b>	: Real Root Boundary
<b>TCS</b>	: Traction Control System
<b>V2V</b>	: Vehicle to Vehicle
<b>ZPETC</b>	: Zero Phase Error Precision Tracking Control



## LIST OF TABLES

	<u>Page</u>
<b>Table 2.1</b> : The nominal parameters of the DC motor.....	11
<b>Table 2.2</b> : Closed loop pole locations and phase margin values for four vertices of the uncertainty box.....	20
<b>Table 5.1</b> : Different cases for braking torque distribution algorithm.....	76
<b>Table 5.2</b> : Comparison of the ILSC and RB-LSC systems according to the sensor, estimator and actuator usage.....	86
<b>Table 5.3</b> : Comparison of the proposed systems according to the error values. ...	87
<b>Table 5.4</b> : Comparison of the Basic ESC and ILSC systems according to FMVSS No. 126 test.....	89



## LIST OF FIGURES

	<u>Page</u>
<b>Figure 2.1</b> : The DC motor scheme.....	10
<b>Figure 2.2</b> : The open loop block diagram of the DC motor with torque disturbance.....	10
<b>Figure 2.3</b> : Uncertainty box for the DC motor parameters.....	11
<b>Figure 2.4</b> : The PI controlled closed system block diagram.....	12
<b>Figure 2.5</b> : D-stable region in the complex plane.....	13
<b>Figure 2.6</b> : The point condition for mixed sensitivity.....	15
<b>Figure 2.7</b> : Detailed view of D-stability and phase margin boundaries in parameter space for P1.....	17
<b>Figure 2.8</b> : Solutions for P1 where $k_{m,\min} = 0.0402$ , $J_{\min} = 17.68 \times 10^{-6}$ (Blue: D-stability boundary, Red: PM boundaries, Green: Mixed sens. req. boundaries).....	18
<b>Figure 2.9</b> : Solutions for P2 point where $k_{m,\max} = 0.0602$ , $J_{\min} = 17.68 \times 10^{-6}$ .	19
<b>Figure 2.10</b> : Solutions for P3 point where $k_{m,\max} = 0.0602$ , $J_{\max} = 26.52 \times 10^{-6}$ .	19
<b>Figure 2.11</b> : Solutions for P4 point where $k_{m,\min} = 0.0402$ , $J_{\max} = 26.52 \times 10^{-6}$ .	19
<b>Figure 2.12</b> : Robust performance plots $ W_S S  +  W_T T $ .....	20
<b>Figure 2.13</b> : The system structure with add-on disturbance observer.....	21
<b>Figure 2.14</b> : Stability robustness plot.....	24
<b>Figure 2.15</b> : Step response and step disturbance rejection simulation results. ....	25
<b>Figure 2.16</b> : Step response and ramp disturbance rejection simulation results. ....	25
<b>Figure 2.17</b> : Experimental setup. ....	26
<b>Figure 2.18</b> : Schematic diagram of the experimental setup.....	26
<b>Figure 2.19</b> : Trajectory tracking experiment result.....	27
<b>Figure 2.20</b> : Step disturbance rejection experiment result.....	28
<b>Figure 2.21</b> : Ramp disturbance rejection experiment result. ....	28
<b>Figure 3.1</b> : Classical disturbance observer for disturbance estimation.....	31
<b>Figure 3.2</b> : Network disturbance concept. ....	32
<b>Figure 3.3</b> : Communication disturbance observer structure. ....	33
<b>Figure 3.4</b> : Equivalent block diagram transformation. ....	34
<b>Figure 3.5</b> : Step response of the time delayed integral plant without/with communication disturbance observer.....	35
<b>Figure 3.6</b> : Step responses of the time delayed integral plant for different delay values.....	36
<b>Figure 3.7</b> : Nyquist plots for different cutoff frequencies $\omega_c$ of $Q(s)$ . ....	36
<b>Figure 3.8</b> : Feedback controlled plant with multiplicative uncertainty.....	37
<b>Figure 3.9</b> : Nyquist plot for illustrating robust stability condition. ....	37
<b>Figure 3.10</b> : Stability of robustness for the time delayed integral plant with communication disturbance observer.....	39

<b>Figure 3.11:</b> Step responses of the time delayed integral plant for different cut-off frequencies $\omega_c$ of $Q(s)$ .	39
<b>Figure 3.12:</b> Time varying delay $T(t)$ .	40
<b>Figure 3.13:</b> Stability of robustness for the time varying delayed integral plant with communication disturbance observer.	41
<b>Figure 3.14:</b> Step responses of the time varying delayed integral plant for different cutoff frequencies $\omega_c$ of $Q(s)$ .	41
<b>Figure 3.15:</b> The basic elements of networked control system in vehicle.	43
<b>Figure 3.16:</b> The yaw stability control system block diagrams: (a)without CDOB, (b)with CDOB.	43
<b>Figure 3.17:</b> Time varying delay $T(t)$ in CAN communication.	44
<b>Figure 3.18:</b> Stability of robustness for the time varying delayed yaw stability control system with communication disturbance observer.	45
<b>Figure 3.19:</b> Simulation results for the yaw stability control system with and without CDOB.	46
<b>Figure 4.1 :</b> Vehicle steering model.	49
<b>Figure 4.2 :</b> Uncertainty box.	50
<b>Figure 4.3 :</b> The resistive forces acting on the longitudinal dynamics of the vehicle.	51
<b>Figure 4.4 :</b> The forces and the torques acting on the wheel.	52
<b>Figure 4.5 :</b> Experimental vehicle.	53
<b>Figure 4.6 :</b> Comparison of test data and nonlinear vehicle simulation results for lateral dynamics.	54
<b>Figure 4.7 :</b> Comparison of test data and nonlinear vehicle simulation results for longitudinal dynamics.	54
<b>Figure 4.8 :</b> D-stable region in the complex plane.	56
<b>Figure 4.9 :</b> Control system structure.	57
<b>Figure 4.10:</b> Detailed view of D-stability in parameter space for P1.	58
<b>Figure 4.11:</b> Overall D-stability solution region.	58
<b>Figure 4.12:</b> Simulation results 1.	59
<b>Figure 4.13:</b> Simulation results 2.	60
<b>Figure 4.14:</b> Steering control system structure based on digital map and GPS measurements.	61
<b>Figure 4.15:</b> A generated digital map using the constrained least square solution.	64
<b>Figure 4.16:</b> Lateral deviation and yaw angle error calculations.	65
<b>Figure 4.17:</b> Simulation results: desired map and stroboscopic vehicle trajectory.	66
<b>Figure 4.18:</b> Simulation results: the changes of important variables.	67
<b>Figure 5.1 :</b> The ILSC system structure.	71
<b>Figure 5.2 :</b> The single track vehicle (bicycle) model.	73
<b>Figure 5.3 :</b> The friction coefficient and velocity discretizations used for calculation of scheduled LQR gains.	75
<b>Figure 5.4 :</b> Vehicle geometry for the braking torque distribution algorithm.	76
<b>Figure 5.5 :</b> Different cases for braking torque distribution algorithm.	77
<b>Figure 5.6 :</b> Wheel slip control system structure.	78
<b>Figure 5.7 :</b> The PD control based algorithm (RB-LSC2) system structure.	82

<b>Figure 5.8</b> : The ILSC system simulation results for sine-with-dwell test ( $\mu = 0.5$ , 25% of Throttle).....	83
<b>Figure 5.9</b> : The ILSC system simulation results for fishhook test ( $\mu = 0.6$ , 25% of Throttle).....	84
<b>Figure 5.10</b> : The RB-LSC1 system simulation results for sine-with-dwell test ( $\mu = 0.5$ , 25% of Throttle).....	85
<b>Figure 5.11</b> : The RB-LSC1 system simulation results for fishhook test ( $\mu = 0.6$ , 25% of Throttle).....	85
<b>Figure 5.12</b> : The RB-LSC2 system simulation results for sine-with-dwell test ( $\mu = 0.5$ , 25% of Throttle).....	86
<b>Figure 5.13</b> : The RB-LSC2 system simulation results for fishhook test ( $\mu = 0.6$ , 25% of Throttle).....	87
<b>Figure 5.14</b> : Stroboscopic plots for sine-with-dwell maneuver. ....	88
<b>Figure 5.15</b> : Stroboscopic plots for fishhook maneuver.....	88
<b>Figure 5.16</b> : The Basic ESC and the ILSC system simulation results for FMVSS No. 126 test. ....	89



# ADVANCED CONTROL SYSTEMS FOR GROUND VEHICLES

## SUMMARY

The vehicle control systems or automotive control is a very important application area of the advanced control systems theory. Along with the advances in the electronics, the control systems have been used in ground vehicles increasingly. They have been played vital role in vehicles by improving safety, reducing pollutant emissions and providing fuel economy. This thesis focuses the important problems of the ground vehicle control systems within the scope of the robust control methodology, especially based on the parameter space and the disturbance observer approaches. Four different problems are investigated in the thesis: robust DC motor speed control for fully electric vehicles, time delay compensation for the vehicle yaw stability control systems, robust automatic steering control for highly automated driving and the lateral stability control for fully electric vehicles.

Firstly, the robust DC motor speed control problem for fully electric vehicles is investigated. The parameter space approach based robust PI controller design is performed considering the uncertain motor parameters. In the robust PI controller design step, the multi-objective design requirements are taken into account such as Hurwitz stability, D-stability, phase margin bounds and the frequency domain specifications. An add-on disturbance observer is employed to improve the tracking and the disturbance rejection properties of the proposed robust PI control system. The parameter space approach based robust PI controller and the add-on disturbance observer is tested by the help of simulations and experiments. The robust PI plus disturbance observer control system shows better performances for all the simulations and experiments.

Secondly, the time delay problems in automotive control applications are discussed. The communication disturbance observer approach for the time delay compensation is introduced. A novel robust stability condition is developed for the cases of the constant and the time varying delay. This robust condition is used in the design of the communication disturbance observer for the forth order time delayed plant with free integrator, which is a special case of unstable time delayed plants. The method is also applied to the vehicle yaw stability problem over CAN bus which suffers from the destabilizing effect of the time delay. It is seen that the time varying delay causes instability in the case of only PI control but in the case of the add-on communication disturbance observer, the vehicle becomes stable and also the yaw rate of the vehicle follows the desired yaw rate successfully.

Thirdly, the robust automatic steering control for highly automated driving is studied. The parameter space approach based robust PID steering control system is designed considering the uncertainties in the vehicle mass, the vehicle velocity and the tire-road friction coefficient. The designed robust controller is tested with the different paths and

the road conditions using the experimentally validated nonlinear vehicle model. Also, the design of digital map and GPS measurements based robust steering controller is performed. The high resolution digital map is generated using the constrained least square method. The lateral deviation and the yaw angle of the vehicle, which are used to determine the feedback signal of the controller, are calculated using this offline generated map and online vehicle's position information. The proposed method is tested successfully on an eight segments road with the validated vehicle model.

Lastly, the problem of lateral stability control for fully electric vehicles is discussed. Two different control systems are proposed: integrated lateral stability control (ILSC) and regenerative braking based lateral stability control (RB-LSC) systems. Also, a benchmark PID based controller (Basic ESC) is used for the comparison of the control systems. Two different tests (the sine-with-dwell and the fishhook) are performed to analyze the proposed controllers. According to the results, the minimum errors of yaw rate and side slip angle are obtained by the proposed ILSC system both for the sine-with-dwell and the fishhook tests. In addition, the standard ESC regulation test (FMVSS No. 126) is applied to the proposed control systems. The Basic ESC and ILSC systems are passed the FMVSS No. 126 test. The RB-LSC systems are found as cheaper alternative support systems in order to correct the yaw dynamics of vehicles not equipped with ESC in a limited manner.

## YOL TAŞITLARI İÇİN İLERİ KONTROL SİSTEMLERİ

### ÖZET

Taşıt kontrol sistemleri veya diğer bir deyişle otomotiv kontrolü, ileri kontrol sistemlerinin en önemli uygulama alanlarından biridir. Elektronik teknolojisindeki ilerlemelerle birlikte, taşıtlarda kontrol sistemi kullanımı giderek yaygınlaşmıştır. Taşıt kontrol sistemleri, yolcu güvenliğinin artırılmasında, kirletici bileşen salınımının azaltılmasında ve taşıtlarda yakıt ekonomisinin sağlanmasında oldukça önemli bir rol oynamaktadır. Günümüzde taşıtlara uygulanmış olan kontrol sistemleri; frenleme esnasında tekerleklerin kilitlenmesini önleyen ABS, çekiş kontrolü sağlayan TCS, taşıt yanal kararlılığının sağlanmasına yardımcı olan ESC, öndeki taşıt ile otomatik olarak hız kontrolünü sağlayan ACC, özellikle ağırlık merkezi yerden yüksek olan taşıtlarda kullanılan devrilme önleyici sistemler, şerit ihlali uyarıcı ve şerit takip sistemleri LDW/LKA ve çarpışma uyarıcı ve önleyici sistemler CW/CA olarak sayılabilir.

Taşıt kontrol sistemleri; güvenliği artırmaya, kirletici seviyelerini istenen seviyelere düşürmeye ve taşıtlarda yakıt ekonomisinin sağlanmasına yardımcı olmasının yanısıra akıllı taşıt ve ulaşım sistemlerinin de en temel bileşenlerinden birisidir. Örneğin ACC ve ESC sistemleri otonom taşıt davranışının ilk örneklerindedir. Taşıt kontrol sistemlerinde elde edilen gelişmeler direkt olarak otonom taşıt çalışmalarını etkilemektedir.

Bu tezde yol taşıtı kontrol sistemleri için önemli olan problemler, dayanıklı kontrol teorisi çerçevesinde ele alınarak çözüm getirilmeye çalışılmıştır. Özellikle parametre uzayı tabanlı dayanıklı kontrol ve bozucu gözleyici yaklaşımları taşıt kontrol problemlerinin çözümünde metot olarak kullanılmıştır. Tez kapsamında araştırılan problemler şunlardır: tam elektrikli taşıtlar için dayanıklı DC motor hız kontrolü, CAN hattı üzerinden taşıt savrulma dinamiği kontrolü için zaman gecikmesi telafisi, otonom taşıtlar için dayanıklı direksiyon kontrol sistemi tasarımı ve tam elektrikli taşıtlar için taşıt yanal dinamiğinin kontrolü.

İlk olarak, tam elektrikli araçlarda dayanıklı DC motor hız kontrolü problemi ele alınmıştır. Parametre uzayı yaklaşımı kullanılarak motor parametrelerindeki belirsizlikler dikkate alınarak dayanıklı PI kontrolcü tasarımı gerçekleştirilmiştir. DC motorda belirsizlik içeren parametreler, motor tork sabiti ve motorun toplam atalet momenti olarak seçilmiştir. Dayanıklı PI kontrolcü tasarımında, Hurwitz kararlılığı, D-kararlılığı, faz payı istekleri ve frekans domeni istekleri gibi çok amaçlı tasarım ihtiyaçları dikkate alınmıştır. Bu tasarım ihtiyaçları, parametre uzayında gösterilerek dayanıklı PI kontrolcünün katsayıları istenen tasarım kriterlerini sağlayacak şekilde seçilmiştir.

Dayanıklı PI kontrollü sistemin istenen girişi takip özelliğini artırmak ve bozuculara karşı hassasiyetini azaltmak için önerilen kontrol sistemine ek olarak bozucu gözleyici kullanılmıştır. Bozucu gözleyici tabanlı kontrol, kontrol sisteminin modelleme

hatalarına ve bozucu etkilere karşı hassasiyetini azaltan ve sistemin istenen nominal model davranışını göstermesini sağlayan bir yöntemdir. Bu yöntem, mekatronik sistemlerin kontrolü sahasında çeşitli uygulama alanlarında kullanılmaktadır. Bozucu gözleyici tabanlı taşıt yanal dinamiği kontrolü, dayanıklı atomik kuvvet mikroskobu kontrolü, imalat sistemleri kontrolü, elektrikli bisiklet kontrolü ve sabit disk servo sistem kontrolü bu uygulamalardan birkaçıdır.

Bu tezde bozucu gözleyici tasarımı DC motor hız kontrolünde sistem cevabını iyileştirmek ve bozucu etkisinin sistem cevabına olan negatif etkisinin azaltılmak için, dayanıklı kararlılık koşulu gözönüne alınarak gerçekleştirilmiştir. Dayanıklı bozucu gözleyici tasarımında, PI kontrolcü tasarımında dikkate alınmayan modellenmemiş dinamik ve zaman gecikmesi de hesaba katılmıştır. Parametre uzayı tabanlı dayanıklı PI kontrolcü ve ek bozucu gözleyici, simülasyonlar ve deneyler yardımıyla test edilmiştir. Üç farklı deney, DC motor seti kullanılarak gerçekleştirilmiştir. Bu testler; istenen girişi takip testi, basamak bozucu etkisi testi ve rampa bozucu etkisi testidir. Dayanıklı PI ve ek bozucu gözleyici kontrol sistemi, tüm simülasyon ve deneylerde daha iyi performans göstermiştir.

İkinci olarak, otomotiv kontrol uygulamalarındaki zaman gecikmesi problemi incelenmiştir. Zaman gecikmesi, sistem frekans cevabına negatif faz açısı ekleyerek sistemin kararlılık özelliklerini kötüleştirmekte ve kimi durumlarda da sistemde kararsızlığa yol açmaktadır. Tez kapsamında, zaman gecikmesi telafisi için zaman gecikmesi gözleyicisi önerilmiştir. Zaman gecikmesi gözleyicisi, gecikme telafisinde sıklıkla kullanılan Smith tahmincisine göre, zaman gecikmesi modeli gerektirmemesi ve zamanla değişen gecikmelerde de iş görmesi bakımından oldukça avantajlıdır. Zaman gecikmesi gözleyicisi yapı olarak bozucu gözleyiciye benzemekle birlikte, bu gözleyici de kullanılan bozucu tanımlaması ve zaman gecikmesi telafisi kısmı bozucu gözleyiciden farklıdır.

Tez kapsamında öncelikle zaman gecikmesi gözleyicisi ve network bozucu konsepti anlatılmıştır. Daha sonra zaman gecikmesi gözleyicisi, dördüncü dereceden serbest integratörlü bir sistemde zaman gecikmesini telafi etmek için kullanılmıştır. Zaman gecikmeli serbest integratörlü sistemler, kararsız zaman gecikmeli sistemlerin özel bir örneği olduğu için bu tip bir sistem seçilmiştir. Değişken zaman gecikmeleri ile simülasyonlar yapılarak, zaman gecikmesi gözleyecisinin çalışması incelenmiştir.

Tezde sabit ve zamanla değişen gecikme durumlarında dayanıklı zaman gecikmesi gözleyici tasarımı için, özgün bir dayanıklı kararlılık koşulu geliştirilmiştir. Bu dayanıklı kararlılık koşulu kullanılarak, örnek zaman gecikmeli serbest integratörlü sistem için zaman gecikmesi gözleyici tasarlanmıştır. Çeşitli simülasyonlarla, önerilen sistem test edilmiştir.

Uygulama alanı olarak, zaman gecikmesi pek çok otomotiv kontrol probleminde görülmekte ve bu sistemlerde kararsızlığa yol açabilmektedir. Bu tip sistemlere örnek olarak; rölanti devri kontrol sistemleri, motor hava yakıt karışımı oranı kontrol sistemleri, araç güç iletim sistemlerindeki sarsma önleyici kontrol sistemleri, kooperatif adaptif seyir kontrol sistemleri ve CAN üzerinden gerçekleştirilen tüm dağıtılmış kontrol sistemleri sayılabilir. Tez kapsamında zaman gecikmesi gözleyicisi, CAN hattı üzerinden taşıt savrulma dinamiği kontrolünde zaman gecikmesinin kararsızlığa yol açan etkisinin giderilmesinde kullanılmıştır. Zaman gecikmesi gözleyicisi tasarımında, zamana bağlı değişen gecikmeler için önerilen, dayanıklı kararlılık koşulundan yararlanılmıştır. Yapılan çalışmada, PI kontrollü taşıt savrulma

dinamiğinin, zamanla değişen gecikme altında kararsızlığa gittiği görülmüştür. Sisteme eklenen zaman gecikmesi gözleyicisi sayesinde taşıt kararlı hale getirilmiş ve taşıtın istenen savrulma açısı hızını başarıyla takip etmesi sağlanmıştır.

Üçüncü olarak, otonom taşıtlar için dayanıklı otomatik direksiyon kontrolü üzerinde durulmuştur. Taşıt kütlesi, taşıt hızı ve tekerlek-yol sürtünme katsayısındaki belirsizlikler dikkate alınarak parametre uzayı yaklaşımı ile dayanıklı PID direksiyon kontrolcüsü tasarımı yapılmıştır. Kontrolcü tasarımında tek izli taşıt modeline referans yolu takip etme dinamiği eklenerek oluşturulmuş taşıt yönlendirme modeli kullanılmıştır. Tasarlanan kontrolcüyü test edebilmek için, doğrulanmış nonlineer taşıt modeli kullanılmıştır. Model doğrulama çalışmasının sonuçları verilerek model ile gerçek taşıt sonuçlarının uyumu gösterilmiştir. Daha sonra da tasarlanan dayanıklı PID direksiyon kontrolcüsünün farklı yörüngelerde ve farklı yol koşullarındaki performansı yapılan simülasyon çalışmalarıyla irdelenmiştir.

Üstte belirtilen yaklaşımdan farklı olarak dijital yol haritası ve GPS ölçümlerine dayalı dayanıklı direksiyon kontrol sistemi tasarımı da tez kapsamında gerçekleştirilmiştir. Yüksek çözünürlüklü dijital harita kısıtlanmış en küçük kareler yöntemi kullanılarak üretilmiştir. Taşıt ağırlık merkezinin istenen rotadan sapma miktarı ve taşıt sapma açısı, üretilen harita ve gerçek zamanlı taşıt pozisyon bilgisi kullanılarak hesaplanmıştır. Dayanıklı PID direksiyon kontrol sisteminde, geri besleme olarak taşıttan belli bir ön mesafedeki rotadan sapma miktarı kullanılmaktadır. Bu geri besleme sinyali, harita ve gerçek zamanlı taşıt pozisyon bilgisinden yararlanılarak bulunan taşıtın rotadan sapma miktarı ve taşıt sapma açısı kullanılarak hesaplanmaktadır. Önerilen metot, sekiz bölmeli bir yolda doğrulanmış nonlineer taşıt modeli kullanılarak başarıyla test edilmiştir.

Son olarak, tam elektrikli taşıtlarda yanal kararlılık problemi konusu ele alınmıştır. Problemin çözümü için iki farklı kontrol sistemi önerilmiştir. Bunlar, bütünleşik yanal kararlılık kontrol (ILSC) sistemi ve rejeneratif frenleme tabanlı yanal kararlılık kontrol (RB-LSC) sistemidir.

ILSC sistemi, düzeltici savrulma momenti hesabı, fren torku dağılım algoritması, tekerlek kayma kontrolcüsü ve elektrik motoru torku azaltma algoritması gibi alt sistemlerden oluşmuştur. Kontrolcü tarafından hesaplanan düzeltici savrulma momenti, tekil frenleme yoluyla taşıta etkimektedir. Fren torku dağılım algoritmasıyla hangi tekerleğin frenleneceği tespit edilmektedir. Frenleme gerçekleştirilirken tekerleklerin kilitlenmesini önlemek için, tekerlek kayma kontrolcüsü kullanılmaktadır. Tekil frenlemenin yeterli kalmadığı durumlarda ise elektrik motoru torku azaltılarak taşıtın yanal kararlılığı sağlanmaya çalışılmaktadır.

RB-LSC sistemi, ILSC'ye göre daha basit ve ucuz, daha az sensör, tahminci ve eyleyici kullanımı gerektiren bir yöntemdir. Bu kontrol sisteminde, elektrik motoru torku kontrol edilerek taşıt yanal kararlılığı sağlanmaya çalışılmaktadır. RB-LSC sistemi için iki farklı yaklaşım önerilmiştir. RB-LSC1'de elektrik motoru torku, taşıt yana kayma açısı ve taşıt savrulma açısı hata değerlerine göre bang-bang kontrolcü yardımıyla kontrol edilerek rejeneratif frenleme gerçekleştirilmektedir. RB-LSC2'de ise elektrik motoru torku sadece taşıt savrulma açısı hata değerine göre PD kontrolcü yardımıyla ayarlanarak rejeneratif frenleme yapılmaktadır. Belirtilen bu ikinci yöntem, taşıt yana kayma açısı tahminine ihtiyaç duymamasından dolayı daha avantajlıdır.

Önerilen kontrol sistemlerin karşılaştırılmasında kullanılmak üzere Temel ESC olarak adlandırılan PID tabanlı bir kontrol sistemi de tez kapsamında kullanılmıştır. Tüm kontrol sistemleri, iki farklı test kullanılarak değerlendirilmiştir. Bu testler beklemeli sinüs testi ve kanca testidir. Yöntemleri sayısal olarak karşılaştırmak için, taşıt yanal dinamiğinin en önemli göstergeleri olan taşıt savrulma açısız hızının ve taşıt yana kayma açısının hata değerleri kullanılmıştır. Elde edilen sonuçlara göre, hem beklemeli sinüs testine, hem de kanca testine göre en küçük taşıt savrulma açısız hızı ve taşıt yana kayma açısı hata değerleri önerilen ILSC sistemi ile elde edilmiştir.

Ayrıca bahsedilen tüm yanal kararlılık kontrol sistemleri, standart ESC regülasyon testi olan FMVSS No. 126 testine sokulmuştur. Temel ESC ve ILSC sistemleri bu testi geçmiştir. RB-LSC sistemleri bu testi geçememesine rağmen, ESC sistemine sahip olmayan taşıtlarda kısıtlı iyileştirme sağlayabilecek ucuz alternatif sürücü destek sistemleri olarak önerilmiştir.

## 1. INTRODUCTION

Today's ground vehicles are the most important example of the electronic control system applications. During the last two decades, the advances in electronics result in the using of the electronic control systems in ground vehicles commonly. Automotive control and mechatronics become essential in ground vehicles for improving safety, reducing pollutant emission levels and providing fuel economy [1].

In Europe, 160 billion Euros is lost in accidents, per year. This is equivalent to 2% of the GNP of Europe. There are 41,000 deaths and a very large number of injuries as a result of these road vehicle accidents, per year [2]. The vehicle control systems are very important to prevent accidents and/or reduce the deaths and the fatal injuries arisen from the accidents.

Some control systems are applied to passenger's vehicles such as anti-lock braking system (ABS), traction control systems (TCS), electronic stability control system (ESC), adaptive cruise control (ACC), rollover avoidance system, lane departure warning and lane keeping assistance systems (LDW/LKA) and collision warning and collision avoidance systems (CW/CA). The design, improvement and adaptation of new control systems continue at Universities' research labs and automotive companies' R&D centers. Moreover, the usage of the vehicle control systems is increasing rapidly. For example, in 1995, the proportion of new cars equipped with ESC was only 5% (in Germany); in 2004, the proportion was 36% in Europe, and much higher in some European countries, e.g. 67% in Germany [3]. In Sweden the ESC equipped vehicle usage has increased 15% to 69% from 2003 March to 2004 December [4].

The vehicle control systems are the essential parts of the intelligent vehicles and intelligent transportation systems in conjunction with sensing and perception. Autonomy in vehicles requires control of motion considering some objectives and constraints. Today's control systems in vehicles such as ACC and LKA are also initial examples of autonomous behavior. The developments of the vehicle control systems directly affect the advances in intelligent autonomous vehicles [5].

Besides the importance of the control systems in intelligent vehicles and intelligent transportation systems, another important issue is the control systems of electric vehicles. There is growing interest in fully electric vehicles in the automotive industry as it becomes increasingly more difficult to meet new and upcoming emission regulations based on internal combustion engines. As a result, some automotive producers are already introducing a variety of fully electric vehicles into the commercial market while other automotive companies are building and evaluating research prototypes. Fully electric vehicles do not have an internal combustion engine. They are usually lighter vehicles with different dynamic characteristics than that of their predecessors that are powered by internal combustion engines (ICEs). As such, their electronic control systems have to be re-designed [6]. For example, the regenerative braking capability of fully electric vehicles has to be taken into account in designing braking controllers like ABS [7, 8].

In this thesis, the important problems of the ground vehicle control systems are discussed and some solutions are developed within the scope of robust control methodology. In general, the parameter space approach based robust control and disturbance observer based control methodologies are applied to the problems. Robust DC motor speed control in fully electric vehicles, time delay compensation in automotive control systems, robust automatic steering control in autonomous vehicles and lateral stability control in fully electric vehicles are studied as problems.

In Chapter 2, robust DC motor speed control for automotive applications is investigated. Two parameters of the DC motor are determined as uncertain parameters. The parameter space approach based robust controller design methodology similar to given in [9, 10] is used here. The parameter space approach can be employed to determine a set of coefficients for a given controller structure which simultaneously stabilize a finite number of plants. In the design stage, multi-objective design requirements such as Hurwitz stability, D-stability, gain and phase margin bounds and frequency domain (mixed sensitivity) specifications can be considered. In Section 2.3, the introduced parameter space approach based design methodology is applied to the robust DC motor speed control.

In order to improve the system response of the robustly controlled system, add-on disturbance observer is proposed in Section 2.4. The disturbance observer design

methodology considering robust stability is given. The tracking performance and disturbance rejection capability of the overall system with add-on disturbance observer is investigated in Section 2.5. To show the effectiveness of the proposed control system, experiments are conducted and results are reported in Section 2.6.

The main focus of Chapter 3 is to develop disturbance observer based time delay compensation technique that can be used in automotive control problems which suffer from the negative effects of the time delay. Communication disturbance observer approach, which is firstly introduced in [11] to compensate the time delay inherent in bilateral teleoperation systems, is used in this thesis to compensate the destabilizing effect of the time delay on the system. The structure of the communication disturbance observer is similar to the disturbance observer except the disturbance definition and time delay compensation part.

After introducing the concept of the communication disturbance observer in Section 3.2, it is applied a fourth order time delayed plant with a free integrator in Section 3.3. Since integral plants with time delay are a special case of the unstable time delayed systems, this type plant is selected an application example. A novel robust stability condition is proposed for the cases of constant and time varying delays in Sections 3.4 and 3.5. This robust stability condition is used in the design stage of the communication disturbance observer.

Time delay occurs and causes stability problems in many automotive control systems such as idle speed control, air-to-fuel ratio control, anti-jerk control, cooperative adaptive cruise control and other Controller Area Network (CAN) based distrusted control systems in vehicle. In Section 3.6, vehicle yaw stability control considering CAN bus communication is discussed. The proposed communication disturbance observer approach is employed to compensate the effect of the time delay in yaw stability control over CAN bus.

In recent years, many research efforts have concentrated on intelligent vehicle systems and highly automated driving technologies. The main focus of Chapter 4 is robust automatic steering control in highly automated vehicles. In Section 4.2, vehicle steering model and experimentally validated nonlinear vehicle model is introduced. The parameter space approach based robust PID steering controller design

is performed in Section 4.3 considering the uncertainties in the vehicle mass, the vehicle velocity and the tire-road friction coefficient. In Section 4.4, the designed robust controller is tested with different desired paths and road conditions.

In Section 4.5, digital map and GPS measurements based robust PID steering control system is presented. Different from the approach is given in Section 4.3.2., the lateral deviation and the yaw angle error of the vehicle are calculated using the offline generated digital map and online the vehicle's position information here. In Section 4.5.1, high precision digital map generation is introduced based on constrained least square method similar to given in [12]. The details of the lateral deviation and the yaw angle error calculations are given in Section 4.5.2. The proposed method is tested with a specific eight segments map in the final section of Chapter 4.

Hybrid electric and fully electric vehicles are becoming more popular as fossil fuel resources are declining and environmental issues are becoming more demanding. As a result, the studies on electric vehicles have increasingly continued both at academy and industry. In recent years, lateral stability control systems have become mandatory in most countries for new vehicles. They have to be adapted to fully electric vehicles. For this reason, the problem of vehicle lateral stability control for fully electric vehicles is investigated in Chapter 5.

Two different lateral stability control system is proposed for a front wheel driven single motor electric vehicle in this thesis. One of them is a novel integrated lateral stability control (ILSC) system and the second one is a regenerative braking based lateral stability control system (RB-LSC).

In Section 5.2, the proposed ILSC system is introduced. The proposed ILSC system consists of some parts such as corrective yaw moment calculation, braking torque distribution algorithm, wheel slip control and electric motor torque reduction algorithm. The corrective yaw moment calculation is performed based on a scheduled LQR controller. The corrective yaw moment actuation is applied through individual wheel braking. The braking torque distribution algorithm and wheel slip controls are also used at the lower control level. The wheel slip controller is a bang-bang controller where the desired slip ratios are determined based on a scheduled LQR controller. In addition to the individual braking intervention, electric motor torque reduction is

applied when the individual braking is not enough to provide lateral stability of the vehicle.

In Section 5.3, the proposed second method - RB-LSC - is introduced. RB-LSC method is a simpler method than the ILSC system. In this method, electric motor torque is regulated to stabilize vehicle behavior according to the vehicle side slip error and/or the vehicle yaw rate error. Two different RB-LSC structures are proposed. Also, a benchmark PID based controller called Basic ESC is employed for the performance comparison of the proposed controllers. In Section 5.4, the designed controllers are tested with several simulation studies. They are compared with each other according to the sensor, estimator, and actuator usage. Also, a comparison is performed in accordance with the calculated error values in tests. In Section 5.4.3, the standard ESC regulation test - NHTSA FMVSS No. 126 - is carried out for all control systems and results are reported.

Finally, Chapter 6 provides the conclusions and the recommendations. This is followed by the potential future extensions on the work presented here.



## **2. PARAMETER SPACE APPROACH BASED ROBUST PI DC MOTOR SPEED CONTROL AND PERFORMANCE IMPROVEMENTS USING DISTURBANCE OBSERVER**

### **2.1 Introduction**

Direct current (DC) motors are essential parts of mechatronic and control systems. The use of DC motors in scientific research and industrial applications is very prevalent for their accurate and simple control characteristics. DC motors have been widely used in robotic applications, positioning systems, electric vehicles, flatbed scanners [13–15] and all sorts of rotational actuation processes.

DC motors are also employed in automotive control applications. One of the important application areas is the speed control of the DC motor in electric vehicles. Due to the simplicity of the DC motor controlling and the fact that the power supply from the battery is DC power, DC motors are typically selected for the traction of electric vehicles [16].

There have been many contributions in the literature for dc motor control ranging from conventional PID control to advanced control methodologies such as sliding mode control, robust  $H_\infty$  control, LMI based robust control, adaptive control, intelligent control such as fuzzy logic, neural network and fractional order controllers.

In [17], sliding mode controller, integral sliding mode controller and dynamic sliding mode controller designs are represented for the DC motor speed control and the controllers are compared each other using simulation results with respect to their robustness against matched uncertainties and chattering reduction. Chattering is reduced with integral and especially dynamic sliding mode techniques. In [18], sliding mode control approach is applied to separately excited DC motor and the results are compared with the conventional PI controller using simulations. In [16], a sliding mode controller requiring only output feedback is proposed and verification with three different experiments on a DC motor speed control system is performed. A pre- and post-filtering approach to output feedback variable structure speed control of a

permanent magnet dc motor is proposed and tested by simulations and experiments in [19]. In [20], a DC motor speed controller is proposed gathering the features of sliding mode control, fuzzy inference system, neural network and genetic algorithms in order to avoid the chattering disadvantage of sliding mode control. The designed controllers are implemented on a FPGA. The fluctuations in the conventional sliding mode controller results are reduced with sliding mode controller with adaptive neural fuzzy interference system and after the optimizing the fuzzy inference system with genetic algorithms the best final results are obtained. A robust  $H_\infty$  optimal speed control scheme for a DC motor with parameter variations using a linear matrix inequality approach is introduced and tested by simulations in [21]. In [22], a mixed  $H_2/H_\infty$  robust controller design for dc motor speed control is presented and tested by simulations. Improved particle swarm optimization is used to solve the optimization problem of  $H_2/H_\infty$  controller and find the optimal parameters of the controller.

A robust adaptive discrete variable structure control scheme for DC motor speed control is described and successfully implemented in [23]. A self tuning minimum variance adaptive control method is developed and successfully implemented for speed and position tracking of a DC motor in [24]. In [25], an online self tuning artificial neural network based speed control scheme is proposed and experimentally implemented for a DC motor. The proposed scheme is compared with PI controller based system. The results show that the performance of artificial neural network based system is superior. An adaptive control algorithm using bacterial foraging algorithm for DC motor speed control is represented in [26]. In this research, bacterial foraging algorithm is used for identification and control of DC motor. A comparison of bacterial foraging algorithm based control and genetic algorithm based control is carried out. An adaptive PID-type neural network control method is applied for the speed control of a DC motor system dead-zone characteristics in [27]. A fractional order PI controller for controlling the speed of a DC motor was designed and implemented on a FPGA target in [28].

In this chapter, parameter space approach based robust PI controller design was carried out to control of DC motor speed considering multi-objective design requirements such as D-stability, phase margin bounds and mixed sensitivity (robust performance) requirements. The parameter space approach can be used to determine a set of

coefficients for a given controller structure which simultaneously stabilize a finite number of plants. The set of parameters for which the characteristic polynomial is Hurwitz-stable is determined. Along with Hurwitz stability, the method has been extended to D-regions for treating relative stability and bandwidth constraints. The parameter space approach cannot handle only parametric (structured) uncertainties. By mapping frequency domain specifications into parameter space, the parameter space method provides the using of experience in the field of frequency domain robust control methods which generally tackle unstructured uncertainties such as  $H_\infty$  robust control. The further information about parameter space approach can be found at [9, 10]. The mapping of design requirements into the parameter space to find the robust fixed disturbance observer (DOB) parameters was applied to vehicle yaw stability control successfully in earlier works [29–31]. In this chapter, parameter space approach based design methodology used for designing robust PI controller. Also, an add-on disturbance observer employed to improve the tracking and disturbance rejection properties of the robust PI based control system. Robust PI and add-on disturbance designs were tested by simulations and experiments.

The organization of the rest of this chapter is as follows. The DC motor model and the uncertain parameters of the DC motor are introduced in Section 2.2. Mapping the robust controller design requirements into the parameter space such as Hurwitz stability, D-stability, phase margin and mixed sensitivity (robust performance) requirements are explained and also design method is applied to DC motor speed control in Section 2.3. The add-on disturbance observer structure and design methodology are given Section 2.4. The simulation results are shown in Section 2.5. Experimental set-up is described and experimental results are given in Section 2.6. The chapter ends with conclusions in Section 2.7.

## 2.2 DC Motor Modeling and Uncertainties

This section describes the DC motor modeling. Figure 2.1 shows the DC motor scheme with its electrical and mechanical parts.

Using Kirchhoff's law, the following equation is obtained.

$$V_m = L_m \frac{dI_m}{dt} + R_m I_m + k_i \omega_m \quad (2.1)$$

where  $V_m$  is the voltage from the amplifier which drives the motor,  $R_m$  is the motor armature resistance,  $I_m$  is the motor armature current,  $L_m$  is the motor armature inductance,  $k_i$  is the back-EMF constant and  $\omega_m$  is the motor angular speed.

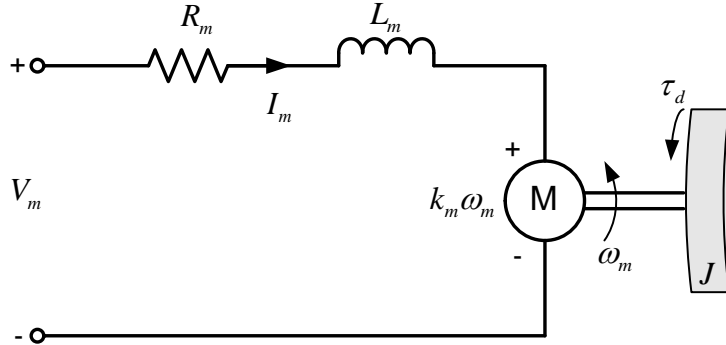


**Figure 2.1 :** The DC motor scheme.

The dynamics of the motor is given by Newton's second equation with the following equation:

$$J \dot{\omega}_m = k_m I_m + \tau_d \quad (2.2)$$

where  $J$  is the total moment of inertia (motor rotor and the load),  $\tau_d$  is the disturbance torque and  $k_m$  is the motor torque constant. In SI units, the motor torque constant is equal to back-EMF constant, that is  $k_i = k_m$ . After this,  $k_m$  is used for both constants.

Using (2.1) and (2.2) and assuming  $L_m \ll R_m$  and neglecting the viscous friction in the system, the transfer function  $G(s)$  from voltage applied to the motor to motor angular speed can be written as follows:

$$G(s) = \frac{k_m}{R_m \left( Js + \frac{k_m^2}{R_m} \right)} \quad (2.3)$$

The open loop block diagram of the motor with torque disturbance is depicted in Figure 2.2.

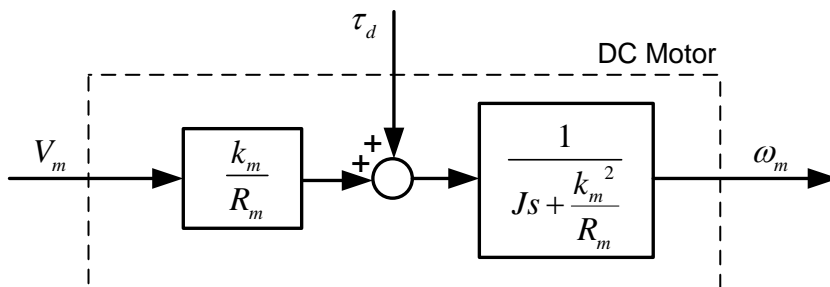


**Figure 2.2 :** The open loop block diagram of the DC motor with torque disturbance.

In the simulations and experiments Quanser DC motor set which includes a Maxon high quality DC motor is used. The nominal parameters of the DC motor used is given at Table 2.1.

**Table 2.1 :** The nominal parameters of the DC motor.

Parameter	Value	Unit
$k_m$	0.0502	$Nm/A$
$J$	$22.1 \times 10^{-6}$	$kgm^2$
$R_m$	10.6	$\Omega$

Two parameters  $k_m$  and  $J$  are taken as uncertain parameters considering  $\pm 20\%$  uncertainty on nominal values. values are between 0.0402 and 0.0602  $Nm/A$  and values are between  $17.68 \times 10^{-6}$  and  $26.52 \times 10^{-6}$   $kgm^2$ . An uncertainty box is depicted in Figure 2.3 for showing these uncertainties.

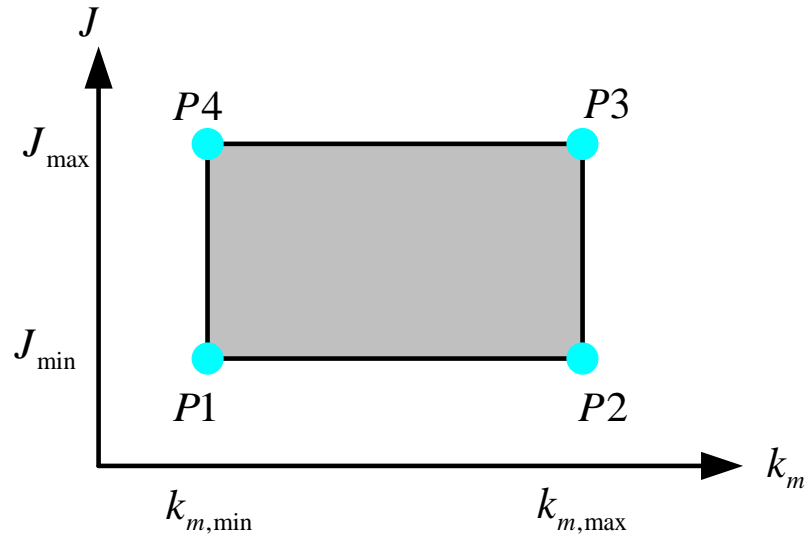


**Figure 2.3 :** Uncertainty box for the DC motor parameters.

### 2.3 Design Methodology by Mapping Multi-Objective Requirements into Parameter Space

In this section, a robust PI controller design methodology based on parameter space approach is introduced. The mapping of multi-objective design requirements into the parameter space is explained including Hurwitz stability, D-stability, phase margin bounds and frequency domain (mixed sensitivity) bounds mapping. The PI controlled closed loop system can be seen from Figure 2.4.

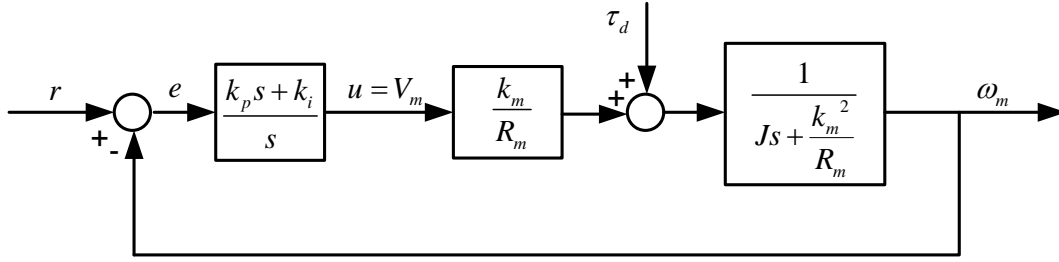


**Figure 2.4 :** The PI controlled closed system block diagram.

### 2.3.1 Hurwitz stability

Consider the plant is given by

$$G(s) = \frac{N(s)}{D(s)} \quad (2.4)$$

where  $N$  represents the numerator of the plant and  $D$  represents the denominator of the plant. The real and imaginary parts of the numerator and denominator can be defined as  $N(j\omega) = N_R(\omega) + jN_I(\omega)$  and  $D(j\omega) = D_R(\omega) + jD_I(\omega)$ .

The PI controlled closed loop system characteristic equation can be written as

$$p_c(s) = sD(s) + (k_p s + k_i)N(s) = a_{n+1}s^{n+1} + a_n s^n + \dots + a_1 s + a_0 = 0 \quad (2.5)$$

where  $n$  is the degree of the plant  $G(s)$ .

The Hurwitz stability boundary crossed by a pair of complex conjugate roots is characterized by the following equations:

$$Re[p_c(j\omega)] = 0 \text{ and } Im[p_c(j\omega)] = 0, \forall \omega \in (0, \infty] \quad (2.6)$$

This is called as complex root boundary (CRB).

There may be a real root boundary such that a single real root crosses the boundary at frequency  $\omega = 0$  is characterized by

$$p_c(0) = 0 \text{ or } a_0 = 0 \quad (2.7)$$

This is called as real root boundary (RRB).

There may exist an infinite root boundary (IRB) which is characterized by a degree drop in characteristic polynomial at  $\omega = \infty$ . This degree drop in characteristic polynomial is characterized as

$$a_{n+1} = 0 \quad (2.8)$$

CRB, RRB and IRB solutions by parameterizing  $\omega$  can be plotted into the  $k_p - k_i$  parameter plane to show the Hurwitz stability regions of the given closed loop system. The  $k_p - k_i$  values which provide Hurwitz stability can be chosen visually from the stable region of the parameter plane.

### 2.3.2 D-stability

The aforementioned parameter space computation method to determine Hurwitz stability regions can be extended to specify relative stability regions such as D-stability. A closed loop system is D-stable when the roots of the closed loop characteristic equation lie in the D-stable region in the complex plane as depicted in Figure 2.5.

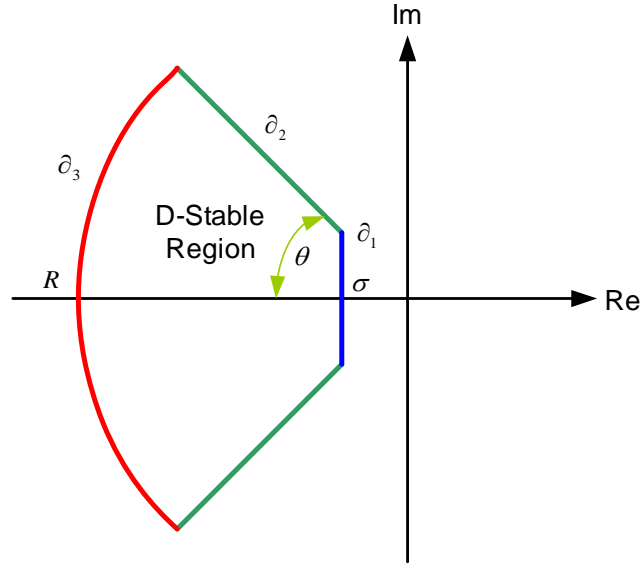


**Figure 2.5 :** D-stable region in the complex plane.

The boundary  $\partial_1$  in Figure 2.5 can be mapped into the parameter space by using  $s - \sigma$  instead of  $s$  in (2.5) in order to shift the stability boundary to  $\partial_1$  in the complex plane. Solving for  $k_p$  and  $k_i$  in (2.6) for CRB and (2.7) for RRB, and then plotting results in the  $k_p - k_i$  plane will result in the  $\partial_1$  boundary in the parameter space. For  $\partial_1$  boundary, there is no IRB because  $s$  is never equal to infinity in the D-shaped region. For mapping  $\partial_2$  boundary, use  $re^{j\theta}$  for  $s$  in (2.5) and parameterize  $r$  in  $re^{j\theta}$  to obtain the CRB of  $\partial_2$ . No RRB and IRB solution exists because  $r$  is never equal to zero or infinity. Lastly,  $\partial_3$  boundary maps into the parameter space by substituting  $s$  with  $Re^{j\theta}$  where  $R$  is constant and parameterizing over  $\theta$  in (2.5). This results in CRB for changing  $\theta$  and RRB for  $\theta = 0$ .

### 2.3.3 Phase margin

The constant phase margin can be also plotted in the parameter space. The constant phase margin boundary satisfies the following equation:

$$L(j\omega) = e^{j(m_\phi - \pi)} \quad (2.9)$$

where  $L$  is the loop gain and  $m_\phi$  is the phase margin bound.

The real and imaginary parts of  $L(j\omega)$  can be written as

$$Re[L(j\omega)] = Re[C(j\omega)G(j\omega)] = Re\left[\frac{k_p j\omega + k_i \frac{N_R + jN_I}{D_R + jD_I}}{j\omega}\right] = -\cos(m_\phi) \quad (2.10)$$

and

$$Im[L(j\omega)] = Im[C(j\omega)G(j\omega)] = Im\left[\frac{k_p j\omega + k_i \frac{N_R + jN_I}{D_R + jD_I}}{j\omega}\right] = -\sin(m_\phi) \quad (2.11)$$

From (2.10) and (2.11), solving for  $k_p$  and  $k_i$  values result in phase margin bound into the parameter space. Constant gain margin bounds can also be obtained in following similar procedure.

### 2.3.4 Mapping mixed sensitivity (frequency domain) bounds

The aim of this section is to map frequency domain criteria of robust control into the parameter space. Similar to the approach in [10, 30, 31], a parameter space design based on satisfying the robust performance requirement is used here as follows:

$$\| |W_S S| + |W_T T| \|_\infty < 1 \quad \text{or} \quad |W_S S| + |W_T T| < 1, \quad \forall \omega \quad (2.12)$$

where  $S = 1/(1+L)$  and  $T = L/(1+L)$  are the sensitivity and complementary sensitivity functions and  $W_S$  and  $W_T$  are corresponding weights.

Mixed sensitivity problem (2.12) can also be expressed in the limit as the equality

$$|W_S| + |W_T L| = |1 + L|, \quad \forall \omega \quad (2.13)$$

which is called the point condition at each frequency. The point condition is depicted in Figure 2.6.

A circle with origin at  $-1$  and a radius equal to  $|W_S(\omega)|$  at a specific frequency  $\omega$  is drawn first. Loop gain  $L(j\omega)$  at the same frequency is shown as vector  $L$  with magnitude  $|L|$  and angle  $\theta_L$  in Figure 2.6 and is given by

$$L(j\omega) = |L| e^{j\theta_L} \quad (2.14)$$

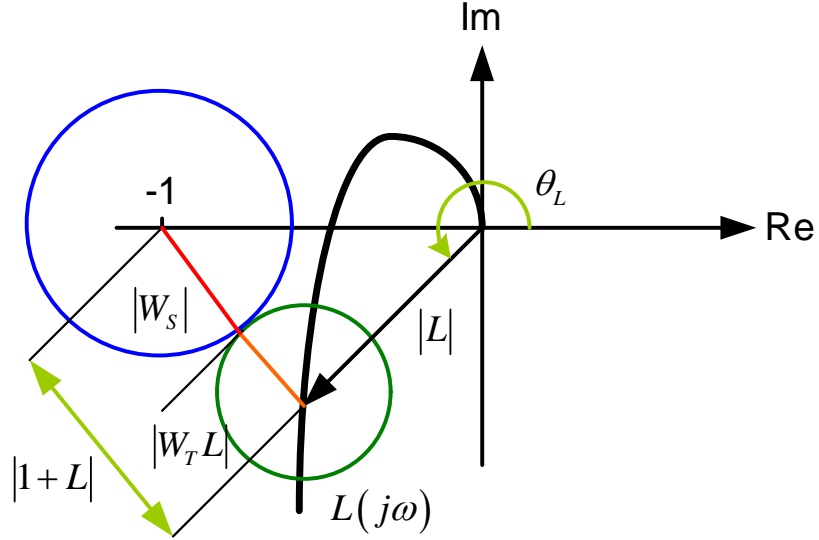


**Figure 2.6 :** The point condition for mixed sensitivity.

A second circle with origin at  $L(j\omega)$  and with a radius equal to  $|W_T(\omega)L(j\omega)|$  for specific frequency  $\omega$  is drawn next.

The vector  $1 + L$  originating at  $-1$  and ending at  $L$  in Figure 2.6 should be greater than  $|W_S| + |W_T L|$  to satisfy the inequality version of the point condition (2.13). This point condition needs to be solved at each frequency to find the controller parameter pairs that satisfy it. Solving and graphically intersecting the solution regions for a sufficient large number of frequencies result in the controller parameter space where robust performance is satisfied.

A graphical solution for  $|L|$  using the cosine rule for Figure 2.6 results in

$$|L| = \frac{-\cos \theta_L + |W_S| |W_T| \pm \sqrt{\Delta}}{1 - |W_T|^2} \quad (2.15)$$

where

$$\Delta = 1 + \cos^2 \theta_L - 2 |W_S| |W_T| \cos \theta_L + |W_S|^2 + |W_T|^2. \quad (2.16)$$

The first part of the solution procedure for loop gain  $L$  is the formation of a grid of  $\theta_L$  in  $[0, 2\pi]$  and then solving (2.15) for  $|L|$  and computing  $L = |L|e^{j\theta_L}$ . Then,  $L$  is expressed in terms of a fictitious controller  $K$  as follows:

$$L = KG = (K_R + jK_I)G \quad (2.17)$$

Solving (2.17) for the real and imaginary parts  $K_R$  and  $K_I$  of the fictitious controller  $K$  and then solving

$$K_R + jK_I = \frac{L}{G} = \frac{k_p j\omega + k_i}{j\omega} \quad (2.18)$$

for PI controller parameters  $k_p$  and  $k_i$  result in

$$k_p = K_R \quad (2.19)$$

$$k_i = -K_I \omega \quad (2.20)$$

which is the final step of the solution.

The aforementioned point condition solution procedure is summarized below.

1. Choose a specific  $\omega$  value.  $|W_S(\omega)|$ ,  $|W_T(\omega)|$  and  $G(j\omega)$  at frequency  $\omega$  are all known at this point.
2. Let  $\theta_L \in [0, 2\pi]$ . Evaluate  $\Delta$  using (2.16), and select the active range of  $\theta_L$ , where  $\Delta \geq 0$  is satisfied. For all values of  $\theta_L$  in the active range.
  - (a) Evaluate  $|L|$  using (2.15). Keep only the positive solutions (since  $|L|$  cannot be negative.)
  - (b) Evaluate  $L = |L| e^{j\theta_L}$ .
  - (c) Solve for the corresponding fictitious controller real and imaginary parts  $K_R$  and  $K_I$  in (2.17).
  - (d) Substitute for  $K_R$  and  $K_I$  into the right-hand sides of (2.19) and (2.20), and solve for  $k_p$  and  $k_i$ .
3. Plot the closed curve of  $k_p$  versus  $k_i$  values (for all active  $\theta_L$  values in 2). Either inside or the outside of this curve is a solution of (2.13) at chosen frequency  $\omega$ . The obtained region is the point condition solution in the chosen controller parameter plane at the frequency chosen in step 1.
4. Go back to 1, and repeat the procedure at a different frequency.

Plot the intersection of all point condition solutions for all frequencies considered. This is the overall solution region for robust performance.

### 2.3.5 Application to robust PI DC motor speed control

The aforementioned multi-objective robust controller design methodology was applied to PI DC motor speed control here. D-stability, phase margin and mixed sensitivity boundaries mapping procedure were realized for four operating points (vertices of the uncertainty box) shown in Figure 2.3. Then, the common  $k_p - k_i$  value that satisfies the design requirements for all points was selected from the  $k_p - k_i$  parameter plane.

D-stability requirements were determined as follows: no roots can be closer than  $-1$  to the Im axis ( $\sigma = 1$ ) and no roots can be further than  $-15$  ( $R = 15$ ), a maximum damping can be 70 degrees ( $\theta = 70^\circ$ ) which corresponding to a damping ratio of 0.342.

Phase margin can be at least 50 degrees ( $PM \geq 50^\circ$ ).

Figure 2.7 shows the solution regions for D-stability and phase margin requirements in parameter space.  $\partial_1$  CRB and RRB,  $\partial_2$  CRB and  $\partial_3$  CRB of D-stability and the increasing phase margin bounds depicted. The intersection of bounds determined the D-stable region with satisfying required PM bound.

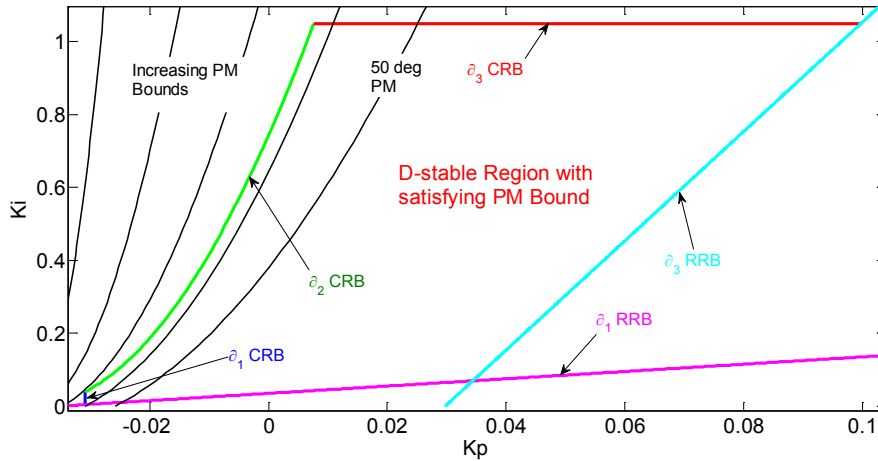


**Figure 2.7 :** Detailed view of D-stability and phase margin boundaries in parameter space for P1.

In order to map robust performance criteria into the parameter space, firstly the sensitivity and the complementary sensitivity weights were determined. The inverse of the sensitivity function weight is selected as

$$W_S^{-1} = h_s \frac{s + \omega_s l_s}{s + \omega_s h_s} \quad (2.21)$$

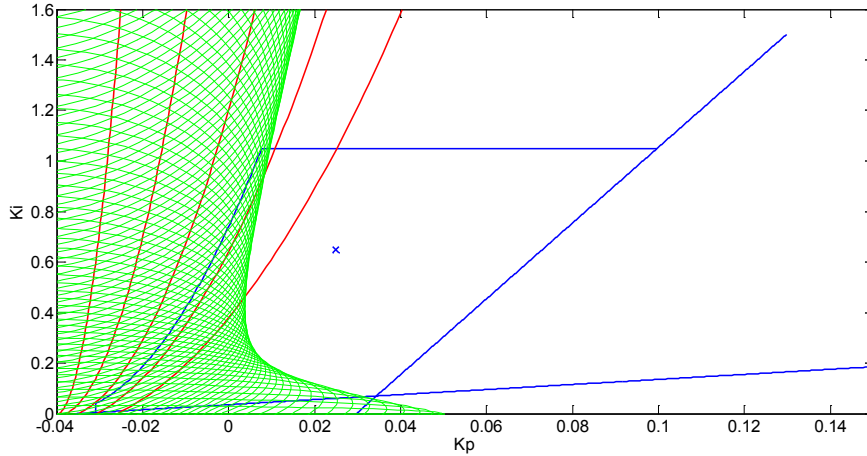
with  $l_s = 0.5$  (i.e., less than 50% steady state error) being the low frequency bound,  $h_s = 4$  being the high frequency bound, and  $\omega_s = 5 \text{ rad/sec}$  being the approximate bandwidth.

The complementary sensitivity function weight is chosen as

$$W_T = h_T \frac{s + \omega_T l_T}{s + \omega_T h_T} \quad (2.22)$$

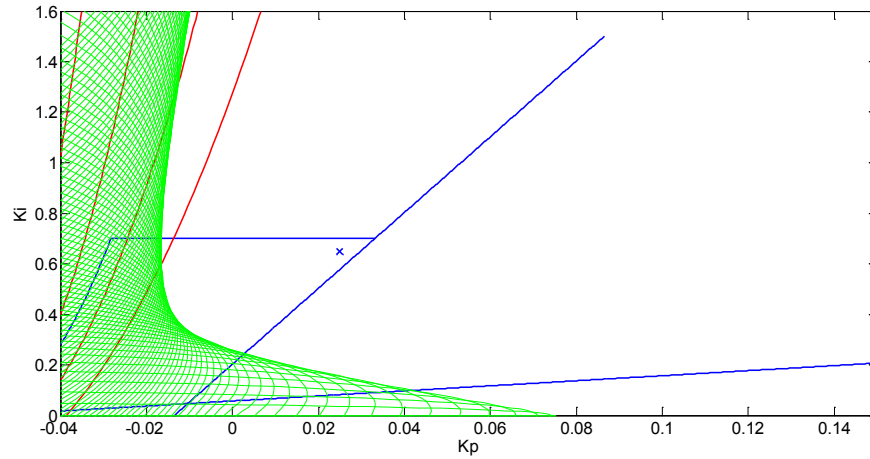
where the low frequency gain is  $l_T = 0.2$ , the high frequency gain is  $h_T = 1.8$  (corresponds to uncertainty of up to 180% at high frequencies), and the frequency of transition to significant model uncertainty is  $\omega_T = 120 \text{ rad/sec}$ .

The mixed sensitivity requirement for the selected weights was mapped into the parameter space. The results with including D-stability and phase margin boundaries can be seen from Figures 2.8, 2.9, 2.10 and 2.11 for the points P1, P2, P3 and P4 shown in Figure 2.3. Blue lines restricted the parameter space for D-stability, red lines restricted for PM bounds and green lines restricted the parameter space for mixed sensitivity requirements.

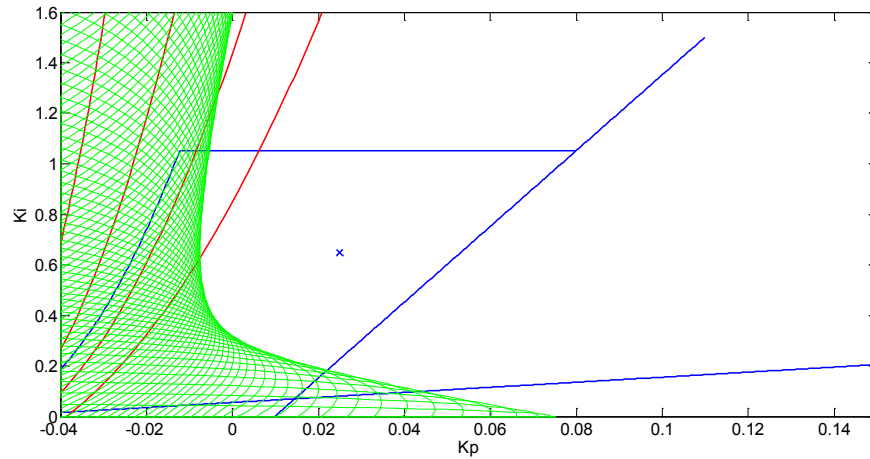


**Figure 2.8 :** Solutions for P1 where  $k_{m,\min} = 0.0402$ ,  $J_{\min} = 17.68 \times 10^{-6}$  (Blue: D-stability boundary, Red: PM boundaries, Green: Mixed sens. req. boundaries).

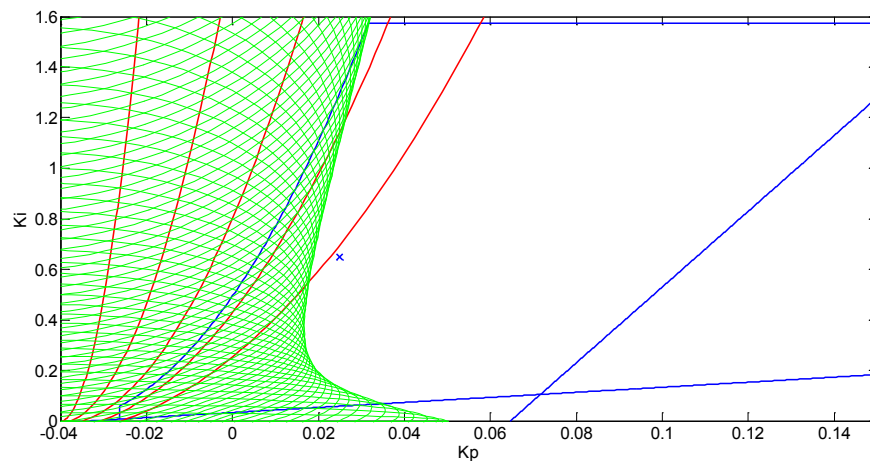
The common  $k_p$  and  $k_i$  were selected as (0.025, 0.65), these points satisfies all design requirements for all operating points. These controller parameters were used in all of the simulations.



**Figure 2.9 :** Solutions for P2 point where  $k_{m,\max} = 0.0602$ ,  $J_{\min} = 17.68 \times 10^{-6}$ .



**Figure 2.10 :** Solutions for P3 point where  $k_{m,\max} = 0.0602$ ,  $J_{\max} = 26.52 \times 10^{-6}$ .



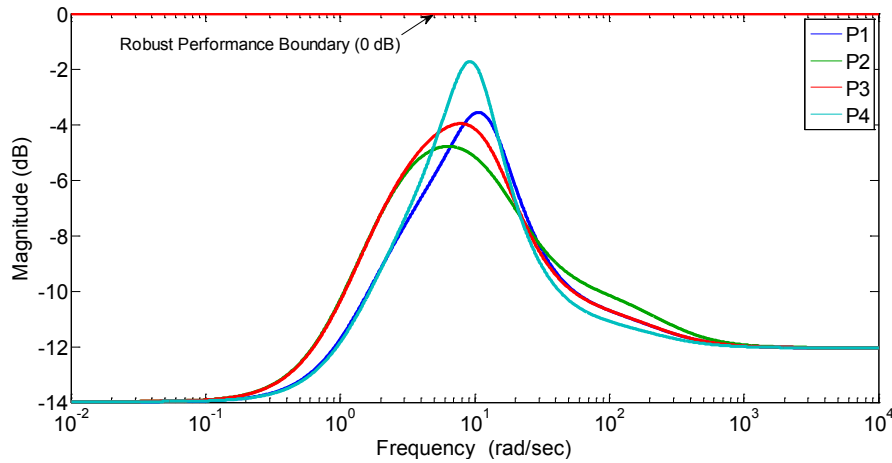
**Figure 2.11 :** Solutions for P4 point where  $k_{m,\min} = 0.0402$ ,  $J_{\max} = 26.52 \times 10^{-6}$ .

Table 2.2 shows the closed loop pole locations and phase margin values for four operating points. The closed loop poles are in the D-stable region and the phase margin requirement is satisfied, all phase margins is larger than 50 degrees.

**Table 2.2 :** Closed loop pole locations and phase margin values for four vertices of the uncertainty box

Points	Closed Loop Pole Locations	Phase Margin (°)
1	$-6.9929 \pm 9.5146i$	61.1032
2	$-13.6842 \pm 4.6411i$	83.5883
3	$-9.1228 \pm 7.4815i$	73.8756
4	$-4.6619 \pm 8.4391i$	51.5451

Figure 2.12 shows the  $|W_S S| + |W_T T|$  frequency-domain plots for all four points as a function of frequency. It is clear from this figure that constraint (2.12) is satisfied at each of the different operating points in Figure 2.3 and for the chosen controller parameters, as none of the plots touch the 0-dB ( $|W_S S| + |W_T T| = 1$ ) line.



**Figure 2.12 :** Robust performance plots  $|W_S S| + |W_T T|$ .

## 2.4 Improvements on System Response using Disturbance Observer

### 2.4.1 Add-on disturbance observer structure

The disturbance observer is a well known approach in the mechatronic systems control area that is used to achieve insensitivity to modeling error and disturbance rejection. It was introduced by [32] and further refined by [33]. It has been used successfully in a variety of mechatronics applications. For instance, friction compensation in [34], road vehicle yaw stability control in [30], robust atomic force microscope control in [35], power assisted electric bicycle control in [36], table drive system in [37] and hard-disc-drive servo system in [38]. In the disturbance observer approach, the inverse of the desired or nominal plant model is used to observe the disturbances and to cancel

the effect of disturbances in the control signal. As a result, the closed system is forced to act like its nominal or desired model. The system structure with add-on disturbance observer is depicted in Figure 2.13.

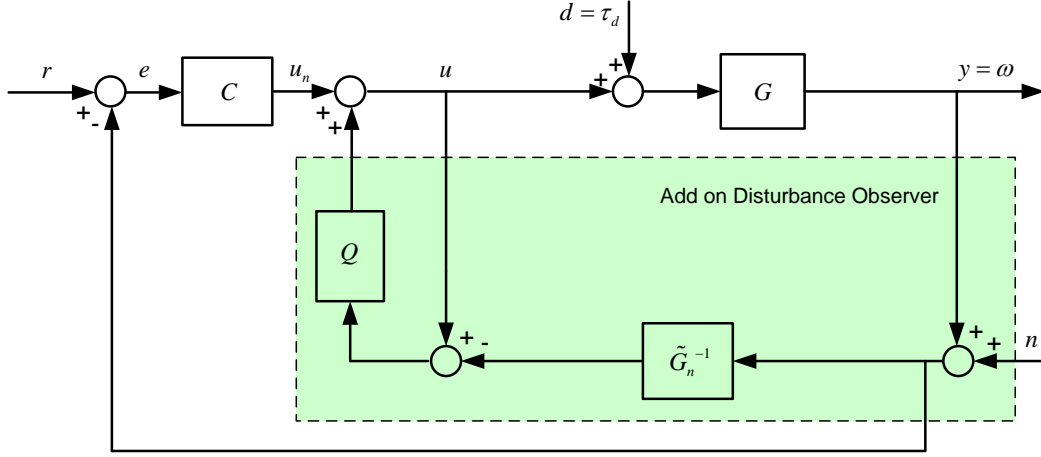


**Figure 2.13** : The system structure with add-on disturbance observer.

Consider plant  $G$  with multiplicative uncertainty  $\Delta_m$  and input disturbance  $d$ :

$$y = G(u + d) \quad (2.23)$$

where  $G = G_n(1 + \Delta_m)$  and  $G_n$  is the nominal model of the plant.

The aim in the disturbance observer usage is to obtain

$$y = G_n u_n \quad (2.24)$$

where  $u_n$  is the new control input.

This aim can be achieved in disturbance observer design by treating the external disturbance and model uncertainty as an extended disturbance  $e$  and solving for it as

$$y = G_n u + \underbrace{G_n d + G_n u \Delta_m + G_n d \Delta_m}_e \quad (2.25)$$

$$e = y - G_n u \quad (2.26)$$

and using the new control signal  $u_n$  given by

$$u = u_n - \frac{1}{G_n} e = u_n - \frac{1}{G_n} y + u \quad (2.27)$$

to approximately cancel its effect when substituted in (2.25). With the aim of not to overcompensate at high frequencies and to avoid stability robustness problems, the

feedback signals in (2.27) are multiplied by the low pass filter  $Q$ . In this case, the final equation becomes

$$u = u_n - Q \left( \frac{1}{G_n} (y + n) + u \right) \quad (2.28)$$

where  $n$  represents the sensor noise, it is available for the case of real implementation.

The disturbance observer can be designed both in continuous time and discrete time. For discrete time design, please refer to [39]. In discrete time implementation, if  $G_n(z)$  is a minimum phase system, its inverse can directly be assigned, if not, stable version of  $\tilde{G}_n^{-1}(z)$  can be obtained using input shaping filter (ISF) designing techniques such as zero phase error tracking control (ZPETC), precision tracking control (PTC), optimal precision tracking control (OPTC).

The loop gain of the disturbance observer compensated plant is

$$L = \frac{GQ}{G_n(1-Q)} \quad (2.29)$$

with the model regulation, disturbance rejection and sensor noise rejection transfer functions given by

$$\frac{y}{u_n} = \frac{G_n G}{G_n(1-Q) + GQ} \quad (2.30)$$

$$\frac{y}{d} = \frac{1}{1+L} = \frac{G_n(1-Q)}{G_n(1-Q) + GQ} \quad (2.31)$$

$$\frac{y}{n} = \frac{-L}{1+L} = \frac{-GQ}{G_n(1-Q) + GQ} \quad (2.32)$$

It is seen that  $Q$  must be a unity gain low pass filter. This choice will result in  $y/u_n \rightarrow G_n$ ,  $y/d \rightarrow 0$  at low frequencies where  $Q \rightarrow 1$  and  $y/n \rightarrow 0$  at high frequencies where  $Q \rightarrow 0$ .

There are limitations in the selection of the bandwidth of the  $Q$  filter. First of all, the bandwidth of the  $Q$  filter cannot exceed the bandwidth of the actuator used. Another limitation for the  $Q$  filter arises from the robust stability requirement.

The characteristic equation of the disturbance observer compensated system can be written

$$G_n(1-Q) + G_n(1+\Delta_m)Q = 0 \quad (2.33)$$

as

$$G_n(1+\Delta_m)Q = 0 \rightarrow Q = -\frac{1}{\Delta_m} \quad (2.34)$$

and note that when the presence of  $\Delta_m$  does not change the number of unstable poles and zeros of  $G$  in comparison to those of  $G_n$ , the application of the Nyquist stability criterion results in

$$|Q| < \left| \frac{1}{\Delta_m} \right|, \forall \omega \quad (2.35)$$

as the necessary and the sufficient condition for robust stability.

The feedback controller  $C$  also affects the robust stability of the overall system. In the presence of the feedback control as shown in Figure 2.13, the closed loop system, disturbance rejection and sensor noise rejection transfer functions can be written as

$$\frac{y}{r} = \frac{CG_n G}{G_n(1-Q) + G(CG_n + Q)} \quad (2.36)$$

$$\frac{y}{d} = \frac{G_n(1-Q)}{G_n(1-Q) + G(CG_n + Q)} \quad (2.37)$$

$$\frac{y}{n} = \frac{-G(CG_n + Q)}{G_n(1-Q) + G(CG_n + Q)} \quad (2.38)$$

In the case of feedback control, the characteristic equation of the closed loop system can be written by

$$G_n(1-Q) + G_n(1+\Delta_m)(CG_n + Q) = 0 \quad (2.39)$$

as

$$G_n(1 + CG_n + \Delta_m(CG_n + Q)) = 0 \rightarrow \frac{Q + CG_n}{1 + CG_n} = -\frac{1}{\Delta_m} \quad (2.40)$$

and using the Nyquist stability criterion results in

$$\left| \frac{Q + CG_n}{1 + CG_n} \right| < \left| \frac{1}{\Delta_m} \right|, \forall \omega \quad (2.41)$$

as the necessary and the sufficient condition for robust stability including feedback control shown in Figure 2.13. Thus, robust stability condition of the system can be investigated in the absence and presence of the feedback control using (2.35) and (2.41), respectively.

## 2.4.2 Disturbance observer design

Using the stability robustness conditions given in (2.35) and (2.41), the cut-off frequency of the low pass  $Q$  filter was determined. The multiplicative uncertainty  $\Delta_m$  is calculated using  $\Delta_m = (G_p - G_n)/G_n$ . Here the plant  $G_p$  was taken different as (2.3) in order to add the effect of the unmodelled dynamics by considering the motor

armature inductance in the investigation of stability robustness. Therefore, the plant model  $G_p$  was taken as follows:

$$G_p(s) = \frac{k_m}{\left(Js + \frac{k_m^2}{R_m}\right)(L_ms + R_m)} e^{-sh} \quad (2.42)$$

Also, time delay  $h$  was considered to reflect the other unmodelled dynamics. Time delay  $h$  was selected as 1.5 times of sampling time. The feedback motor angular speed was calculated based on encoder measurements. Since the angular speed is determined by taking differences of the angles between two sampling intervals, there is a delay of a one sampling time. Also, there is an effect of controller hardware dynamics, it is approximated as an extra delay corresponding to half a sampling time [40].

The uncertainty for  $k_m$  and  $J$  shown in Figure 2.3 was divided into an equally spaced grid of values in both axis directions and the  $1/\Delta_m$  plot shown in Figure 2.14 was obtained. An envelope was drawn to determine the upper bound of the multiplicative uncertainty. Using these plots and considering stability robustness conditions (2.35) and (2.41),  $Q$  was selected as a first order low pass filter of  $1/(\tau_q s + 1)$  with the cut-off frequency of 40 rad/sec.

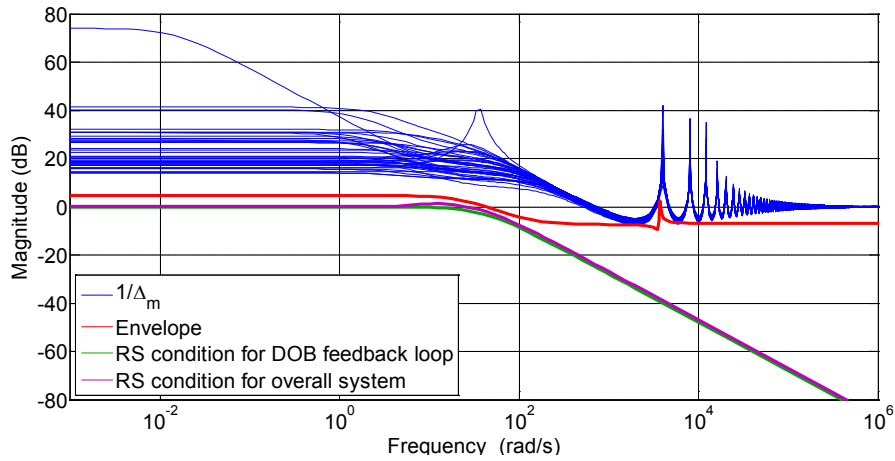


**Figure 2.14 :** Stability robustness plot.

## 2.5 Simulation Results

Simulations were performed to show the effectiveness of the parameter space based fixed robust PI speed controller and the designed add-on disturbance observer. Figure 2.15 and Figure 2.16 show the step input response of desired angular velocity of 100 rad/sec for four operating points shown in Figure 2.3. For simulation shown in Figure

2.15, a step disturbance was applied to the system at  $t = 2 \text{ sec}$  and for simulation shown in Figure 2.16, a ramp disturbance was applied to the system at  $t = 2 \text{ sec}$ . Results show that robust PI plus disturbance observer system rejects step and ramp disturbance successfully and forces the uncertain system to act as nominal plant while satisfying multi-objective design requirements.

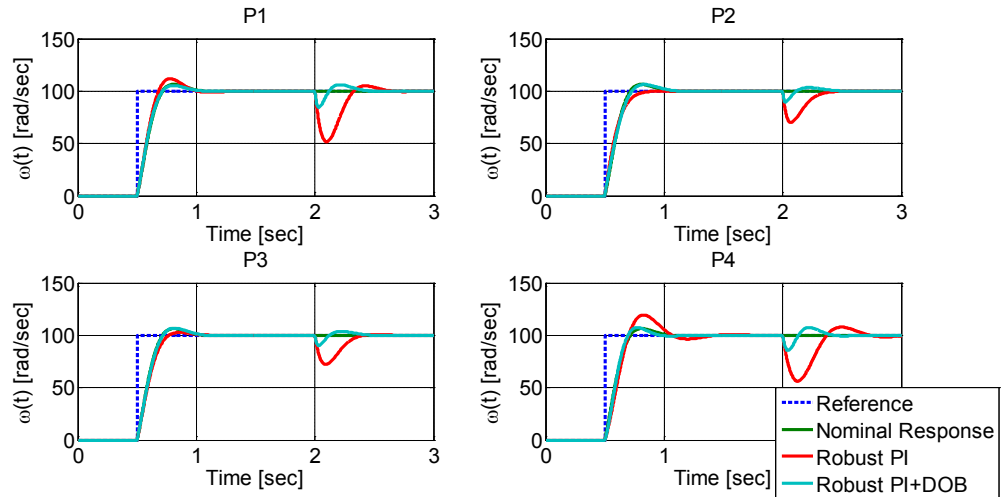


**Figure 2.15 :** Step response and step disturbance rejection simulation results.

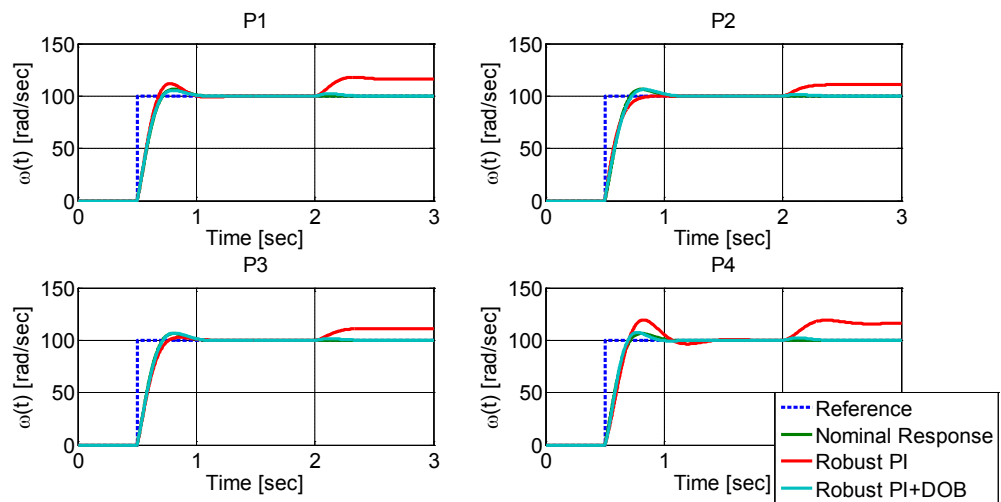


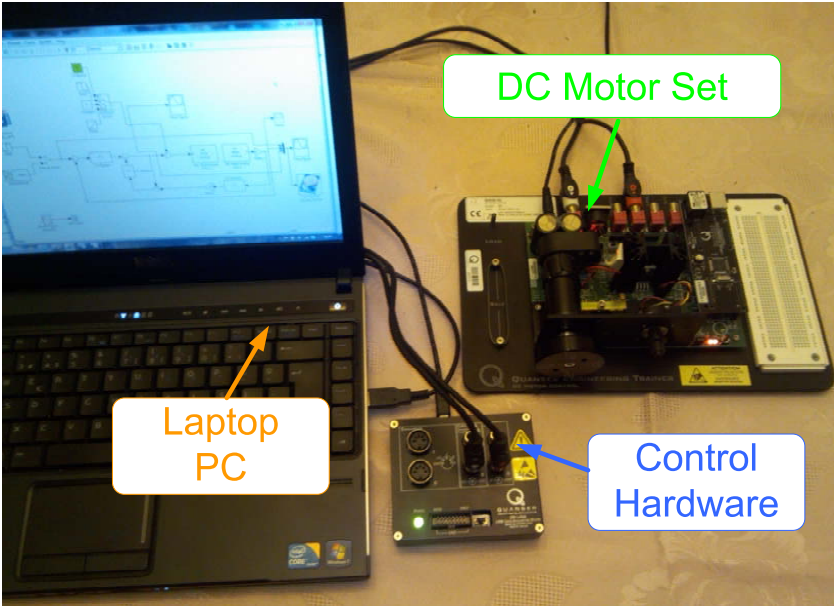
**Figure 2.16 :** Step response and ramp disturbance rejection simulation results.

## 2.6 Experiments

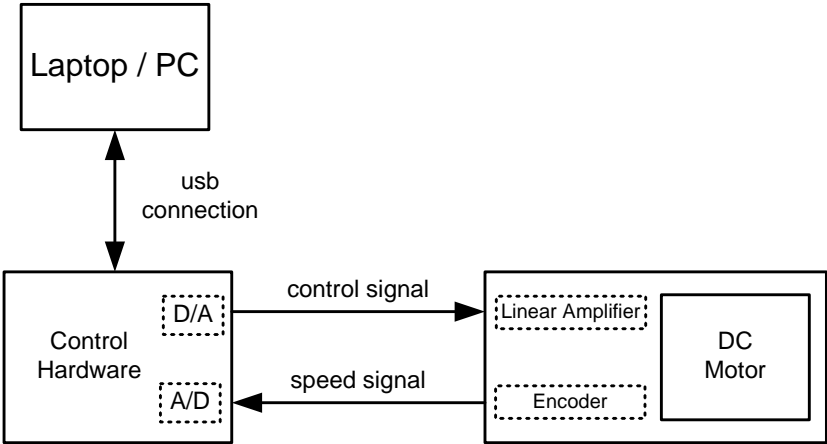
### 2.6.1 Experimental set-up

Figure 2.17 shows the experimental setup. Also, schematic diagram of the experimental setup is depicted in Figure 2.18. The main part of the experimental

setup is a 15 Watt motor of Maxon brand equipped with a quadrature encoder with the resolution of 4096 pulses per revolution. The encoder pulses are received by a 24-bit encoder counter integrated circuit. The angular speed of the motor for feedback is derived from encoder signal. A linear 15 V, 1.5 A power amplifier is used to drive the motor. Quanser Q2-usb board is used as control hardware. The control signal to the DC motor linear amplifier is sent from a 12 bit D/A convertor on Q2-usb board and the angular speed signal is received by a 12 bit A/D convertor on Q2-usb board. The control algorithms is prepared on Matlab/Simulink environment and realized with a 2.27 GHz Intel Core i5 processor Laptop PC. The control algorithms are embedded to Q2-usb board using Matlab Real Time Windows Target and Quanser QUARC software. The DC motor is controlled at the sample rate of 1 kHz.



**Figure 2.17 :** Experimental setup.



**Figure 2.18 :** Schematic diagram of the experimental setup.

## 2.6.2 Experimental results

Three different experiments were conducted in order to test the proposed control scheme. Figure 2.19 shows the trajectory tracking experiment results. The reference motor angular velocity is changing from  $100 \text{ rad/sec}$  to  $50 \text{ rad/sec}$  in  $2 \text{ secs}$  with initial velocity of  $100 \text{ rad/sec}$ . The robust PI plus disturbance observer control system tracks the reference signal with less overshoot with respect to only robust PI control system. However, rise time of the robust PI plus DOB system is longer. When the disturbance observer added to the system, also an extra dynamics inserted to the system, this situation was arisen from this fact.

Figure 2.20 shows the step disturbance rejection test result. At  $t = 10 \text{ sec}$ , the step disturbance was applied to the system. It can be seen that the robust PI plus DOB system attenuated the step disturbance better than only robust PI control system.

Figure 2.21 shows the ramp disturbance rejection test result. The ramp disturbance was injected to the system at  $t = 10 \text{ sec}$ . The only robust PI control system could not attenuate the ramp disturbance but the robust PI plus DOB system dealt with the ramp disturbance successfully.

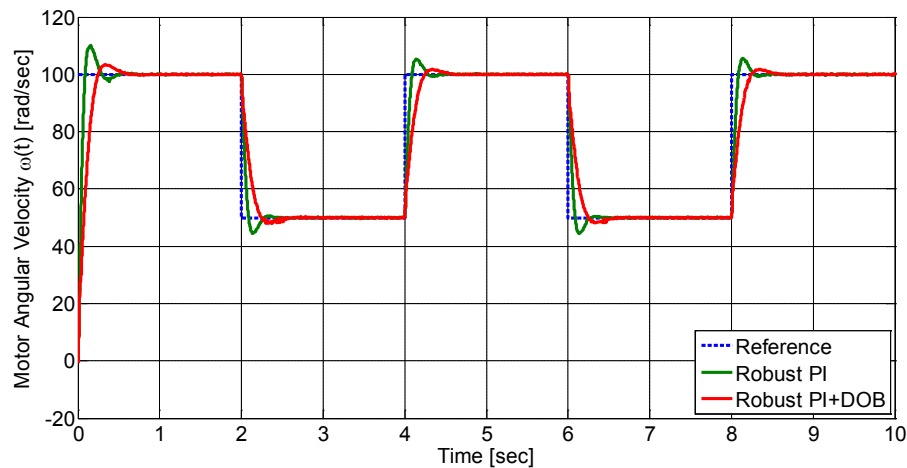


**Figure 2.19** : Trajectory tracking experiment result.

## 2.7 Conclusion

Parameter space approach based robust PI controller and add on disturbance observer design for the DC motor speed control has been presented here. The motor torque constant and total moment of inertia of DC motor has been taken as uncertain parameters. Multi-objective design requirements such as D-stability, phase margin and

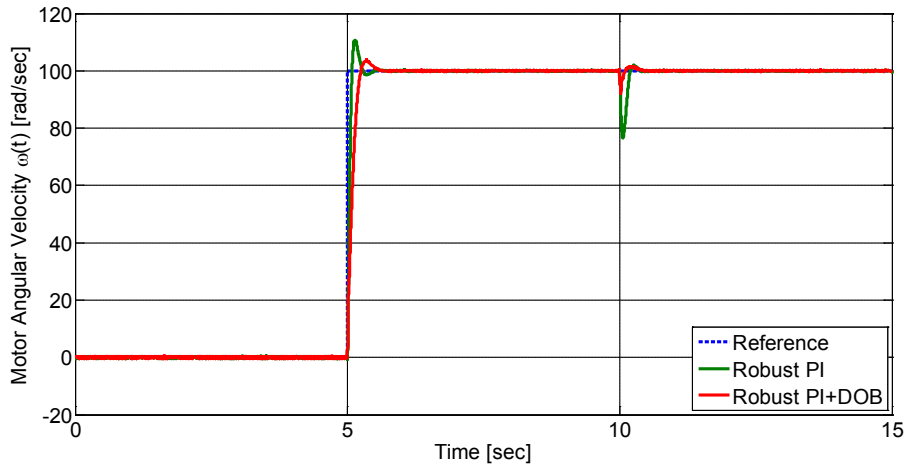


**Figure 2.20 :** Step disturbance rejection experiment result.

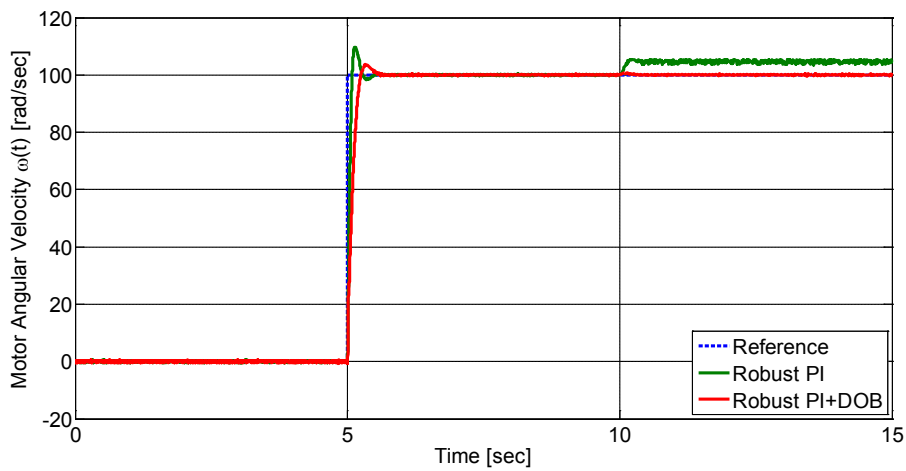


**Figure 2.21 :** Ramp disturbance rejection experiment result.

mixed sensitivity (frequency domain) bounds have been mapped into the controller parameter space to find the robust PI controller coefficients. In order to improve the tracking performance and disturbance rejection properties of the proposed control system, add on disturbance observer has been employed. The disturbance observer design procedure considering stability robustness of the overall system has been given in details. The proposed control system has been tested through simulations and experiments successfully.

### **3. TIME DELAY COMPENSATION USING COMMUNICATION DISTURBANCE OBSERVER APPROACH AND ITS AUTOMOTIVE CONTROL APPLICATION**

#### **3.1 Introduction**

Control of plants that have time delay is a difficult procedure. Time delay adds large negative phase angle to the plant frequency response and tends to destabilize it. There exist a large number of research articles in the literature on time delay systems like references [41] and [42], for example.

The most famous and widely used time delay compensation method is the well known Smith predictor [43]. Smith predictor compensation has been extended for various cases in references [44] and [45]. The Smith predictor and its extensions are simple to understand and are easily implemented. However, use of a Smith predictor requires the model of the time delay and modeling inaccuracies in the knowledge of the time delay element cause degradation of compensation performance.

The disturbance observer is a well known approach in the mechatronic systems control area that is used to achieve insensitivity to modeling error and disturbance rejection. It was introduced by Ohnishi [32] and further refined by Umeno and Hori [33]. It has been used successfully in a variety of mechatronics applications. For instance, friction compensation in [34], road vehicle yaw stability control in [30], robust atomic force microscope control in [35] and power assisted electric bicycle control in [36]. In the disturbance observer approach, the inverse of the desired or nominal plant model is used to observe the disturbances and to cancel the effect of disturbances in the control signal. As a result, the closed system is forced to act like its nominal or desired model. In the literature on the disturbance observer approach, time delayed systems were considered in references [46] and [47].

A compensation method called the communication disturbance observer was introduced to compensate the time delay inherent in bilateral teleoperation systems by Natori et al. [11]. This method was extended to robust time delayed acceleration

control of a single degree of freedom rotary manipulator in [48]. The communication disturbance observer approach differs from the other time delay model based approaches such as the Smith predictor and also the classical disturbance observer as accurate knowledge of the time delay is not necessary. Therefore, this method can be applied even in the case of plants with time delays that are variable.

In this chapter, firstly the communication disturbance observer is applied to a fourth order plant with free integrator and inherent time delay which is an example of an open loop unstable system with time delay. The effect of the  $Q$  filter cut-off frequency selection on the communication disturbance observer is investigated. A novel robust stability condition for the cases of constant and varying time delay is developed based on Nyquist criterion.

Also, the automotive control problems with the time delay is investigated from the point of networked control systems in this chapter. The communication disturbance observer approach is applied to an automotive control problem which suffers from the destabilizing effect of the time varying delay. Using the proposed robust stability condition in the design stage of the communication disturbance observer, the method is employed for the time delay compensation of the vehicle yaw stability control over CAN bus.

The organization of the rest of this chapter is as follows. The communication disturbance observer is introduced in Section 3.2. The communication disturbance observer is applied to a fourth order time delayed process with a free integrator and the results are analyzed in Section 3.3. The robust stability analysis of the communication disturbance observer applied to constant time delayed plants is presented in Section 3.4. Also, a similar analysis in the case of bounded time varying delays is introduced in Section 3.5. The proposed communication disturbance observer approach is applied to the vehicle yaw stability control over CAN bus in Section 3.6. The chapter ends with conclusions in Section 3.7.

### **3.2 Communication Disturbance Observer Structure**

This section firstly presents the classical disturbance observer method for disturbance estimation. Then, the network disturbance concept and the communication disturbance

observer structure are introduced. The closed loop transfer function of the system with the communication disturbance observer is obtained.

### 3.2.1 Classical disturbance observer for disturbance estimation

Consider a nominal plant  $G_n$  with input disturbance  $d$

$$y = G_n(u - d) \quad (3.1)$$

where  $y$  is the output and  $u$  is the input. The aim is to estimate the input disturbance  $d$ . In this case, (3.1) is written as follows:

$$d = u - G_n^{-1}y. \quad (3.2)$$

For causality, the estimated disturbance  $\hat{d}$  is given by

$$\hat{d} = Q(u - G_n^{-1}y) \quad (3.3)$$

where  $Q$  is a low pass filter.

This classical disturbance observer structure for disturbance estimation is illustrated in Figure 3.1.

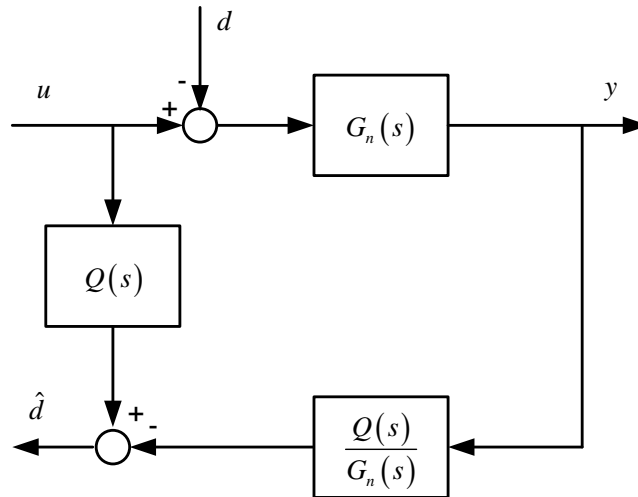


**Figure 3.1** : Classical disturbance observer for disturbance estimation.

### 3.2.2 Network disturbance concept

The structure of the communication disturbance observer is similar to the structure of the disturbance observer except the disturbance definition and time delay compensation. The time delayed system is rewritten using the network disturbance

concept. The effect of the time delay can be expressed as shown in Figure 3.2 where the time delay is seen as a disturbance that is acting on the system.

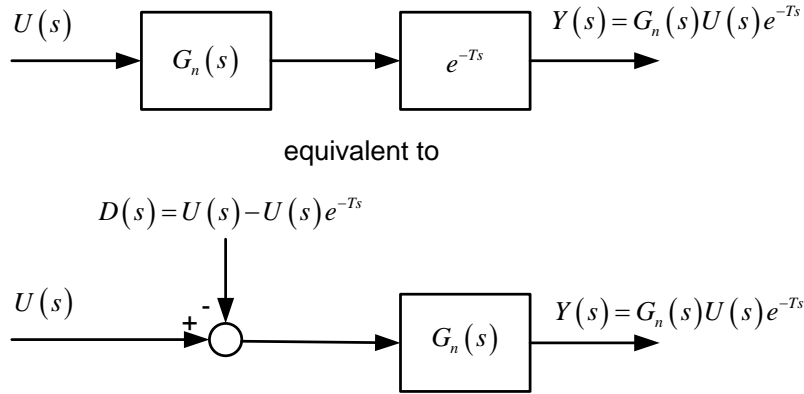


**Figure 3.2 :** Network disturbance concept.

The network disturbance is defined as follows:

$$d(t) = u(t) - u(t - T) \quad (3.4)$$

or in Laplace form

$$D(s) = U(s) - U(s)e^{-Ts} \quad (3.5)$$

where  $u$  is the system input and  $T$  is the time delay.  $D(s)$  is called the network disturbance.

### 3.2.3 Communication disturbance observer

The communication disturbance observer structure is shown in Figure 3.3. It consists of two parts: network disturbance estimation and time delay compensation. The communication disturbance observer estimates the network disturbance according to (3.3). This estimated disturbance is used to compensate the time delay effect in the feedback signal.

As our knowledge of the nominal plant  $G_n$  may have uncertainty in it, the nominal plant in the top path in Figure 3.3 is better represented by  $G = G_n(1 + \Delta_m)$  where  $\Delta_m$  represents the uncertainty in our knowledge of the plant. With this change, the closed loop system transfer function is given by

$$\frac{y}{r} = \frac{CGe^{-Ts}}{1 + CG_nQ + CGe^{-Ts}(1 - Q)} \quad (3.6)$$

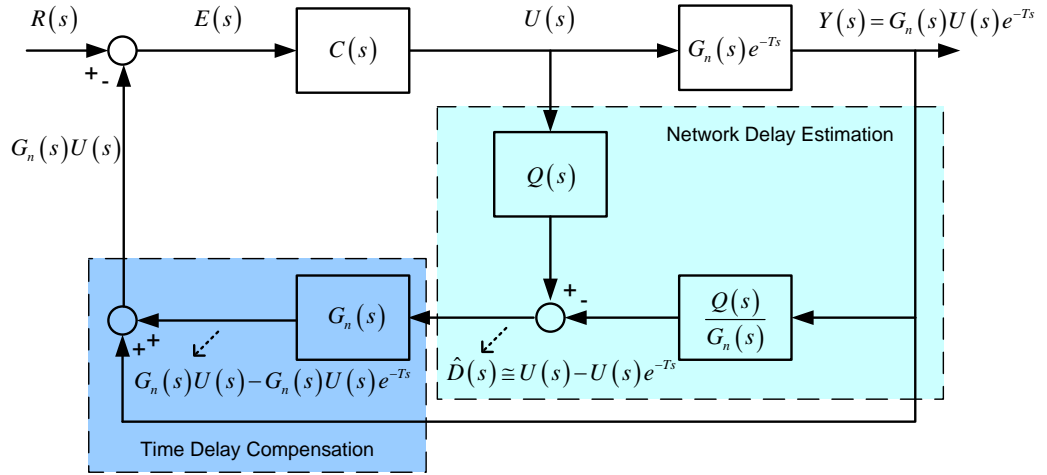


**Figure 3.3 :** Communication disturbance observer structure.

If  $Q$  is selected as a unity gain low pass filter, this choice will result in no time delay element in the denominator of the transfer function. In this way, the time delay is compensated by the communication disturbance observer.

### 3.3 Communication Disturbance Observer based Time Delayed Integral Plant Control

Since integral plants with time delay are a special case of the unstable time delayed systems, there have been many researchers who were interested in this topic [47], [49] and [50]. In this section, the communication disturbance observer approach is applied to the control of time delayed integral plants.

Consider the following time delayed single integrator plant:

$$G_p(s) = G(s)e^{-Ts} = \frac{G_0(s)}{s}e^{-Ts} \quad (3.7)$$

where  $T$  is a pure time delay and  $G_0(s)$  is a strictly proper, minimum phase and Hurwitz transfer function  $G_0(0) \neq 0$ .

The communication disturbance observer based control scheme is shown in Figure 3.3 and its equivalent sequential block diagram transformation for implementation is shown in Figure 3.4. The nominal model  $G_n(s)$  is a low order approximation of  $G(s)$ . The controller  $C(s)$  is designed for the nominal model  $G_n(s)$  which does not have a time delay. The low pass filter  $Q(s)$  is designed to compensate for the time delay within its bandwidth and to satisfy robust stability of the system.

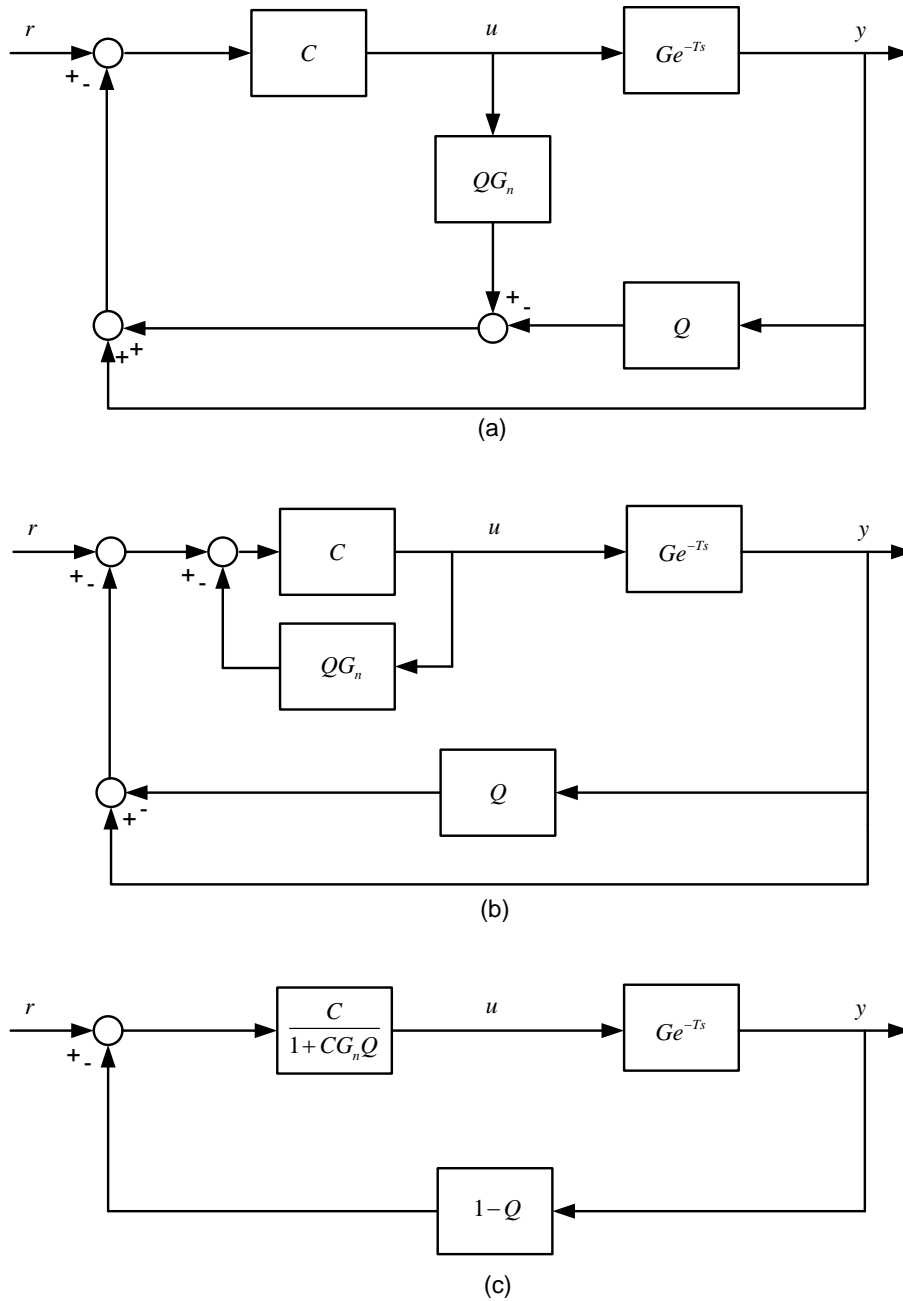


**Figure 3.4 :** Equivalent block diagram transformation.

The fourth order time delayed integral plant with one integrator

$$G_p(s) = \frac{1}{s(0.5s+1)(0.15s+1)^2} e^{-Ts} \quad (3.8)$$

is used as an example to illustrate the effectiveness of the communication disturbance observer. The controller  $C(s)$  can be designed according to the nominal model  $G_n(s) = 1/(s(0.5s+1))$  where the term  $1/(0.15s+1)^2$  in the plant model (3.8) is treated as modeling error. The nominal model is the low order approximation of (3.8). Here,  $C(s)$  is chosen as a proportional controller with  $C(s) = 0.5$  in order to obtain short settling time and no overshoot.  $Q = \omega_c/(s+\omega_c)$ , where the cut-off frequency  $\omega_c$  is chosen to

obtain time delay compensation up to that frequency. The unit step response for this plant is shown in Figure 3.5 with and without the communication disturbance observer when the time delay is  $T = 3 \text{ sec}$ . Here, the cutoff frequency  $\omega_c$  of the low pass filter  $Q(s)$  is selected as  $100 \text{ rad/sec}$ . It is seen that the process with communication disturbance observer is stable. Communication disturbance observer compensates the time delay effect on the closed loop system.

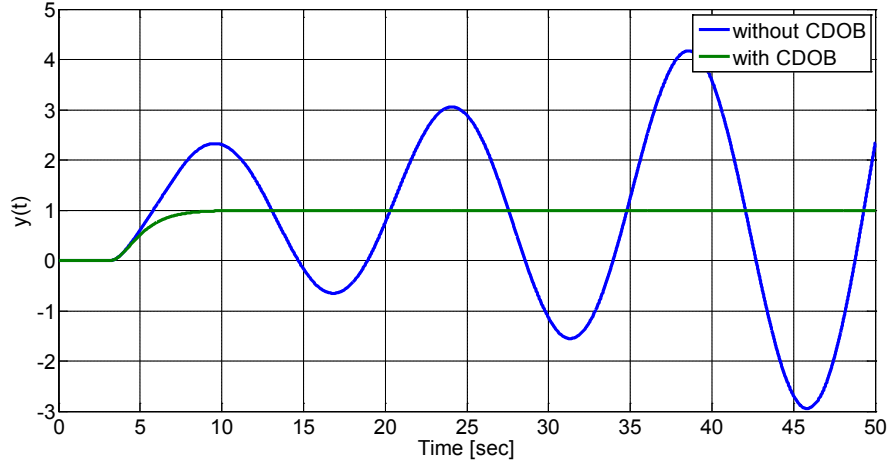


**Figure 3.5 :** Step response of the time delayed integral plant without/with communication disturbance observer.

Figure 3.6 shows the step responses of the plant (3.8) for different values of time delay, under the action of the communication disturbance observer. The cut-off frequency is selected as  $100 \text{ rad/sec}$  again for these simulations. The time delayed integral process is stable for long dead times such as 3, 5, 7, 10 and 15 secs. Also, it can be seen that there is no overshoot for these time delay values.

The Nyquist plot is drawn for different values of  $\omega_c$  in Figure 3.7 when the time delay is  $T = 5 \text{ sec}$ . The unstable behavior of the closed loop system can be seen when the communication disturbance observer is not used. Also, the importance of the selection of  $\omega_c$  is seen. When the cutoff frequency  $\omega_c$  is increased, the gain margin of the system is intensified.

### 3.4 Robust Stability Analysis in the case of Constant Time Delay

For an uncertain system, the uncertain plant model  $G(s)$  can be represented using multiplicative uncertainty as follows:

$$G(s) = G_n(s) (1 + \Delta_m(s)), \forall \omega \quad (3.9)$$

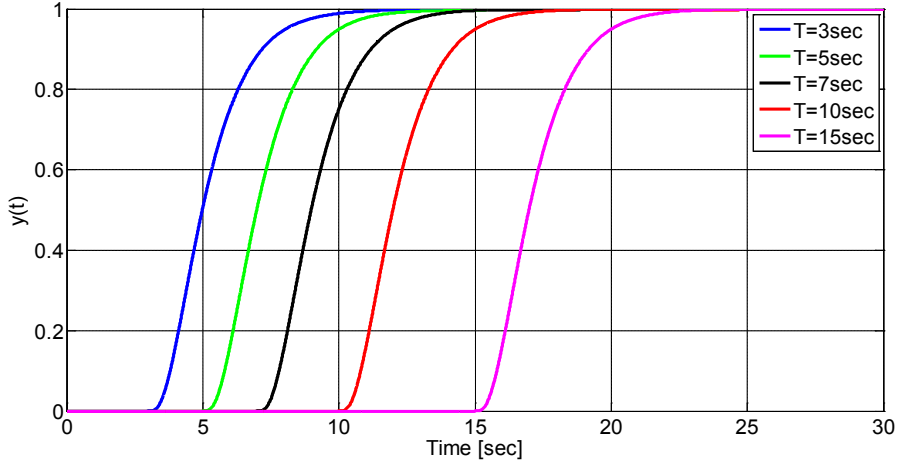


**Figure 3.6 :** Step responses of the time delayed integral plant for different delay values.

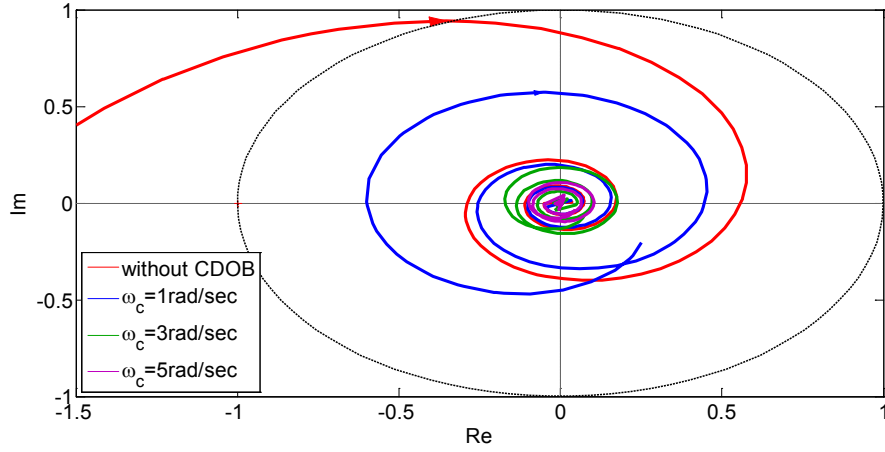


**Figure 3.7 :** Nyquist plots for different cutoff frequencies  $\omega_c$  of  $Q(s)$ .

where  $G_n(s)$  is the nominal model and  $G(s)$  denotes a family of models that deviate no more than the multiplicative uncertainty  $\Delta_m(s)$ .

A system with multiplicative uncertainty is depicted in Figure 3.8. For this system, the loop transfer function is written as

$$L = KG = KG_n(1 + \Delta_m) = L_n + L_n\Delta_m \quad (3.10)$$

where,  $K$  is the controller and  $L_n = KG_n$  is the nominal loop transfer function.

If we assume that the nominal closed loop system is stable, robust stability of the uncertain system can be guaranteed if  $L$  does not encircle the point  $(-1, 0)$  according to Nyquist stability criterion. Figure 3.9 depicts this robust stability condition.

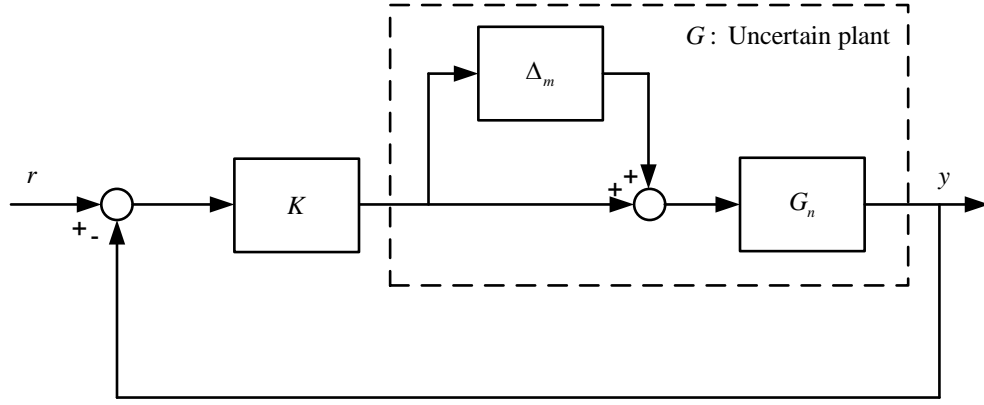


**Figure 3.8 :** Feedback controlled plant with multiplicative uncertainty.

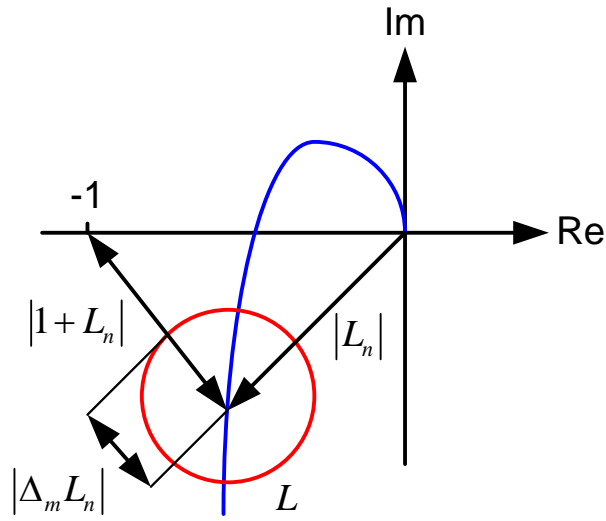


**Figure 3.9 :** Nyquist plot for illustrating robust stability condition.

This condition can be expressed as follows:

$$|\Delta_m(j\omega)L_n(j\omega)| < |1 + L_n(j\omega)|, \forall \omega \quad (3.11)$$

or equivalently

$$\left| \frac{\Delta_m(j\omega)L_n(j\omega)}{1 + L_n(j\omega)} \right| < 1, \forall \omega \Leftrightarrow \|\Delta_m T_n\|_\infty < 1 \quad (3.12)$$

where  $T_n$  is the nominal complementary sensitivity function.

Using the equivalent system in Figure 3.4 (c) and incorporating the feedback loop term into the controller, the controller  $K$  for the communication disturbance observer based control can be represented as

$$K = \frac{C(1-Q)}{1 + CG_nQ}. \quad (3.13)$$

The nominal loop transfer function for the system is written as

$$L_n = KG_n e^{-Ts} = \frac{C(1-Q)G_n e^{-Ts}}{1 + CG_nQ}. \quad (3.14)$$

Using (3.14), the nominal complementary sensitivity function is given by

$$T_n = \frac{L_n}{1+L_n} = \frac{CG_n e^{-Ts} (1-Q)}{1+CG_n Q + CG_n e^{-Ts} (1-Q)}. \quad (3.15)$$

As a result, the robust stability condition in (3.12) can be written for communication disturbance observer based controlled system as:

$$\left| \frac{CG_n e^{-Ts} (1-Q)}{1+CG_n Q + CG_n e^{-Ts} (1-Q)} \right| < \left| \frac{1}{\Delta_m} \right|, \forall \omega \quad (3.16)$$

To illustrate the effects of time delay, assume that  $e^{-Ts}$  is the only source of unmodeled dynamics. Thus, the multiplicative uncertainty model can be represented as

$$\Delta_m(s) = e^{-Ts} - 1. \quad (3.17)$$

Consider the following time delayed basic integral plant for robust stability analysis:

$$G_p(s) = \frac{1}{s} e^{-Ts}. \quad (3.18)$$

The nominal model  $G_n$  is equal to  $1/s$ . Time delay  $T$  is taken as  $0.2 \text{ sec}$ . The controller  $C(s)$  is a proportional controller, it is equal to 20 in order to satisfy short settling time and no overshoot design requirements.

The robust stability condition (3.16) is investigated for different cut frequencies of  $Q(s)$ . The results are given in Figure 3.10. It is seen that the uncertainty and robust stability lines intersected for  $\omega_c = 10 \text{ rad/sec}$ . For this value, the feedback controlled integral plant may be unstable. For the other values of cut-off frequency, the system is stable. If we increase the cut-off frequency, the stability margin is increased. However, noise issues may restrict this frequency selection in real applications. Figure 3.11 depicts the step responses of the same plant for different cut-off frequencies of  $Q(s)$ . It is clear that the higher cut-off frequency selection improves the transient response of the process.

### 3.5 Robust Stability Analysis in the case of Bounded Time Varying Delay

The communication disturbance observer can also be used when the time delay is varying. In the case of time varying delay, the robust stability condition in (3.16) becomes

$$\left| \frac{CG_n e^{-T_{\max} s} (1-Q)}{1+CG_n Q + CG_n e^{-T_{\max} s} (1-Q)} \right| < \left| \frac{1}{e^{-T_{\max} s} - 1} \right|, \forall \omega. \quad (3.19)$$

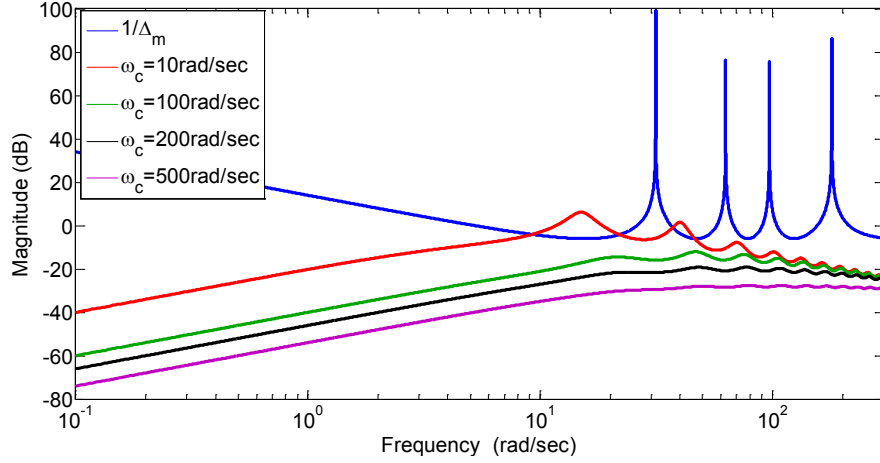


**Figure 3.10 :** Stability of robustness for the time delayed integral plant with communication disturbance observer.

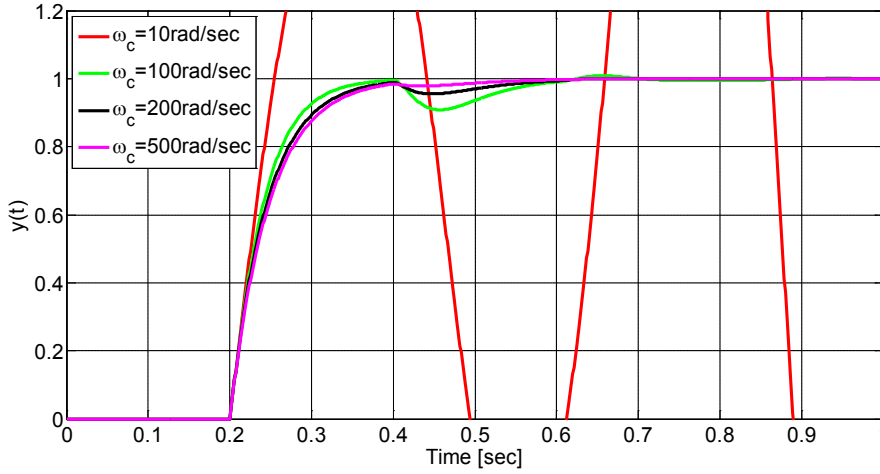


**Figure 3.11 :** Step responses of the time delayed integral plant for different cut-off frequencies  $\omega_c$  of  $Q(s)$ .

The unity gain low pass  $Q$  filter can be designed considering the restriction of the time delay upper bound  $T_{max}$  with some conservatism. Below, a numerical example is given to show the effectiveness of the communication disturbance observer in the case of time varying delay.

Consider the following single input – single output time varying delay system for robust stability analysis:

$$\dot{x}(t) = Ax(t) + bu(t) \quad (3.20)$$

$$y(t) = c^T x(t - T(t)) \quad (3.21)$$

where  $x$  is the state,  $T(t)$  is an bounded time varying delay such that  $T_{min} \leq T(t) \leq T_{max}$ .

For simplicity and coherence with the constant time delay example,  $A = [0]$ ,  $b = [1]$  and  $c = [1]$  which corresponds to an integrator are used. This example system is the same as the previous one except for the presence of the time varying delay. The nominal plant and the controller are the same as those of the previous example.

Figure 3.12 shows the time delay  $T(t)$  varying between 0.1 and 0.4 secs. The robust stability condition (3.19) is shown in Figure 3.13 for two different cut-off frequencies of the  $Q$  filter. For  $\omega_c = 100 \text{ rad/sec}$ , the feedback controlled integrator plant with time varying time delay under communication disturbance observer control is stable. The step responses of the system for different cut-off frequencies and for the case of no communication disturbance observer are illustrated in Figure 3.14. The stability of the system with communication disturbance observer is also seen from this figure when appropriate selection of cut-off frequency of  $Q$  filter is realized.

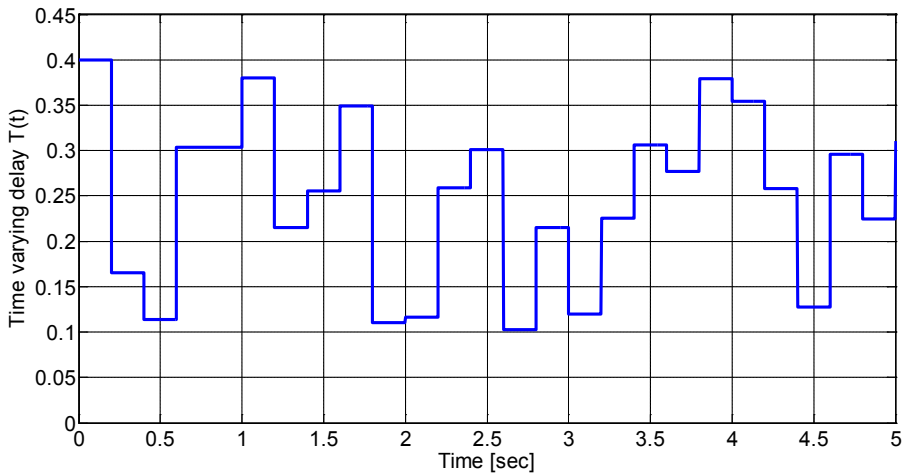


**Figure 3.12 :** Time varying delay  $T(t)$ .

### 3.6 Application to Yaw Stability Control over CAN Bus

Time delay occurs and causes stability problems in many automotive control systems such as idle speed control, air-to-fuel ratio control, anti-jerk control, cooperative adaptive cruise control and other controller area network (CAN) based distributed control systems in vehicle.

In idle speed control, the delay is due to the intake-to-combustion stroke delay. This delay should not be neglected, since it often constitutes the dominant dynamics of the

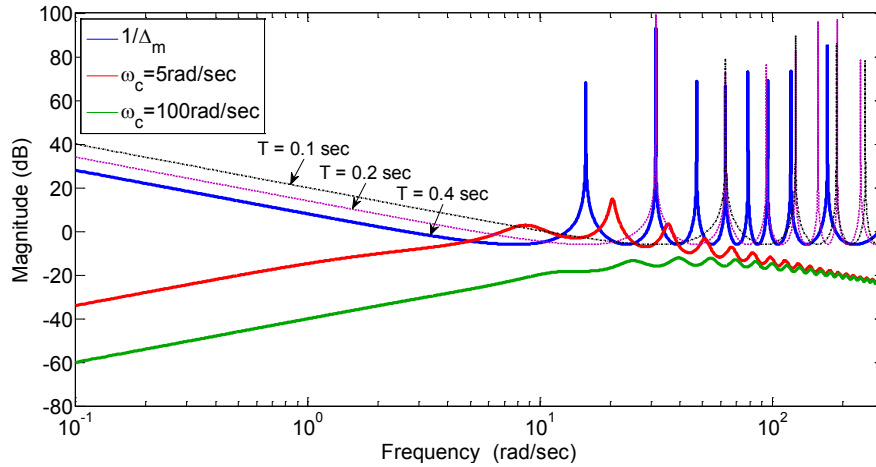


**Figure 3.13 :** Stability of robustness for the time varying delayed integral plant with communication disturbance observer.

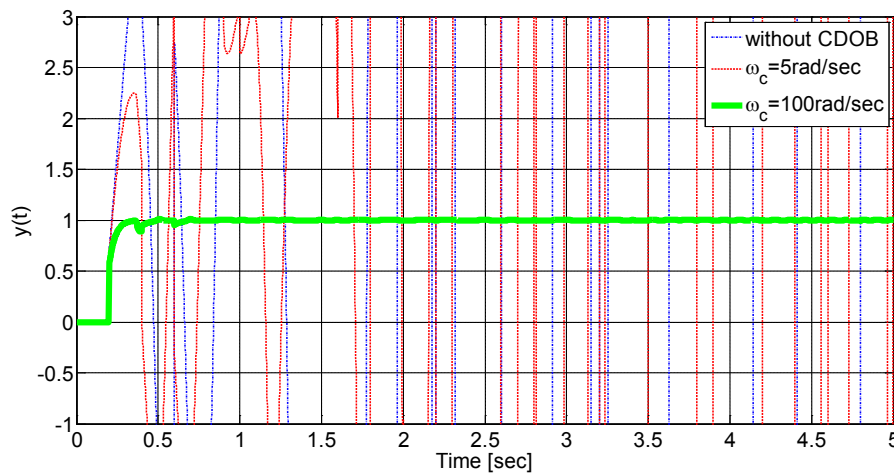


**Figure 3.14 :** Step responses of the time varying delayed integral plant for different cutoff frequencies  $\omega_c$  of  $Q(s)$ .

resulting closed-loop system [51, 52]. Different control methodologies applied to the idle speed control in the literature such as model predictive control [53].

Air-to-fuel ratio control is very important for gasoline vehicles in order to achieve emission regulations. The delay between fuel injection and universal exhaust gas oxygen sensor measurement can be a limiting factor seriously degrading the achievable performance of the air-to-fuel ratio feedback loop [52].

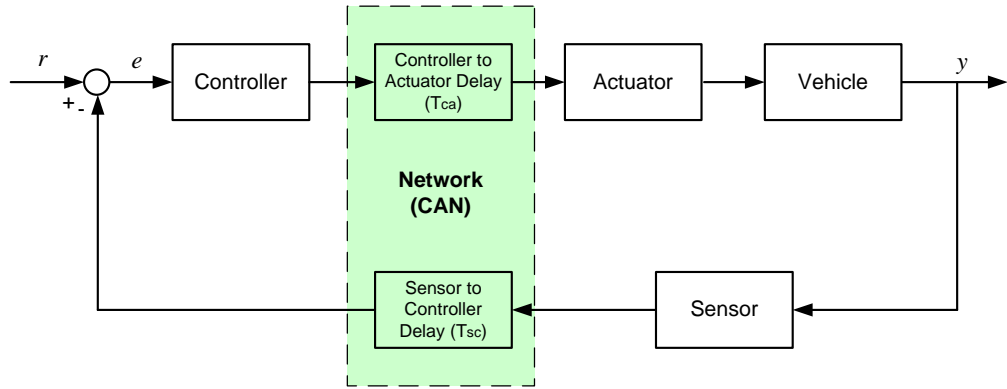
Modern diesel engines with direct fuel injection generate a high engine torque at very low engine speeds. One problem with this high engine torque is the torsion of the drivetrain which causes drivetrain oscillations. Anti-jerk control is required to avoid these oscillations and to improve the comfort of the passengers. The

drivetrain system has an inherent time delay caused by the engine. To compensate this behavior, modified Smith Predictor can be used which provides the predictive model output. Using the predictive model output as controller input gives the possibility to avoid jerking before its occurrence and therefore minimizing the oscillations in the drivetrain [54].

Cooperative adaptive cruise control (CACC) is an extension of adaptive cruise control (ACC). The aim in ACC is to reduce headway time as much as possible, without violating string stability. CACC extends the capability of standard ACC by communicating information about the state of the preceding vehicle, thereby reducing the headway time used in standard ACC [55]. In CACC, the delay raises from communication among vehicles. Vehicles send location, speed and acceleration data via modems. The robustness of the cooperative adaptive cruise controller against network-induced delays was investigated in [56]. According to this research, high bandwidth controllers are desirable for better asymptotic tracking, but from a string stability point of view, this choice impairs the robustness of the controller against communication delays.

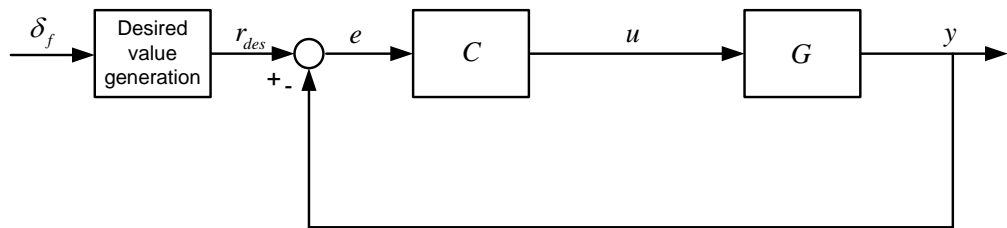
Active safety systems in vehicles such as ABS, TCS, ESC employ to improve the safety of the passengers. These systems use sensor information in order to make decisions and control actuators. These systems generally work through the communication networks such as Controller Area Network (CAN). CAN is a serial communications protocol which efficiently supports embedded distributed real time control systems with a very high level of security. For further information, please see [57]. Networked control systems provide safety, flexibility, cost efficiency and easy manageability in complicated systems such as automobiles, airplanes. However, the limited bandwidth and the introduction of the communication network into the closed loop system can cause problems such as network-induced delays which can result in instability and performance degradation of the control system [58].

Figure 3.15 shows the basic elements of networked control systems in vehicle. There are two network-induced delays: controller to actuator delay ( $T_{ca}$ ) and sensor to controller delay ( $T_{sc}$ ). In this section, communication disturbance observer approach is used to compensate these network-induced delays for yaw stability control of the vehicle.

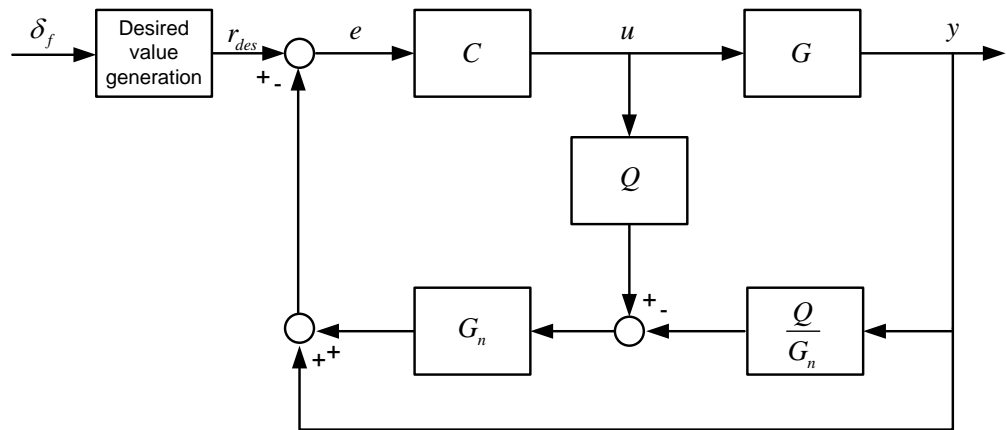


**Figure 3.15 :** The basic elements of networked control system in vehicle.

Figure 3.16 shows the yaw stability control systems without and with communication disturbance observer. In yaw stability control, the aim is to control the yaw rate according to the desired yaw rate. This desired value can be calculated using the front wheel steering angle  $\delta_f$  and single track vehicle model in desired value generation block. The obtained yaw rate error  $e$  used by the controller  $C$  to generate the controller signal  $u$ . Here, the controller  $C$  is designed as PI controller.



(a)



(b)

**Figure 3.16 :** The yaw stability control system block diagrams: (a)without CDOB, (b)with CDOB.

The nominal transfer function  $G_n$  from the front wheel angle  $\delta_f$  to the yaw rate  $r$  derived from linearized single track vehicle model can be written as follows [9]:

$$G_n(s) = \frac{r(s)}{\delta_f(s)} = \frac{b_1s + b_0}{a_2s^2 + a_1s + a_0} \quad (3.22)$$

where  $b_1 = \mu c_f l_f m V^2$ ,  $b_0 = \mu^2 c_f c_r (l_f + l_r) V$ ,  $a_2 = J m V^2$ ,  $a_1 = \mu (c_f (J + l_f^2 m) + c_r (J + l_r^2 m)) V$ ,  $a_0 = \mu^2 c_f c_r (l_f + l_r)^2 + \mu (c_r l_r - c_f l_f) m V^2$ .

Here,  $\mu$  is the tire-road friction coefficient,  $m$  is the vehicle mass,  $J$  is the moment of inertia,  $c_f$  and  $c_r$  are the cornering stiffnesses,  $l_f$  is the distance from the center of gravity of the vehicle (CG) to the front axle and  $l_r$  is the distance from the CG to the rear axle. The values of the parameters used are  $m = 1296 \text{ kg}$ ,  $J = 1750 \text{ kgm}^2$ ,  $l_f = 1.25 \text{ m}$ ,  $l_r = 1.32 \text{ m}$ ,  $c_f = 84000 \text{ N/rad}$  and  $c_r = 96000 \text{ N/rad}$ . Note that the uncertain vehicle transfer function  $G$  in Figure 3.16 denotes the nominal transfer function and added time delay effects from the network communication.

The time varying network-induced delay in CAN consists of the sum of the controller to actuator delay  $T_{ca}$  and the sensor to the controller delay  $T_{sc}$ . The total time varying delay can be taken as between  $6 \text{ ms}$  and  $20 \text{ ms}$  [58]. Figure 3.17 shows the bounded time varying delay  $T(t)$  used in simulations.

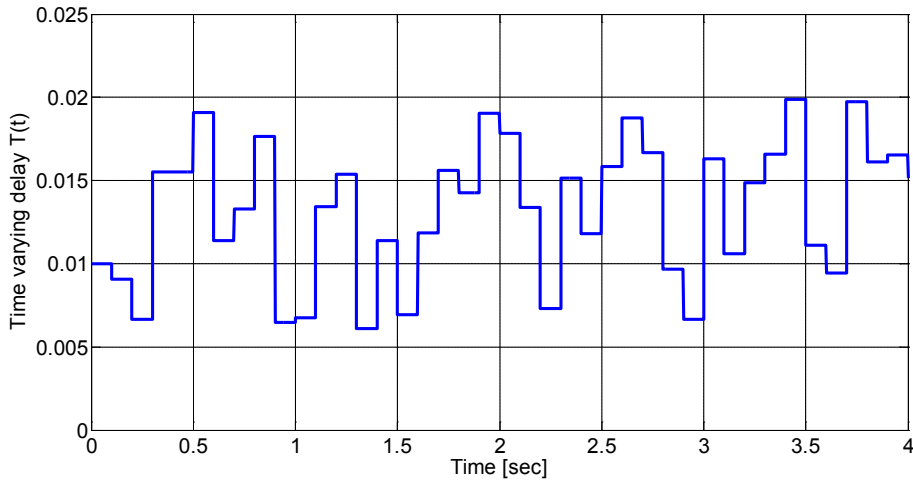


**Figure 3.17 :** Time varying delay  $T(t)$  in CAN communication.

The unity gain low pass  $Q$  filter can be designed considering the robust stability condition for the bounded time varying delay given in (3.19). This condition is depicted in Figure 3.13 for the  $Q$  filter with the cut-off frequency of  $600 \text{ rad/sec}$ . It is seen that the uncertainty and robust stability lines do not intersect each other for  $\omega_c = 600 \text{ rad/sec}$ . The feedback controlled system is stable for the selected

cut-off frequency. Note that the uncertain vehicle model  $G = G_n(1 + \Delta_m)$  and the multiplicative uncertainty  $\Delta_m$  can be represented here as  $e^{-T_{max}} - 1$  to illustrate only the effects of the time delay on robustness.

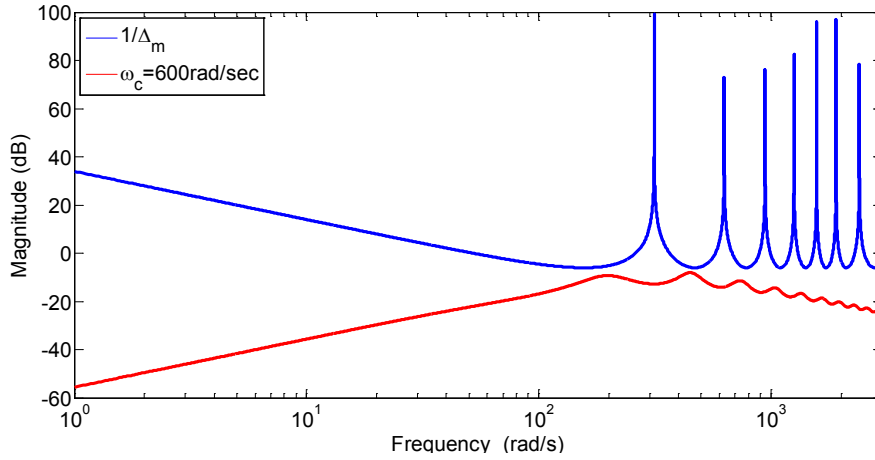


**Figure 3.18 :** Stability of robustness for the time varying delayed yaw stability control system with communication disturbance observer.

A simulation is performed to test the effectiveness of the communication disturbance observer. In simulation, the magnitude of 8 *deg* front wheel steering input is applied to the vehicle at constant velocity of 30 *m/s*. The tire-road friction coefficient  $\mu$  is selected as 1. The responses of desired yaw rate, the yaw rate of the only PI controlled vehicle and the yaw rate of the PI controlled vehicle with communication disturbance observer is illustrated in Figure 3.19. It can be seen that time varying delay causes instability in the case of only PI control but in the case of add-on communication disturbance observer, the vehicle becomes stable and also the yaw rate of the vehicle follows the desired yaw rate successfully. The designed communication disturbance observer compensates the negative effect of the network-induced delay.

### 3.7 Conclusion

In this chapter, the communication disturbance observer approach was introduced and it was applied to time delayed systems using a fourth order plant with a free integrator, an integrator only plant and the vehicle yaw stability control problem as examples. The method was verified for different time delay values. The effect of the  $Q$  filter cut-off frequency selection was investigated. As a result, the enhancement of gain margin with the increasing of disturbance observer cut-off frequency was observed. A robust stability condition was derived based on the Nyquist criterion for the constant

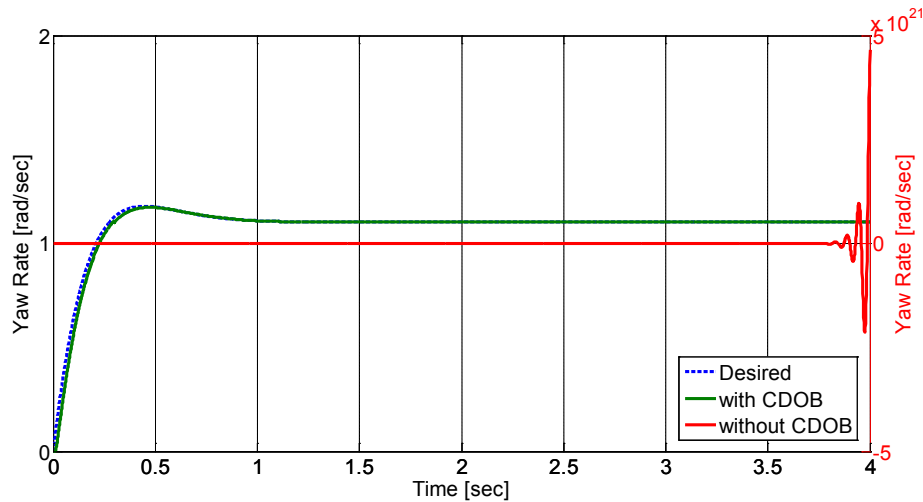


**Figure 3.19 :** Simulation results for the yaw stability control system with and without CDOB.

time delay values. The robust stability of a constant time delayed integral plant was examined for different selection of cut-off frequencies. Also, this robust stability criterion was applied to the case of time varying delay integral plant using the upper bound of the time varying delay in the analysis, resulting in a conservative result.

The effectiveness of the approach was illustrated by simulations both for constant and time varying cases for different problems. It was applied to the vehicle yaw stability control problem for compensating time varying CAN bus delay. It was observed that time varying delay is compensated successfully by the use of add-on communication disturbance observer. In general, the method was found to be simple and implementable. The time delay compensation without the necessity of time delay and dealing with the time varying delay are the most important advantages of the method over Smith predictor and classical disturbance observer approach for the time delay systems. It can be found many application areas in the area of automotive control.

## **4. ROBUST PID STEERING CONTROL IN PARAMETER SPACE FOR HIGHLY AUTOMATED DRIVING**

### **4.1 Introduction**

In recent years, intelligent vehicle systems and highly automated driving technologies have drawn interests among researchers. Many research efforts including for example the work of [59], [55] and [60] have concentrated on semi-autonomous and fully autonomous vehicles. Autonomous driving requires the coordinated automation of the longitudinal and lateral driving tasks of speed control and steering control, respectively. Desired path tracking of an autonomous vehicle requires the proper design and implementation of steering and speed controllers at the lower control level. This chapter concentrates on automated robust steering control.

The basic automatic steering control algorithms found in the literature are based on proportional type controllers [61] and [62]. In these designs, the lateral deviation of the vehicle at a preview distance is fed back for controlling the vehicle's lateral dynamics. In [63], a robust PIDD controller is designed for automatic bus steering control as a solution of a benchmark problem. The yaw rate is measured in addition to lateral deviation measurements and is fed back for improving the control system performance. For the same benchmark problem, a discrete time add-on disturbance observer design is realized in [39]. Using the add-on disturbance observer, the performance improvement is achieved without the need for yaw rate feedback. Another approach to automatic steering controller is to design nested PI and PID controllers. A PI steering controller that reduces yaw rate tracking error is used to improve the vehicle steering dynamics and a PID controller is employed to reject the lateral deviation from the desired path due to road curvature disturbance in [64].

In this chapter, the parameter space approach based PID controller design is applied to robust automatic steering control. The theoretical background about the parameter space approach and an example of road vehicle yaw stability control can be found

in references [9], [30] and [31]. The parameters exhibiting the largest variation in automatic steering control are taken as uncertain parameters, which are the vehicle mass, the vehicle velocity and tire-road friction coefficient. In this chapter, the controller parameter space is obtained considering D-stability requirements for the two free coefficients of a PID controller chosen as the proportional gain  $k_p$  and the derivative gain  $k_d$ . An overall solution region is calculated by intersecting solution regions for exemplary points chosen from the boundary of the uncertain range of parameters. Robust PID coefficients satisfying D-stability are chosen from the overall calculated parameter space regions. The designed controller is applied to an experimentally validated nonlinear simulation model of a sedan vehicle.

Also, robust PID automatic steering control system design is realized based on the digital map and GPS measurements. In this structure, the lateral deviation from the desired path at the preview distance is calculated by comparing the generated map and the vehicle position in real time. The high resolution digital map generation by using the constrained least square method is introduced. The proposed control system is tested with the validated nonlinear vehicle model on a specific eight segments desired path.

The organization of the rest of this chapter is as follows. In Section 4.2, the linear vehicle model used in controller design and the experimental vehicle that it is based on are described. The nonlinear model of this experimental vehicle and model validation results are also presented in Section 4.2. In Section 4.3, robust PID controller design based on mapping D-stability boundaries into parameter space is given. Simulation results in Section 4.4 illustrate the effectiveness of the designed controller. In Section 4.5, digital map and GPS measurements based robust PID steering control is described and the effectiveness of the method is demonstrated by the help of the simulations. The chapter ends with conclusions in Section 4.6.

## **4.2 Vehicle Models and Model Validation**

### **4.2.1 Vehicle steering model**

The vehicle steering behavior is modeled as single track model that also includes the dynamics of following the reference path as illustrated in Figure 4.1.

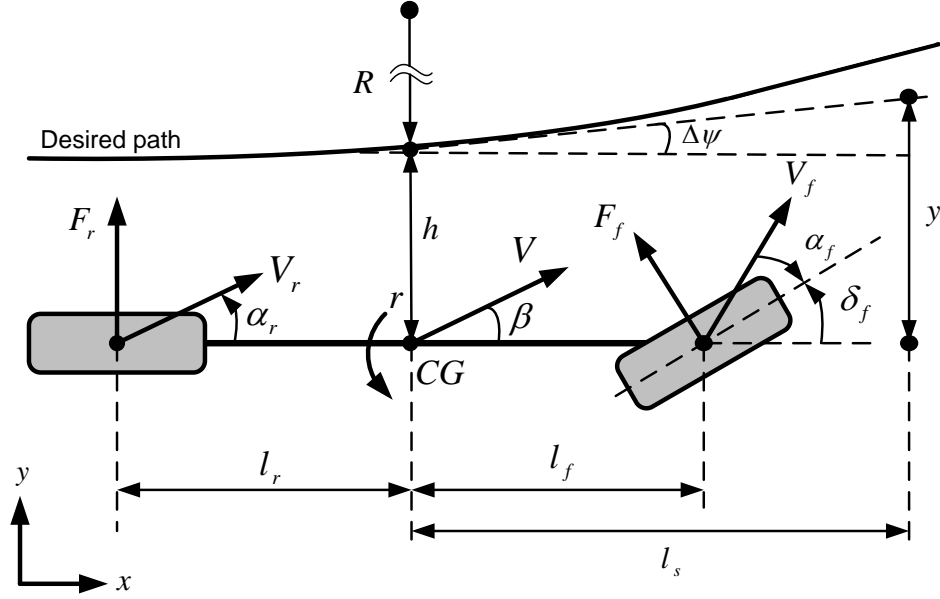


**Figure 4.1** : Vehicle steering model.

The linear vehicle steering model is described in state-space form as

$$\begin{bmatrix} \dot{\beta} \\ \dot{r} \\ \Delta\dot{\psi} \\ \dot{y} \end{bmatrix} = \begin{bmatrix} a_{11} & a_{12} & 0 & 0 \\ a_{21} & a_{22} & 0 & 0 \\ 0 & 1 & 0 & 0 \\ V & l_s & V & 0 \end{bmatrix} \begin{bmatrix} \beta \\ r \\ \Delta\psi \\ y \end{bmatrix} + \begin{bmatrix} b_{11} & 0 \\ b_{21} & 0 \\ 0 & -V \\ 0 & 0 \end{bmatrix} \begin{bmatrix} \delta_f \\ \rho_{ref} \end{bmatrix} \quad (4.1)$$

where  $\beta$ ,  $r$ ,  $V$ ,  $\Delta\psi$ ,  $l_s$  and  $y$  are vehicle side slip angle, vehicle yaw rate, vehicle velocity, yaw angle relative to the desired path's tangent, the preview distance and lateral deviation from the desired path at the preview distance, respectively. The control input is the steering angle  $\delta_f$ .  $\rho_{ref} = 1/R$  is the road curvature where  $R$  is the road radius. The remaining terms are

$$\begin{aligned} a_{11} &= -(c_r + c_f)/\tilde{m}V, & a_{12} &= -1 + (c_r l_r - c_f l_f)/\tilde{m}V^2 \\ a_{21} &= (c_r l_r - c_f l_f)/\tilde{J}, & a_{22} &= -(c_r l_r^2 + c_f l_f^2)/\tilde{J}V^2 \\ b_{11} &= c_f/\tilde{m}V, & b_{12} &= c_f l_f/\tilde{J} \end{aligned} \quad (4.2)$$

where  $\tilde{m} = m/\mu$  is the virtual mass,  $\tilde{J} = J/\mu$  is the virtual moment of inertia,  $\mu$  is the tire-road friction coefficient,  $m$  is the vehicle mass,  $J$  is the moment of inertia,  $c_f$  and  $c_r$  are the cornering stiffnesses,  $l_f$  is the distance from the center of gravity of the vehicle (CG) to the front axle and  $l_r$  is the distance from the CG to the rear axle [39]. The values of the parameters used are  $J = 2392 \text{ kgm}^2$ ,  $l_f = 1.07 \text{ m}$ ,  $l_r = 1.53 \text{ m}$ ,  $l_s = 2 \text{ m}$ ,  $c_f = 72463 \text{ N/rad}$  and  $c_r = 92492 \text{ N/rad}$ . The vehicle mass, the vehicle velocity and the tire-road friction coefficient are taken as uncertain parameters within the ranges of  $m \in [1400, 1700]$  (kg) (the nominal value of mass is 1550 kg),

$\mu \in [0.5, 1], V \in [1, 20]$  (m/s), respectively. The virtual mass, then, is within the range  $\tilde{m} = m/\mu \in [1400, 3400]$  (kg). The corresponding uncertainty box of virtual mass and vehicle speed is illustrated in Figure 4.2.

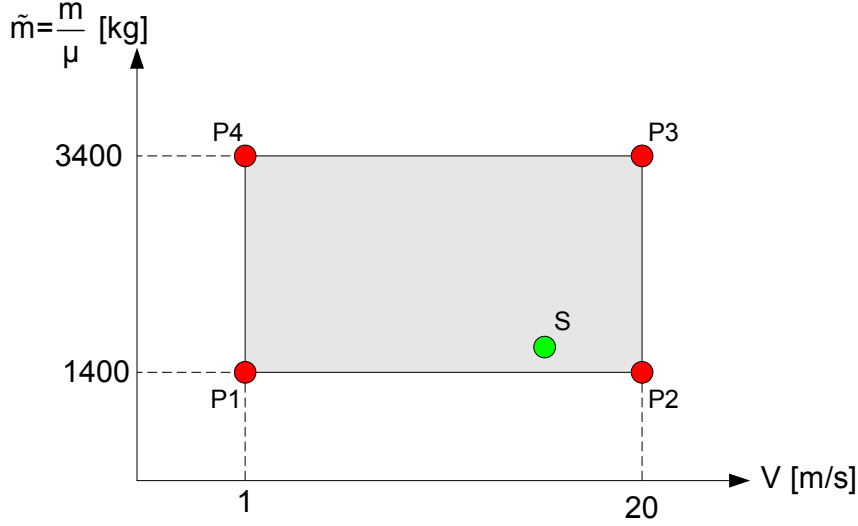


**Figure 4.2 :** Uncertainty box.

#### 4.2.2 Nonlinear vehicle model

The equations of motion for longitudinal and lateral dynamics of the nonlinear vehicle model are

$$m(a_x - rV_y) = \sum_{i=f,r} F_{xi} \cos \delta_i - F_{yi} \sin \delta_i - (F_{aero} + F_{rr} + F_{hc}) \quad (4.3)$$

$$m(a_y + rV_x) = \sum_{i=f,r} F_{xi} \sin \delta_i + F_{yi} \cos \delta_i \quad (4.4)$$

while the equation of motion around the yaw axis is

$$I_z \dot{r} = l_f F_{yf} \cos \delta_f - l_r F_{yr} \cos \delta_r + l_f F_{xf} \sin \delta_f - l_r F_{xr} \sin \delta_r \quad (4.5)$$

where  $F_{xi}$  and  $F_{yi}$  are the longitudinal and the lateral tire forces.  $f$  and  $r$  represent the front and rear tires.  $a_x$ ,  $a_y$ ,  $V_x$ ,  $V_y$  and  $I_z$  are the longitudinal acceleration at the CG, the lateral acceleration at the CG, the longitudinal velocity at the CG, the lateral velocity at the CG and the moment of inertia about the yaw axis, respectively. Note that the front wheel steered vehicle considered in this chapter so that the rear wheel steering angle is taken as zero ( $\delta_r = 0$ ) [55].

The resistive forces which affect the longitudinal dynamics of the vehicle are shown in Figure 4.3. The aerodynamic drag force  $F_{aero}$  is given by

$$F_{aero} = \frac{1}{2}A\rho C_d V^2 \quad (4.6)$$

where  $A$  is the effective frontal area of the vehicle,  $\rho$  is the mass density of air,  $C_d$  is the drag coefficient, and  $V$  is the velocity of the vehicle. The rolling resistance force  $F_{rr}$  is determined as

$$F_{rr} = C_{rr}mg \cos(\theta) \quad (4.7)$$

where  $C_{rr}$  is the rolling resistance coefficient and  $\theta$  is the road inclination angle. The gravitational slope resistance force  $F_{hc}$  is modeled as

$$F_{hc} = mg \cos(\theta). \quad (4.8)$$

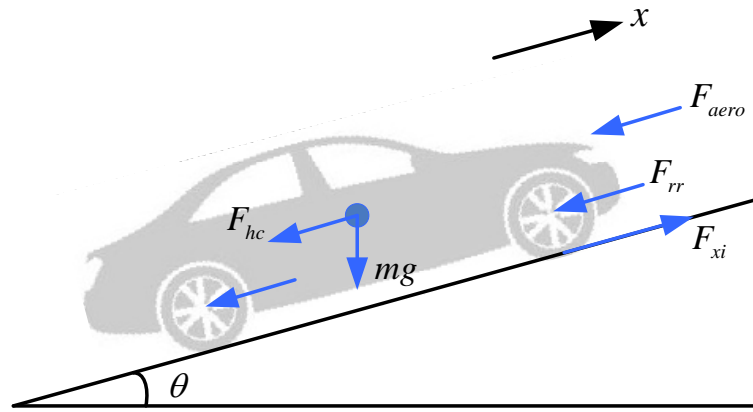


**Figure 4.3 :** The resistive forces acting on the longitudinal dynamics of the vehicle.

The internal combustion engine (ICE) is modeled using a static engine map that defines the relationship between the inputs of throttle position  $\alpha$ , the engine speed  $\omega$  and the output engine torque  $T_{ICE}(\omega, \alpha)$ . The engine torque output is transmitted to the wheels through the driveline as torque  $T_d$  according to

$$T_d = \eta_t i_t T_{ice}(\omega, \alpha) \quad (4.9)$$

where  $\eta_t$  is a static efficiency factor used to model mechanical losses and it is the transmission ratio. These parameters are used to model the transmission of the vehicle.

The forces and torques acting on the wheel are shown in Figure 4.4. The moment balance at the center of the wheel is given by

$$I_w \dot{\omega}_i = T_d - T_{bi} - F_{xi} R_w \quad (4.10)$$

where  $I_w$  is the moment of inertia of the wheel,  $\omega_i$  is the angular velocity of the  $i$ th wheel,  $T_{bi}$  is the braking torque on the  $i$ th wheel applied through the brake system,  $F_{xi}$  is the longitudinal tire force of the  $i$ th wheel and  $R_w$  is the effective wheel radius.

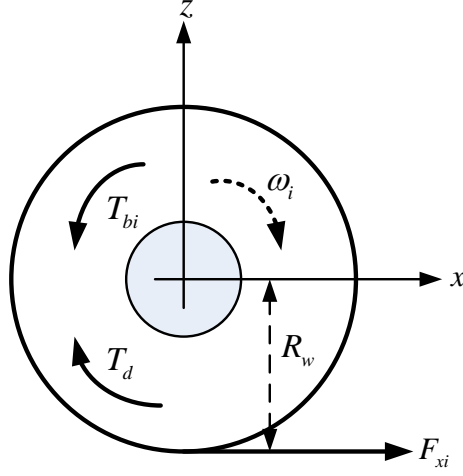


**Figure 4.4 :** The forces and the torques acting on the wheel.

The longitudinal velocities of the front and rear wheels can be determined as follows:

$$V_{fx} = \sqrt{V_x^2 + (V_y + l_f r)^2} \cos \alpha_f \quad (4.11)$$

$$V_{rx} = \sqrt{V_x^2 + (V_y - l_r r)^2} \cos \alpha_r \quad (4.12)$$

where the tire slip angles are

$$\alpha_f = \delta_f - \arctan \left( \tan \beta + \frac{l_f r}{V_x} \right) \quad (4.13)$$

$$\alpha_r = \delta_r - \arctan \left( \tan \beta + \frac{l_r r}{V_x} \right). \quad (4.14)$$

The longitudinal wheel slip ratio is defined as

$$s_i = \begin{cases} \frac{R_w \omega_i - V_{ix}}{V_{ix}}, & R_w \omega_i < V_{ix} \text{ (braking)} \\ \frac{R_w \omega_i - V_{ix}}{R_w \omega_i}, & R_w \omega_i > V_{ix} \text{ (traction), } (i = f, r). \end{cases} \quad (4.15)$$

The Dugoff tire model is used for the calculations of the tire forces as

$$F_{xi} = f_i C_{xi} s_i \quad (4.16)$$

$$F_{yi} = f_i C_{yi} \alpha_i \quad (4.17)$$

where  $C_{xi}$  and  $C_{yi}$  are the longitudinal and the lateral cornering stiffness of the  $i$ th wheel. The coefficients  $f_i$  are determined using

$$f_i = \begin{cases} 1, & F_{Ri} \leq \frac{\mu F_{zi}}{2} \\ \left(2 - \frac{\mu F_{zi}}{2F_{Ri}}\right) \frac{\mu F_{zi}}{2F_{Ri}}, & F_{Ri} > \frac{\mu F_{zi}}{2} \end{cases} \quad (4.18)$$

$$F_{Ri} = \sqrt{(C_{xi}s_i)^2 + (C_{yi}\alpha_i)^2}. \quad (4.19)$$

### 4.2.3 Model validation

Model validation studies were performed using the data obtained from the experimental vehicle test runs. The experimental vehicle is a Fiat Linea mid-sized sedan. Three similar Fiat Linea mid-sized sedans were used by the author and their colleagues in lateral dynamics testing [65], semi-autonomous driving in a platoon [55] and in autonomous path following experiments [66], respectively. Figure 4.5 shows the drive-by-wire vehicle of Istanbul Okan University named Okanom which was used here for the model validation studies. In the vehicle, throttle, brake and steering actuation signals are provided by a dSPACE MicroAutoBox general purpose electronic control unit which is also used for all the low level computations. Available signals on the vehicle CAN bus are read by this MicroAutoBox. A personal computer operating under Linux is used as an upper level control system. This PC collects data from the GPS receiver, the IMU, the LIDAR in front of the vehicle and the IEEE 802.11p vehicle to vehicle (V2V) modem and communicates with the low level MicroAutoBox controller. The GPS and the IMU signals are used in the GPS/INS integration [67].



**Figure 4.5 :** Experimental vehicle.

The measured steering wheel and vehicle velocity were used as inputs to the nonlinear vehicle model. The simulated outputs for vehicle velocity and yaw rate were compared with the obtained experimental data. A comparison result from a test run is shown in Figure 4.6. A J-turn like maneuver is applied to the vehicle. The nonlinear vehicle model results of the vehicle velocity and yaw rate are consistent with the obtained data from the experimental vehicle. In the test run shown in Figure 4.7, the experimental vehicle follows a velocity profile from the Grand Cooperative Driving Challenge [55]. The steering wheel input is zero. It can be seen from Figure 4.7 that the velocity obtained from the nonlinear vehicle model coincides with the experimental test result closely.

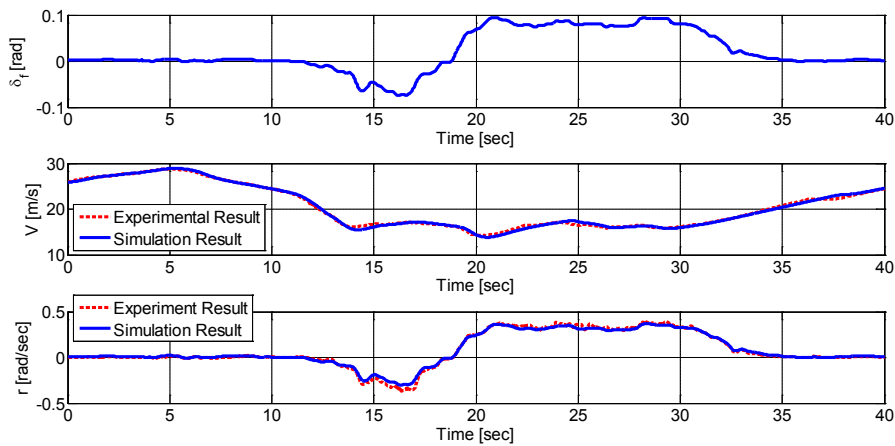


**Figure 4.6 :** Comparison of test data and nonlinear vehicle simulation results for lateral dynamics.

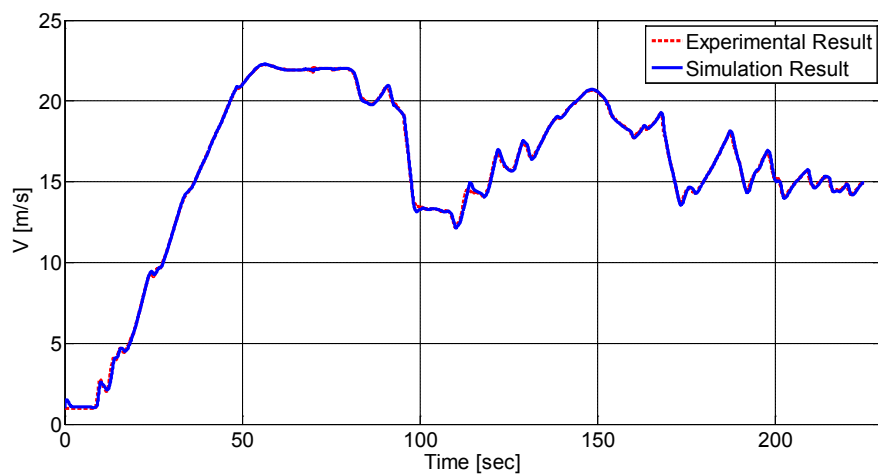


**Figure 4.7 :** Comparison of test data and nonlinear vehicle simulation results for longitudinal dynamics.

### 4.3 Robust PID Steering Controller Design using The Parameter Space Approach

#### 4.3.1 Mapping D-stability requirements into the parameter space

Similar to the approach in [31], D-stability requirements can be mapped into the parameter space.

Consider the plant is given by

$$G(s) = \frac{N(s)}{D(s)} \quad (4.20)$$

where  $N$  represents the numerator of the plant and  $D$  represents the denominator of the plant. The real and imaginary parts of the numerator and denominator can be defined as  $N(j\omega) = N_R(\omega) + jN_I(\omega)$  and  $D(j\omega) = D_R(\omega) + jD_I(\omega)$ .

The PID controlled closed loop system characteristic equation can be written as

$$p_c(s) = sD(s) + (k_p s + k_i + k_i s^2)N(s) = a_{n+1}s^{n+1} + a_n s^n + \dots + a_1 s + a_0 = 0 \quad (4.21)$$

where  $n$  is the degree of the plant  $G(s)$ .

The Hurwitz stability boundary crossed by a pair of complex conjugate roots is characterized by the following equations:

$$Re[p_c(j\omega)] = 0 \text{ and } Im[p_c(j\omega)] = 0, \forall \omega \in (0, \infty] \quad (4.22)$$

This is called as complex root boundary (CRB).

There may be a real root boundary such that a single real root crosses the boundary at frequency  $\omega = 0$  is characterized by

$$p_c(0) = 0 \text{ or } a_0 = 0 \quad (4.23)$$

This is called as real root boundary (RRB).

There may exist an infinite root boundary (IRB) which is characterized by a degree drop in characteristic polynomial at  $\omega = \infty$ . This degree drop in characteristic polynomial is characterized as

$$a_{n+1} = 0 \quad (4.24)$$

CRB, RRB and IRB solutions parameterized by frequency  $\omega$  can be plotted in the parameter plane of two free design parameters to show the Hurwitz stability regions of

the given closed loop system. The free parameter pairs which provide Hurwitz stability can be chosen visually from the stable region of the parameter plane.

The aforementioned parameter space computation method to determine Hurwitz stability regions can be extended to specify relative stability regions such as D-stability. A closed loop system is D-stable when the roots of the closed loop characteristic equation lie in the D-stable region in the complex plane as depicted in Figure 4.8.

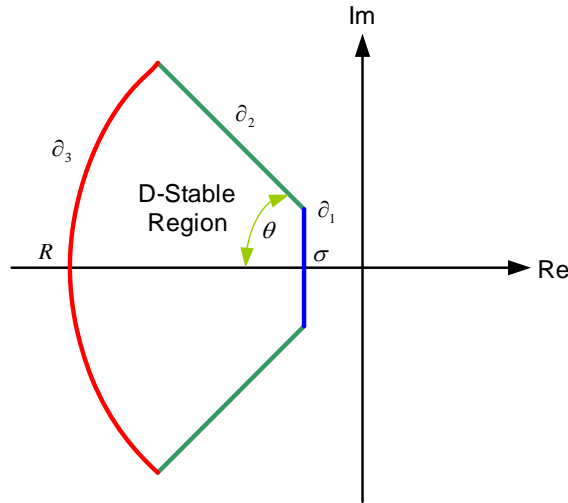


**Figure 4.8 :** D-stable region in the complex plane.

The boundary  $\partial_1$  in Figure 4.8 can be mapped into the parameter space by using  $s - \sigma$  instead of  $s$  in (4.21) in order to shift the stability boundary to  $\partial_1$  in the complex plane. Solving for two free parameters in (4.22) for CRB and (4.23) for RRB, and then plotting results will result in the  $\partial_1$  boundary in the parameter space. For  $\partial_1$  boundary, there is no IRB because  $s$  is never equal to infinity in the D-shaped region. For mapping  $\partial_2$  boundary, use  $re^{j\theta}$  for  $s$  with constant  $\theta$  in (4.21) and parameterize  $r$  in  $re^{j\theta}$  to obtain the CRB of  $\partial_2$ . No RRB and IRB solution exists because  $r$  is never equal to zero or infinity. Lastly,  $\partial_3$  boundary maps into the parameter space by substituting  $s$  with  $Re^{j\theta}$  where  $R$  is constant and the map is parameterized over  $\theta$  in (4.21). This results in CRB for changing  $\theta$  and RRB for  $\theta = 0$ .

### 4.3.2 Application to automatic steering control

The vehicle steering dynamics state space model corresponding to (4.1) can be expressed in standard form as

$$\dot{x} = Ax + Bu. \quad (4.25)$$

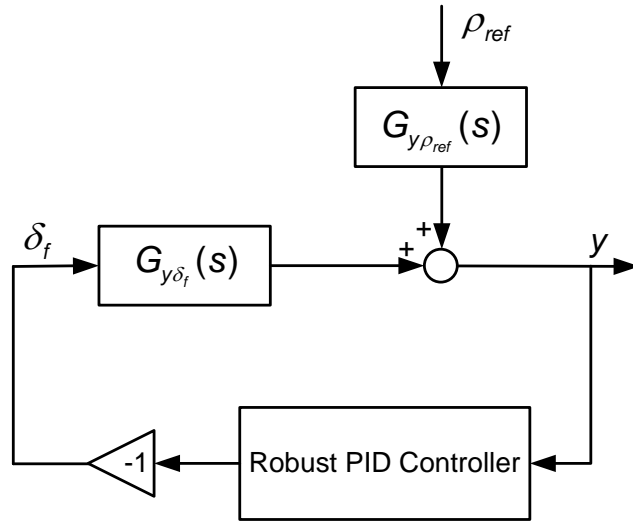
Using the state space form, the transfer function  $G_{y\delta_f}$  from the steering angle  $\delta_f$  to the lateral deviation  $y$  is written as

$$G_{y\delta_f} = [ 0 \ 0 \ 0 \ 1 ] (sI - A)^{-1} \begin{bmatrix} b_{11} \\ b_{21} \\ 0 \\ 0 \end{bmatrix} \quad (4.26)$$

and the transfer function from the road curvature  $\rho_{ref}$  to the lateral deviation  $y$  is described as

$$G_{y\rho_{ref}} = [ 0 \ 0 \ 0 \ 1 ] (sI - A)^{-1} \begin{bmatrix} 0 \\ 0 \\ -V \\ 0 \end{bmatrix}. \quad (4.27)$$

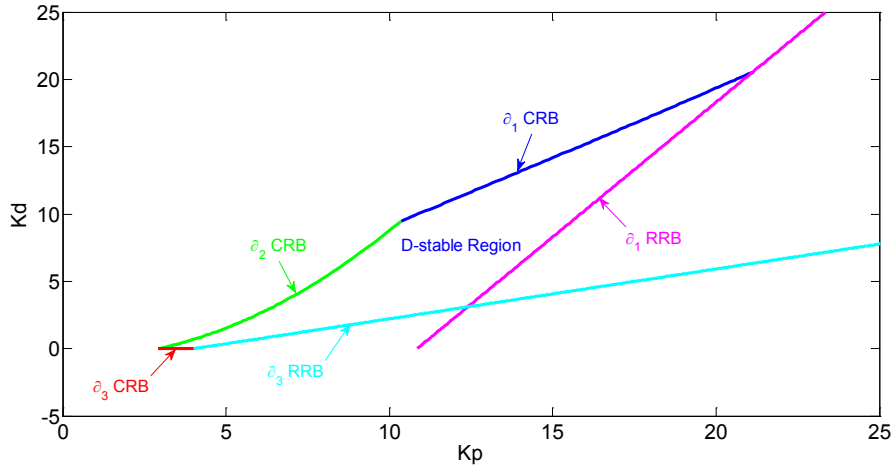
These transfer functions are used in designing the robust PID controller for the automatic steering system. The control system structure is illustrated in Figure 4.9.



**Figure 4.9 :** Control system structure.

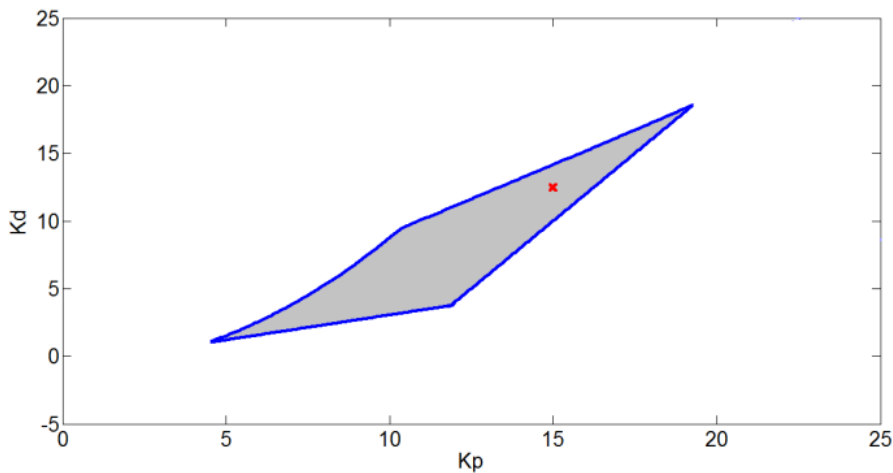
The robust PID controller is designed based on the parameter space approach. The D-stability requirements are taken into consideration. The D-stability boundaries (shown in Figure 4.8) are formed by assuming roots no closer than 0.5 to the imaginary axis and no further in magnitude than 2.7 from the imaginary axis ( $\sigma = 0.5$  and  $R = 2.7$ ). A minimum damping ratio corresponding to  $\theta = 45^\circ$  is determined as 0.707. Two parameters of the PID controller are selected as free design parameters. In this chapter, these free parameters are chosen as the proportional gain  $k_p$  and the derivative gain  $k_d$  of the PID controller. The integral gain  $k_i$  of the PID controller is determined as a fixed parameter by the designer. Here,  $k_i$  is selected as 5.

Figure 4.10 shows the solution region for the P1 vertex of the uncertainty box shown in Figure 4.2.  $\partial_1$  CRB and RRB,  $\partial_2$  CRB and  $\partial_3$  CRB and RRB of the D-stability bounds are depicted with different colors. The intersection of these bounds determines the boundary of the D-stable region in the  $k_p - k_d$  plane.



**Figure 4.10 :** Detailed view of D-stability in parameter space for P1.

The overall solution region which combines all the solutions for the vertices of the uncertainty box in Figure 4.2 is shown in Figure 4.11. The design point for  $k_p$  and  $k_d$  is selected as (15, 12.5) from the shaded area in Figure 4.11 which satisfies the design requirements for all operating points.



**Figure 4.11 :** Overall D-stability solution region.

#### 4.4 Simulation Studies

The simulation studies are performed to test the effectiveness of the designed robust PID controller. In the first simulation, the vehicle mass, the vehicle velocity and the

tire-road friction coefficient are taken as  $1500 \text{ kg}$ ,  $15 \text{ m/s}$  and  $1$ , respectively. These parameter values correspond to a single point S in the uncertainty box of Figure 4.2.

In the first simulation of Figure 4.12, the vehicle tries to follow a path consisting of a straight track of  $150 \text{ m}$  followed by a full turn in a circle of radius  $100 \text{ m}$  followed by a  $150 \text{ m}$  straight track. The vehicle velocity is  $15 \text{ m/s}$  along the way. In the nonlinear vehicle model, a PI based cruise control algorithm keeps the vehicle velocity constant. Also, the steering angle saturation is taken into consideration in the simulations. The front wheel steering angle  $\delta_f$  is limited to  $40$  degrees. The simulation results given in Figure 4.12 show the vehicle trajectory, the lateral deviation, the vehicle velocity and the yaw rate. It is seen that the vehicle follows the desired trajectory successfully. The vehicle velocity is kept around  $15 \text{ m/s}$  by the cruise control algorithm and the vehicle yaw rate is at acceptable values.

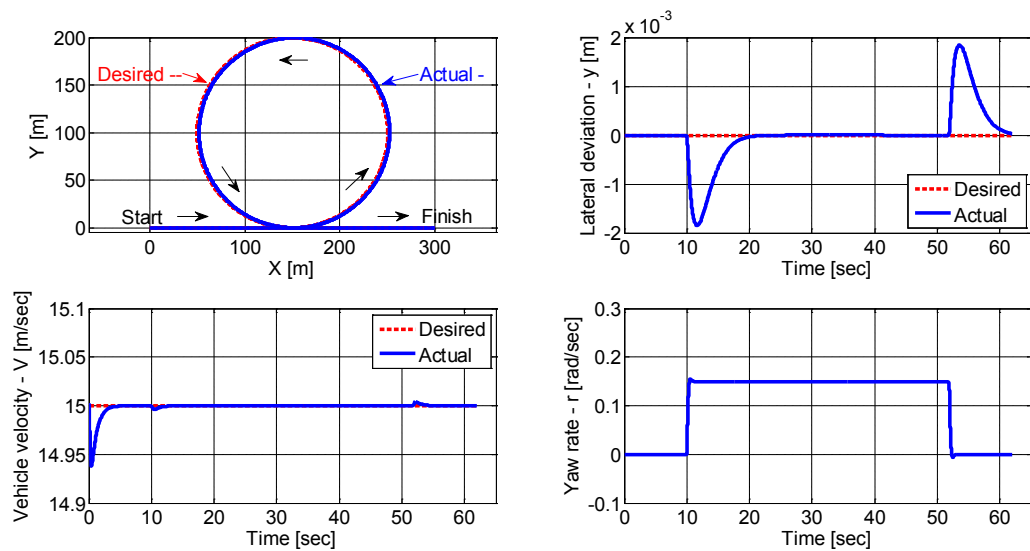


**Figure 4.12 :** Simulation results 1.

In the second simulation, the vehicle tries to follow a curving path with different road curvature values. The tire- road friction coefficient alters between  $0.5$  and  $1$  to simulate different road conditions such as dry asphalt, slippery surface. The vehicle tries to track a velocity profile which changes between  $5$  and  $18 \text{ m/s}$ . The followed road curvature, the variable tire-road friction coefficient profile, the vehicle trajectory, the lateral deviation of the vehicle, the velocity profile followed, the vehicle velocity and also the vehicle yaw rate change can be seen from the Figure 4.13. It is seen that the vehicle follows the given trajectory with very small lateral deviation and the velocity

profile is followed successfully by the PI-based cruise controller. Note that the vehicle yaw rate is at acceptable values.

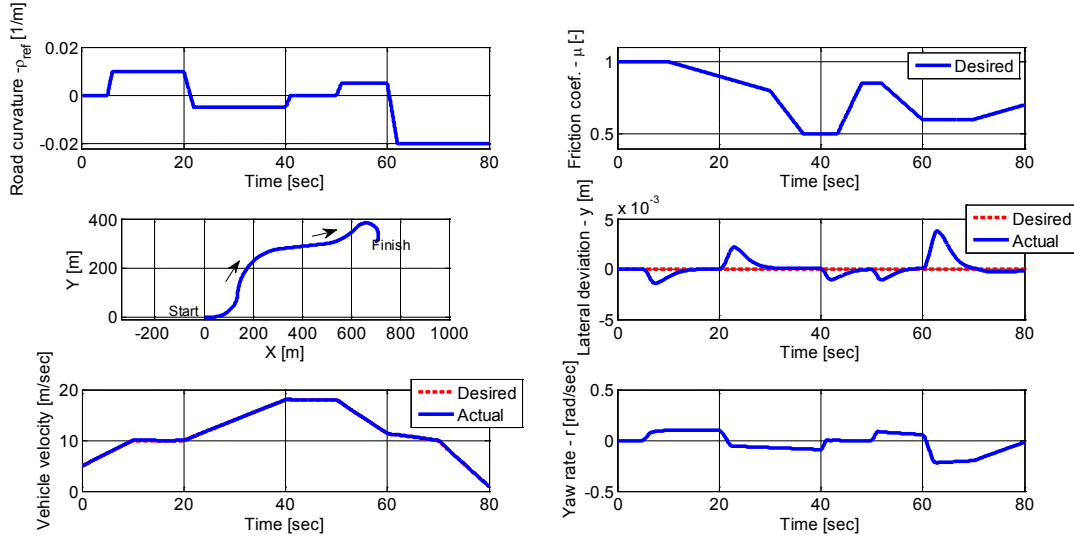


Figure 4.13 : Simulation results 2.

#### 4.5 Digital Map and GPS Measurements based Robust PID Steering Control

Robust steering control can be realized based on offline generated digital maps and real time global positioning system (GPS) measurements in real implementation. In this section, the details of the digital map generation and GPS measurements based steering control are given. It can be seen from the steering control system structure shown in Figure 4.9 that the lateral deviation from the desired path at the preview distance is feedback for performing steering control. Considering Figure 4.1, the lateral deviation from the desired path at the preview distance can be calculated as follows:

$$y = h + l_s \sin(\Delta\psi) \quad (4.28)$$

where  $h$  is the lateral deviation from the desired path at the centre of gravity of the vehicle,  $l_s$  is the preview distance and  $\Delta\psi$  is the yaw angle relative to the desired path's tangent. Also, it can be called as the yaw angle error.  $h$  and  $\Delta\psi$  can be calculated using offline generated digital maps and online GPS measurements which determines the vehicle position according to the global coordinates.

Robust PID steering control system based on digital map and GPS measurements is depicted in Figure 4.14. Also the PI based cruise control system used for speed control

of the vehicle is shown on the same figure. In simulations at this section, this structure (see Figure 4.14) is used. It is different from the structure given in Figure 4.9.

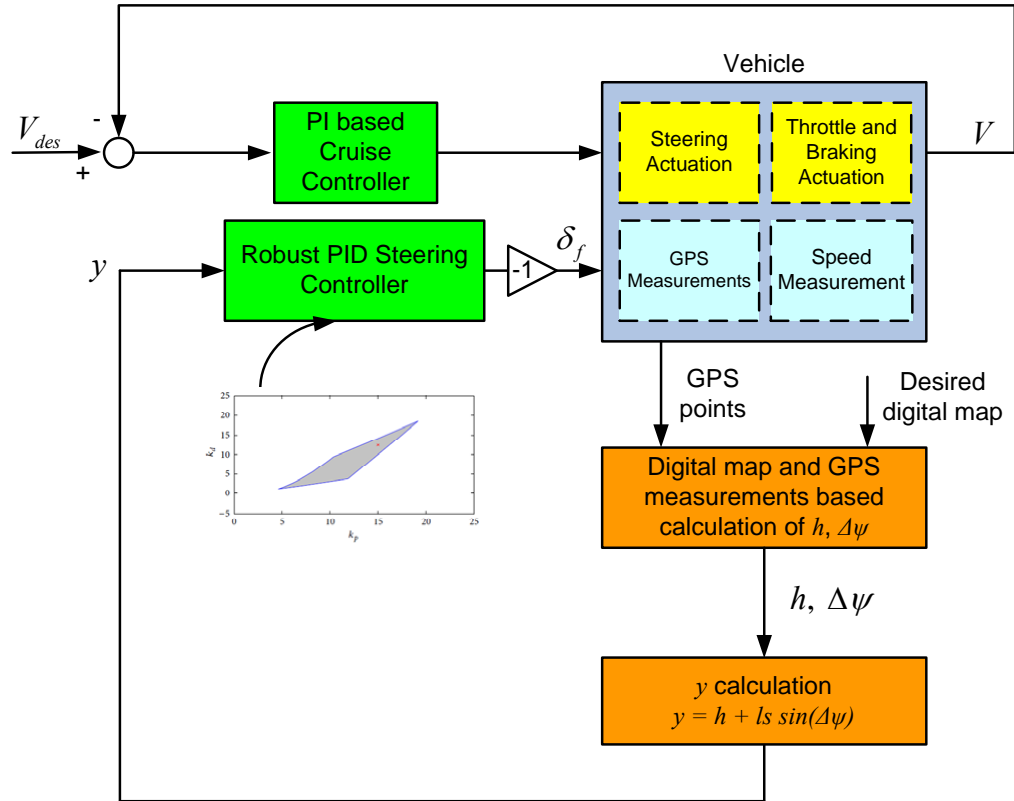


**Figure 4.14 :** Steering control system structure based on digital map and GPS measurements.

In this thesis, a similar approach given in [12, 59, 68, 69] used for the calculations of  $h$  and  $\Delta\psi$ . In the following sections, high resolution digital map generation and lateral deviation and yaw angle error calculations are given in details and the effectiveness of the approach is tested with the simulations.

#### 4.5.1 High resolution digital map generation

Robust PID steering control system requires the knowledge of lateral deviation and yaw angle error of the vehicle to calculate the lateral deviation from the desired path at the preview distance given in (4.28). Using a digital map, the vehicle's current position is utilized to determine the lateral deviation and the yaw angle of the vehicle.

High resolution digital maps can be generated using the GPS data points which are obtained from a constant speed test. The map making approach introduced in [12] is used here to obtain high resolution digital maps. These maps consist of a predetermined number of segments. Each of these segments is a parametric polynomial

of a distance parameter,  $\lambda$ . For simplicity the aforementioned segments can be chosen to contain equal numbers of data points.

The third order polynomials of the each segment can be written as follows:

$$X_i(\lambda) = a_{xi}\lambda^3 + b_{xi}\lambda^2 + c_{xi}\lambda + d_{xi} \quad (4.29)$$

$$Y_i(\lambda) = a_{yi}\lambda^3 + b_{yi}\lambda^2 + c_{yi}\lambda + d_{yi} \quad (4.30)$$

where  $\lambda$  changes from 0 to 1 on each segment.  $a_{xi}$ ,  $b_{xi}$ ,  $c_{xi}$ ,  $d_{xi}$  and  $a_{yi}$ ,  $b_{yi}$ ,  $c_{yi}$ ,  $d_{yi}$  are the coefficients of the  $i$ th segment  $X$  and  $Y$  polynomials, respectively.

In the digital map processing, the determination of the polynomial coefficients is a constrained linear squares problem. Before solving this problem, the unconstrained least square problem should be solved. The unconstrained least square problem for digital map generation can be defined as follows:

$$x_{data} = \Lambda n_{x,uncs} \quad (4.31)$$

$$y_{data} = \Lambda n_{y,uncs} \quad (4.32)$$

where

$$\Lambda = \begin{bmatrix} \bar{\lambda}^3 & \bar{\lambda}^2 & \bar{\lambda} & 1 & 0 & 0 & 0 & 0 \dots \\ 0 & 0 & 0 & 0 & \bar{\lambda}^3 & \bar{\lambda}^2 & \bar{\lambda} & 1 \dots \\ \vdots & \vdots & \vdots & \vdots & \vdots & \vdots & \vdots & \ddots \end{bmatrix} \quad (4.33)$$

$$n_{x,uncs} = [ a_{x1} \quad b_{x1} \quad c_{x1} \quad d_{x1} \quad \dots \quad a_{xm} \quad b_{xm} \quad c_{xm} \quad d_{xm} ]^T \quad (4.34)$$

$$n_{y,uncs} = [ a_{y1} \quad b_{y1} \quad c_{y1} \quad d_{y1} \quad \dots \quad a_{ym} \quad b_{ym} \quad c_{ym} \quad d_{ym} ]^T \quad (4.35)$$

Here  $\bar{\lambda}$  shows the entire  $\lambda$  array ranging from 0 to 1. Its length equal to the number of data points in the segment.  $n_{x,uncs}$  and  $n_{y,uncs}$  contain the best fitted polynomial coefficients for all  $m$  segments.

The solution of the unconstrained least square problem can be given as follows:

$$n_{x,uncs} = (\Lambda^T \Lambda)^{-1} \Lambda^T x_{data} \quad (4.36)$$

$$n_{y,uncs} = (\Lambda^T \Lambda)^{-1} \Lambda^T y_{data} \quad (4.37)$$

The unconstrained least square problem solution does not guarantee the continuity and smoothness at the segment boundaries. To avoid these problems, the below boundary conditions are added to the unconstrained least square problem solution.

$$X_i(1) = X_{i+1}(0) \quad (4.38)$$

$$Y_i(1) = Y_{i+1}(0) \quad (4.39)$$

$$\frac{dX_i(1)}{d\lambda} = \frac{dX_{i+1}(0)}{d\lambda} \quad (4.40)$$

$$\frac{dY_i(1)}{d\lambda} = \frac{dY_{i+1}(0)}{d\lambda} \quad (4.41)$$

The aforementioned conditions can be written as constraint equations considering the segment polynomials defined in (4.29) and (4.30):

$$a_{xi} + b_{xi} + c_{xi} + d_{xi} = d_{xi+1} \quad (4.42)$$

$$a_{yi} + b_{yi} + c_{yi} + d_{yi} = d_{yi+1} \quad (4.43)$$

$$3a_{xi} + 2b_{xi} + c_{xi} = c_{xi+1} \quad (4.44)$$

$$3a_{yi} + 2b_{yi} + c_{yi} = c_{yi+1} \quad (4.45)$$

Using these constraint equations, the unconstrained least square problem can be reformulated as a constrained least square problem. The constraint equations are placed on the problem in the form of a matrix equation:

$$Fn_{x,cs} = 0 \quad (4.46)$$

$$Fn_{y,cs} = 0 \quad (4.47)$$

where  $F$  matrix is formed to constraint the continuity and smoothness at segment boundaries. The last rows of the  $F$  matrix must provide the continuity and smoothness between the final and the first segments of the map in order to obtain a closed map. As an example for four segments digital map (considering each segment is defined using third order polynomials as shown in (4.29) and (4.30), the  $F$  matrix can be written as follows to form closed digital map:

$$F = \begin{bmatrix} 1 & 1 & 1 & 1 & 0 & 0 & 0 & 0 & -1 & 0 & 0 & 0 & 0 & 0 & 0 \\ 3 & 2 & 1 & 0 & 0 & 0 & -1 & 0 & 0 & 0 & 0 & 0 & 0 & 0 & 0 \\ 0 & 0 & 0 & 0 & 1 & 1 & 1 & 1 & 0 & 0 & 0 & -1 & 0 & 0 & 0 \\ 0 & 0 & 0 & 0 & 3 & 2 & 1 & 0 & 0 & 0 & -1 & 0 & 0 & 0 & 0 \\ 0 & 0 & 0 & 0 & 0 & 0 & 0 & 0 & 1 & 1 & 1 & 1 & 0 & 0 & 0 \\ 0 & 0 & 0 & 0 & 0 & 0 & 0 & 0 & 3 & 2 & 1 & 0 & 0 & 0 & -1 \\ 0 & 0 & 0 & -1 & 0 & 0 & 0 & 0 & 0 & 0 & 0 & 0 & 1 & 1 & 1 \\ 0 & 0 & -1 & 0 & 0 & 0 & 0 & 0 & 0 & 0 & 0 & 0 & 3 & 2 & 1 \end{bmatrix} \quad (4.48)$$

Finally, the constrained least square problem solution for digital map generation can be obtained as follows:

$$n_{x,cs} = n_{x,uncs} - (\Lambda^T \Lambda)^{-1} F^T [F (\Lambda^T \Lambda)^{-1} F^T]^{-1} F n_{x,uncs} \quad (4.49)$$

$$n_{y,cs} = n_{y,uncs} - (\Lambda^T \Lambda)^{-1} F^T \left[ F (\Lambda^T \Lambda)^{-1} F^T \right]^{-1} F n_{y,uncs} \quad (4.50)$$

Figure 4.15 shows a digital map generated from data points. It contains eight segments. Each segment has equal number of data points. It can be seen from Figure 4.15 that the boundaries of segments are continuous and smooth.

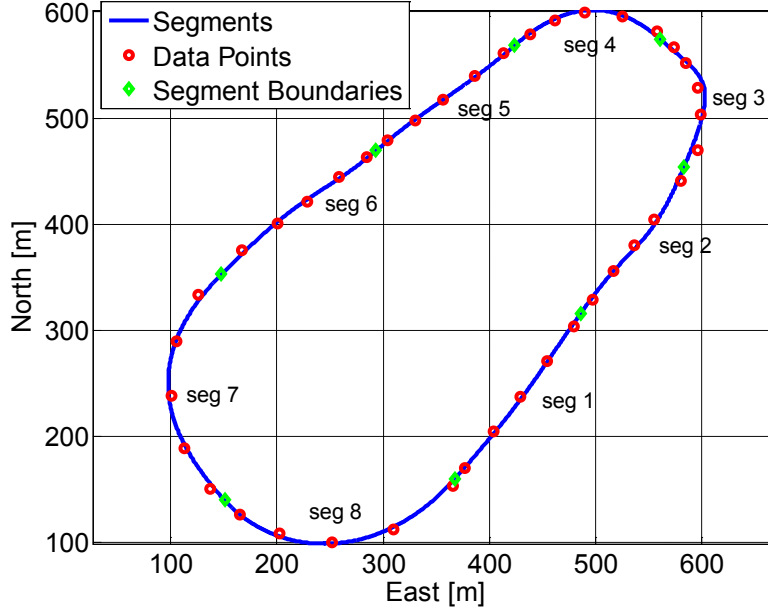


**Figure 4.15 :** A generated digital map using the constrained least square solution.

#### 4.5.2 Lateral deviation and yaw angle error calculations

The desired trajectory for the robust steering control can be described by the generated digital map. The lateral deviation and yaw angle error of the vehicle for each segment can be found by comparing the desired trajectory (the generated map) and the vehicle position in real time.

Assuming that the radius of the curvature for each segment is large compared to the lateral deviation of the vehicle, the shortest distance from the vehicle to the path is perpendicular with the path tangent. Using vectorial relation shown in Figure 4.16, the dot product between the vehicle's position relative to the path and the slope of the map should be zero to obtain the shortest distance. This dot product can be written as follows:

$$((X(\lambda) - P_E), (Y(\lambda) - P_N)) (\dot{X}(\lambda), \dot{Y}(\lambda)) = 0 \quad (4.51)$$

where  $P_E$  and  $P_N$  denote the vehicle's east and north position according to the map coordinate system, respectively.

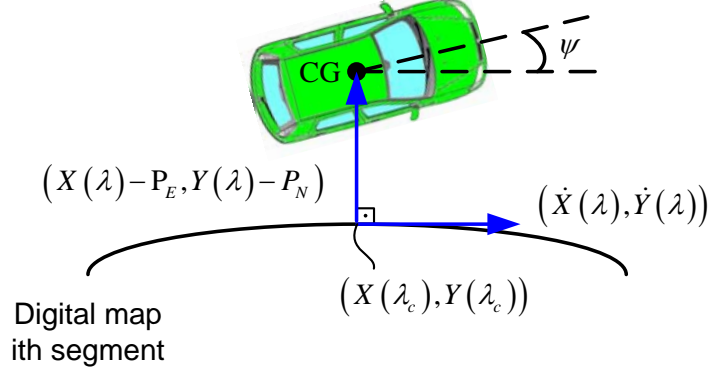


**Figure 4.16 :** Lateral deviation and yaw angle error calculations.

If the polynomial used to define the map segment is  $n$ th order, this dot product polynomial is the order of  $2n - 1$ . The dot product given in (4.51) is solved for the distance down the segment,  $\lambda_c$ , which corresponds to the point on the segment closest to the vehicle. Note that the problem given in (4.51) can be solved for  $\lambda_c$  by a polynomial root-finding algorithm such as Matlab's `fzero` algorithm.

Once  $\lambda_c$  is found, it is used to find the distance (the lateral deviation of the vehicle,  $h$ ) between vehicle's CG and the point on the path identified by  $\lambda_c$ . The lateral deviation of the vehicle,  $h$  can be calculated as follows:

$$h = \rho \sqrt{(X(\lambda_c) - P_E)^2 + (Y(\lambda_c) - P_N)^2} \quad (4.52)$$

where  $\rho = \text{sgn}(\vec{U}(3))$  and

$$\vec{U} = ((X(\lambda_c) - P_E), (Y(\lambda_c) - P_N), 0) \times (\dot{X}(\lambda_c), \dot{Y}(\lambda_c), 0).$$

The  $\rho$  part of (4.52) is used to determine sign of the lateral deviation of  $h$ . It is calculated based on the cross product of the vectors between the vehicle's position relative to the path and the slope of the map. The third dimension of this product gives the direction information of the lateral deviation,  $h$ . If  $h$  is positive, it means the vehicle is outer of a closed map and if  $h$  is negative, the vehicle is inner of a closed map.

Similarly, the yaw angle of the vehicle can be calculated comparing the yaw angle of the vehicle and the slope of the path at the point  $\lambda_c$ .

$$\Delta\psi = \psi - \frac{\dot{Y}(\lambda_c)}{\dot{X}(\lambda_c)} \quad (4.53)$$

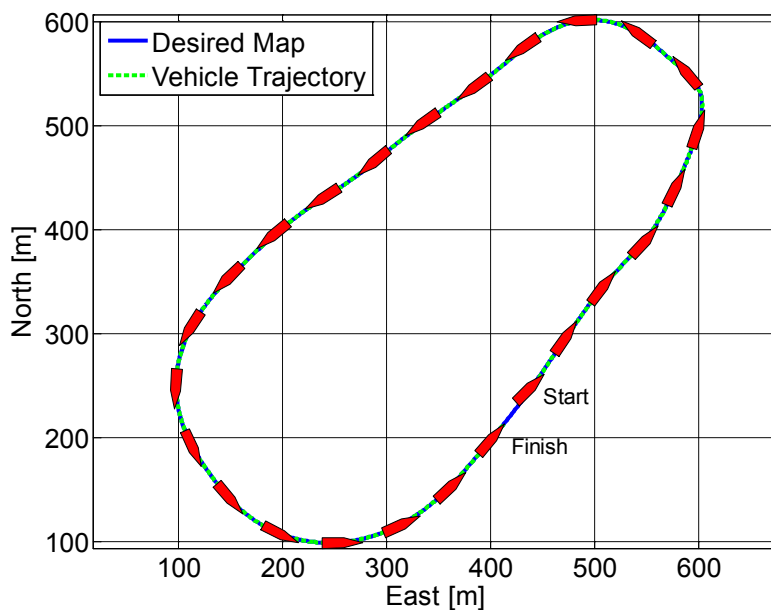
As a result, using the  $h$  and  $\Delta\psi$ , the lateral deviation  $y$  at the preview distance  $l_s$  is calculated by (4.28) and this signal is feedback to the controller to maintain robust steering control as shown in Figure 4.14.

The segment switching is also a problem to be solved in this approach. In order to determine when the vehicle switches the segment, an added algorithm checks the distance between the vehicle and the upcoming segment's boundary, if the distance is lower than a predefined distance (for example 1 *m*), it is assumed that the vehicle switched the segment. Also, it is assumed that the vehicle is always moving forward to maintain consistency.

### 4.5.3 Simulation results

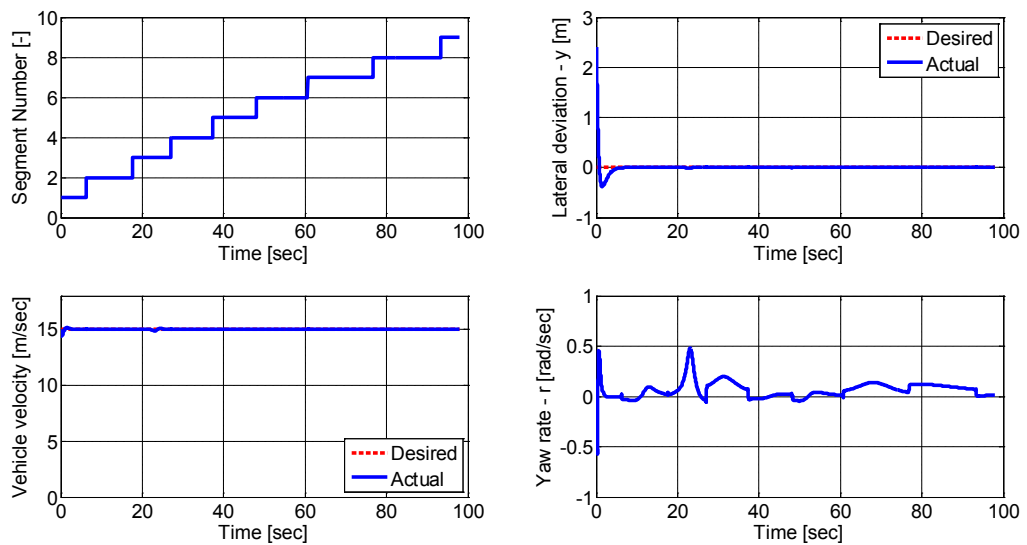
The simulation study is performed to test the digital map and GPS measurements based robust PID steering controller for highly automated driving. In the simulation, the vehicle mass and the tire-road friction coefficient are taken as 1500 *kg* and 1, respectively. The vehicle tries to follow the eight segments desired map with the constant velocity of 15 *m/s*. The lateral deviation (*h*) and the yaw angle error ( $\Delta\psi$ ) are calculated following the procedure given in sub-section 4.5.2. After the determination of *h* and  $\Delta\psi$ , the lateral deviation *y* at the preview distance  $l_s$  is calculated using these variables. Then, *y* is used in the feedback controller as shown in Figure 4.14.

Figure 4.17 shows the desired map and the stroboscopic vehicle trajectory. The vehicle starts its movement from the point (430 *m*, 240 *m*) near the segment 1 with 45 degrees initial yaw angle. Firstly the vehicle moves to compensate the distance difference from the segment 1 and then tracks the segment 1 and the upcoming segments successfully.



**Figure 4.17** : Simulation results: desired map and stroboscopic vehicle trajectory.

Figure 4.18 shows the changes of the segments, the lateral deviation  $y$  from the desired path at the preview distance, vehicle velocity  $V$  and the vehicle yaw rate  $r$  in the simulation. The vehicle tracks the segments from one to eight. It is seen that the lateral deviation at the preview distance is around zero after the settling of the vehicle to the segment 1. The velocity of the vehicle is kept constant at  $15\text{ m/s}$  along the path successfully by the PI-based cruise controller. Also, the vehicle yaw rate is at acceptable values during the simulation.



**Figure 4.18 :** Simulation results: the changes of important variables.

## 4.6 Conclusion

A parameter space based robust PID steering controller design for automated steering was developed and tested in a simulation environment in this chapter. The vehicle mass, the vehicle velocity and the tire-road friction coefficient were taken as uncertain parameters in parameter space design. A validated nonlinear model of a mid-sized sedan was used in the simulations. In the simulations, the vehicle with uncertain parameters followed the different road curvatures with constant and the time varying tire-road friction coefficients successfully.

Also, robust PID steering control was performed based on the digital map and GPS measurements in this chapter. In this control structure, the lateral deviation and the yaw angle error of the vehicle were calculated differently from the previous one by comparing the desired trajectory and the vehicle position in real time. The desired

trajectory (the digital map) was calculated using the constrained least square method. An eight segments high resolution digital map was tracked by the validated nonlinear vehicle model successfully. In general, the simulation results showed the success of the proposed controller in path following.

## **5. LATERAL STABILITY CONTROL OF FULLY ELECTRIC VEHICLES**

### **5.1 Introduction**

Unexpected yaw disturbances caused by unsymmetrical vehicle perturbations like extreme maneuvers on severe road conditions, side wind forces, unilateral loss of tire pressure may result in dangerous lateral motions of a vehicle. Safe driving requires the driver to react extremely quickly in such dangerous situations. This is not possible as the driver who can be modelled as a high-gain control system with dead time overreacts, resulting in instability. Consequently, improvement of vehicle lateral dynamics by active vehicle control to avoid such catastrophic situations has been and is continuing to be a subject of active research [7, 70, 71]. In order to improve the vehicle lateral stability, yaw stability control systems have been developed and commercialized for vehicles with internal combustion engines since the middle of the 90's (see [72, 73] for example).

Different approaches applied to vehicle lateral stability control problem such as differential braking to generate required stabilizing yaw moment [74], active front steering via electric power assisted steering or steer-by-wire [29, 75] and active rear differential systems [76]. Disturbance observer based active front steering control system to yaw stabilization is introduced in [30]. On the other hand, hybrid electric and fully electric vehicles are becoming more popular as fossil fuel resources are declining and environmental issues are becoming more demanding. As a result, automotive producers are seeking vehicles powered by alternative energy sources. Consequently, fully electric vehicles are entering the commercial market in growing numbers and are currently viewed as the future of automobile technology as they do not directly pollute the environment. In addition, lateral stability control systems have become mandatory in most countries for new vehicles. They have to be adapted to fully electric vehicles that use an electric motor instead of an internal combustion engine for traction. This chapter of the thesis addresses lateral stability control of fully electric vehicles.

In the literature, most of the studies on electric vehicle stability control systems are on four wheel drive (4WD) vehicles using in-wheel motors at the wheels [6, 77]. Four wheel driven systems can provide vehicle stability by using the braking and acceleration abilities of independent in-wheel electric motors on each wheel [78]. In contrast to in-wheel motor 4WD electric vehicles, a front wheel driven single motor electric vehicle is taken into consideration in this thesis. The aim of this chapter is to introduce two different lateral stability control systems for improving the lateral stability of a front wheel driven single motor electric vehicle under critical driving conditions. The purpose of the proposed lateral stability control systems is to follow the desired side slip angle and yaw rate values successfully, thereby improving the vehicle's lateral stability.

The organization of this chapter is as follows. In Section 5.2, the proposed ILSC system structure is explained briefly. Then, the subsystems of the ILSC system are explained in the subsections of Section 5.2 as: desired value generation, corrective yaw moment calculation based on scheduled LQR control, braking torque distribution algorithm, electric motor torque reduction algorithm and wheel slip control. In Section 5.3, the proposed RB-LSC system is explained. Also, two different design methods for the RB-LSC systems are given in the subsections of Section 5.3. In Section 5.4, different simulation results are given to verify the effectiveness of the proposed control systems with extreme maneuvers on severe road conditions. Moreover, different lateral control approaches are compared with each other and with a benchmark controller in this section. Finally, this chapter ends with conclusions in Section 5.5.

## **5.2 ILSC System Structure**

The proposed ILSC system consists of subsystems such as corrective yaw moment calculation, braking torque distribution algorithm, wheel slip control and torque reduction algorithm. The corrective yaw moment calculation is based on a scheduled LQR controller. The corrective yaw moment actuation is achieved through individual wheel braking. The braking torque distribution algorithm and wheel slip controls are also used at the lower control level. The wheel slip controller is a bang-bang controller where the desired slip ratios are determined based on a scheduled LQR controller. In addition to the individual braking intervention, electric motor torque reduction is

applied when the individual braking is not enough to provide lateral stability of the vehicle.

Figure 5.1 shows the control structure of the proposed ILSC system. The inputs of the vehicle are front wheel steering angle ( $\delta_f$ ), the tire braking pressures ( $P_{bi}$ ) and the torque reduction command. The outputs of the vehicle are the vehicle side slip angle ( $\beta$ ), the vehicle yaw rate ( $r$ ), the vehicle velocity ( $V$ ) and individual wheel angular velocities ( $\omega_i$ ). The lateral stability control algorithm needs measurement or estimation of several vehicle variables. For example, yaw rate and wheel angular velocities are easily measured using standard sensors. In contrast, vehicle side slip angle, tire-road friction coefficient and vehicle velocity should be estimated since the measurement of these variables is not economically feasible for commercial road vehicles. Several studies on the estimation of the aforementioned vehicle parameters is available in the literature [79–82].

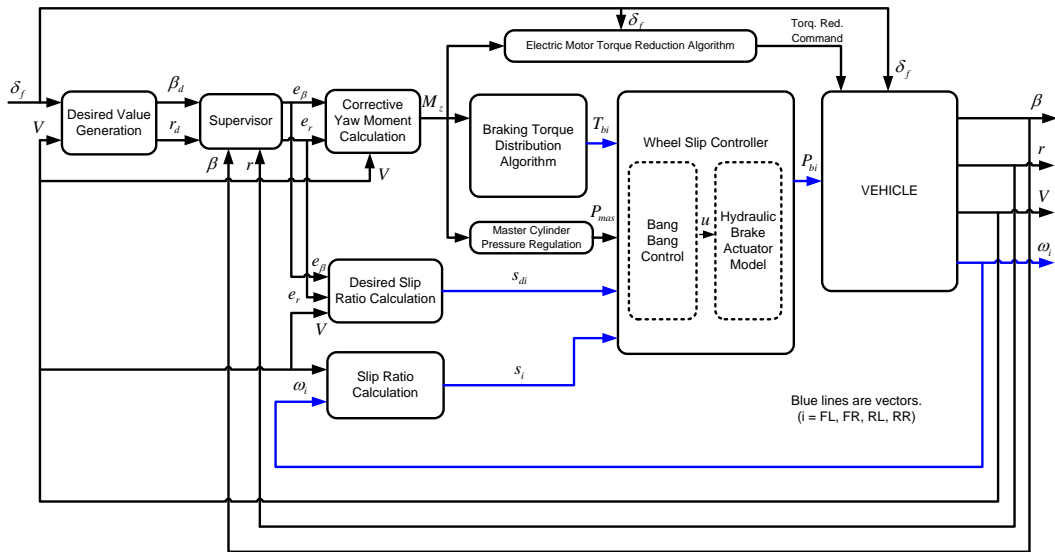


**Figure 5.1 :** The ILSC system structure.

The proposed control system structure is shown in Figure 5.1. In the desired value generation subsystem, the desired values of the vehicle yaw rate and side slip angle are calculated based on current values of steering angle and vehicle velocity. The error values of side slip angle and yaw rate ( $e_\beta$  and  $e_r$ , respectively) are determined by the help of the supervisor. The supervisor contains threshold value triggers to prevent the working of the ILSC system when the error of side slip angle and yaw rate are small. Using the error values of side slip angle and yaw rate, the corrective yaw moment is calculated and this corrective yaw moment acts on the vehicle through the

braking torque distribution algorithm. The individual wheel slip controllers are used for individual wheel braking. In addition to the individual wheel braking intervention, electric motor torque reduction is applied when the individual braking is not enough to provide lateral stability of the vehicle.

The details of these actuators and the subsystems are explained in the following sections.

### 5.2.1 Desired value generation

The desired vehicle yaw rate can be dynamically determined based on front wheel steering angle, vehicle longitudinal velocity and vehicle parameters as follows [83] :

$$r_d = \frac{V_x \delta_f}{\frac{mV_x^2(l_r C_{yr} - l_f C_{yf})}{2C_{yf} C_{yr}(l_f + l_r)} + (l_f + l_r)} \quad (5.1)$$

where  $V_x$  is the vehicle longitudinal velocity at the CG,  $\delta_f$  is the front wheel steering angle,  $m$  is the total mass of the vehicle (1652 kg),  $l_f$  is the distance from vehicle CG to the front axle (1.245 m),  $l_r$  is the distance from vehicle CG to the rear axle (1.510 m),  $C_{yf}$  is the lateral cornering stiffness for the front wheel (52000 N/rad) and  $C_{yr}$  is the lateral cornering stiffness for the rear wheel (52000 N/rad).

The aforementioned equation gives suitable desired yaw rate values when the tire-road friction coefficient is high enough. But in the case of a low friction road surface, the maximum obtained tire force is not sufficiently high to generate the required lateral tire forces to obtain the desired yaw rate. Hence, the desired yaw rate must be limited. Since the lateral acceleration of the vehicle cannot exceed the level allowed by the maximum tire-road friction coefficient, the desired yaw rate is limited by the following relation [73, 83]:

$$|r_d| \leq |0.85\mu g/V_x| \quad (5.2)$$

where  $\mu$  is the tire-road friction coefficient and  $g$  is the gravitational acceleration.

The desired vehicle side slip value is taken as zero ( $\beta_d = 0$ ). Theoretically, we would like to have zero side slip angle. This means that the vehicle longitudinal axis is always aligned with the velocity vector at the center of gravity of the vehicle. However, road vehicles are physically nonholonomic systems and turning cannot be realized without any side slippage. The practical aim is to keep the side slip at low values.

### 5.2.2 Corrective yaw moment calculation based on scheduled LQR control

The corrective yaw moment calculation is realized based on the single track vehicle model and LQR optimal control design. The single track model is the simplest vehicle model that accurately captures lateral dynamics up to 0.3-0.4g of lateral acceleration and has been validated in many publications (e.g. [9]).

In the single track model, two tires on the same axle are lumped together and this results in one front and one rear tire sets. Figure 5.2 illustrates the basic parameters of the single track model.

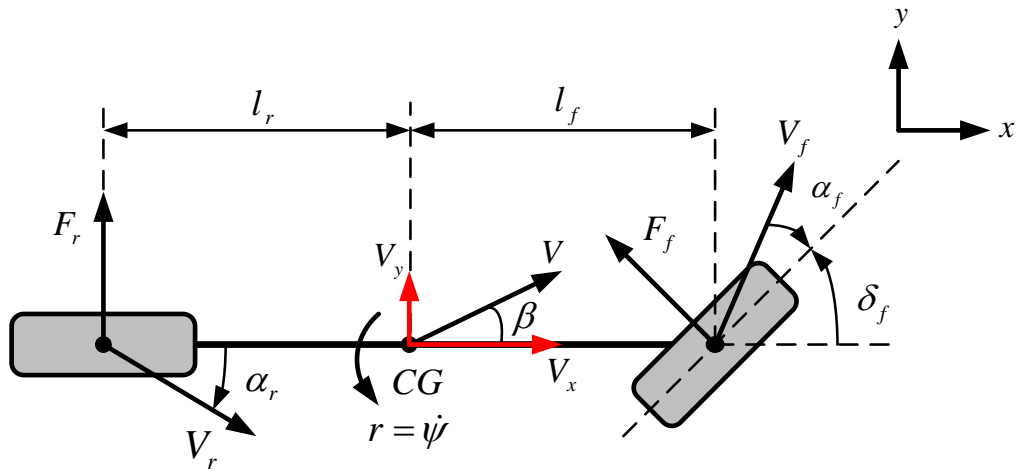


**Figure 5.2 :** The single track vehicle (bicycle) model.

The linearized two degrees-of-freedom single track model is given in state space representation as follows:

$$\dot{x} = Ax + Bu \quad (5.3)$$

where  $x = [\beta \ r]^T$ ,  $u = [\delta_f \ M_z]^T$ ,

$$A = \begin{bmatrix} \frac{-2(C_{yr} + C_{yf})\mu}{mV} & -1 + \frac{2(C_{yr}l_r + C_{yf}l_f)\mu}{mV^2} \\ \frac{2(C_{yr}l_r - C_{yf}l_f)\mu}{J} & \frac{-2(C_{yr}l_r^2 + C_{yf}l_f^2)\mu}{JV} \end{bmatrix}, \quad B = \begin{bmatrix} \frac{2C_{yf}\mu}{mV} & 0 \\ \frac{2C_{yf}l_f\mu}{J} & \frac{\mu}{J} \end{bmatrix}.$$

Here,  $M_z$  denotes the corrective yaw moment and  $J$  denotes the vehicle moment of inertia about yaw axis ( $5392 \text{ kgm}^2$ ). The other parameters have been defined previously.

The desired vehicle motion is represented as follows in state space form (see for ex. [84]):

$$\dot{x}_d = Ax_d + \begin{bmatrix} b_{11} \\ b_{21} \end{bmatrix} \delta_f \quad (5.4)$$

Define an error state between the actual state  $x$  and the desired state  $x_d$  as follows:

$$e = x - x_d \quad (5.5)$$

Differentiating the error in (5.5) yields the tracking error dynamics:

$$\dot{e} = \dot{x} - \dot{x}_d = Ae + \begin{bmatrix} b_{12} \\ b_{22} \end{bmatrix} M_z \quad (5.6)$$

Equation (5.6) describes the dynamic relation between the state tracking deviations and the corrective yaw moment.

After the determination of the tracking error dynamics, the optimal corrective yaw moment is calculated as follows:

$$M_z^* = -k_1 (\beta - \beta_d) - k_2 (r - r_d) \quad (5.7)$$

where the gains  $k_1$  and  $k_2$  are determined based on LQR optimal control theory by minimizing the cost function

$$J = \int_0^{\infty} \left[ q_1 (\beta - \beta_d)^2 + q_2 (r - r_d)^2 \right] dt \quad (5.8)$$

It is seen from (5.3) that the system matrix  $A$  and the input matrix  $B$  depend on the vehicle velocity ( $V$ ) and the tire-road friction coefficient ( $\mu$ ). In order to reduce this dependency, the LQR controller is scheduled with these variables.

Figure 5.3 shows the different regions of the velocity and friction coefficient. The point marked with a cross within each shaded area in Figure 5.3 shows the calculation point used. State feedback gains ( $k_1, k_2$ ) are calculated for these points and the calculated ( $k_1, k_2$ ) values are used within the shaded area. There are 12 shaded areas in Figure 5.3. These shaded areas are for three regions of friction value discretization chosen as snowy/icy ( $\mu < 0.45$ ), wet asphalt ( $0.45 \leq \mu < 0.85$ ) and dry asphalt ( $\mu \geq 0.85$ ). Also, four velocity level discretizations are chosen as low speed ( $V < 45 \text{ km/h}$ ), moderate speed ( $45 \leq V < 80 \text{ km/h}$ ), fast speed ( $80 \leq V < 130 \text{ km/h}$ ) and very fast speed ( $V \geq 130 \text{ km/h}$ ). These discretizations form the 12 shaded areas in Figure 5.3.

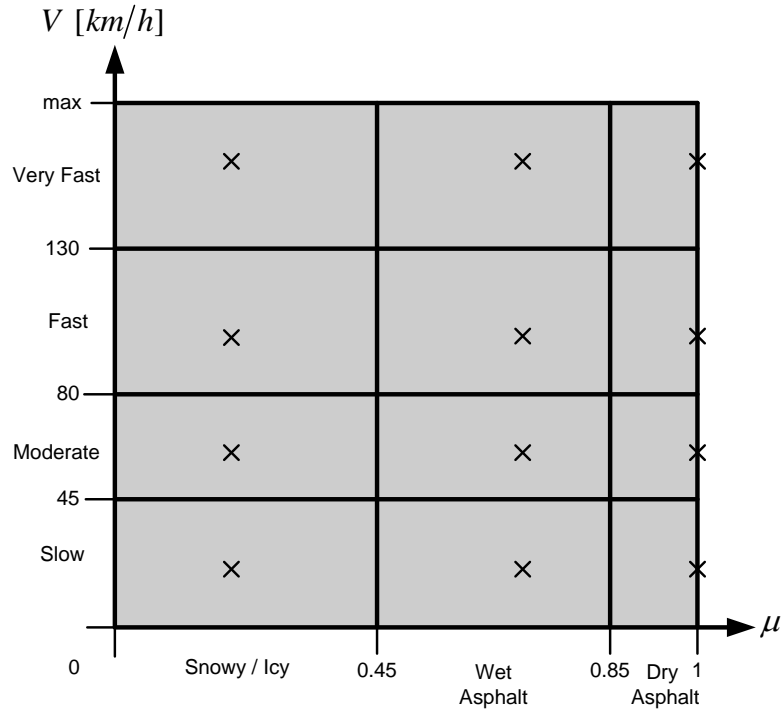


**Figure 5.3 :** The friction coefficient and velocity discretizations used for calculation of scheduled LQR gains.

### 5.2.3 Braking torque distribution algorithm

After the calculation of corrective yaw moment by the scheduled LQR controller, the braking torque distribution algorithm computes the individual wheel braking torques that will generate the computed corrective yaw torque. The braking torque distribution algorithm also determines which wheel will be braked.

Braking torques for individual wheels is calculated using (5.9) and (5.10) for the vehicle in Figure 5.4 [85]. These equations can be derived using moment relations between braking force and the corrective yaw moment and also using basic trigonometric relationships.

For the front wheels, the braking torques are calculated as

$$T_{bFL} = T_{bFR} = \frac{|M_z| R_{ef}}{\sin [\arctan ((l_{wF}/2)/l_f) - \delta_f] \sqrt{l_f^2 + (l_{wF}/2)^2}} \quad (5.9)$$

and for the rear wheels, the braking torques are calculated as

$$T_{bRL} = T_{bRR} = \frac{|M_z| R_{ef}}{\sin [\arctan ((l_{wR}/2)/l_r)] \sqrt{l_r^2 + (l_{wR}/2)^2}}. \quad (5.10)$$

Here,  $R_{ef}$  denotes the effective rolling radius of wheels ( $0.304\text{ m}$ ),  $l_{wF}$  and  $l_{wR}$  are the front track width ( $1.510\text{ m}$ ) and the rear track width ( $1.530\text{ m}$ ), respectively. The other parameters have been defined previously.

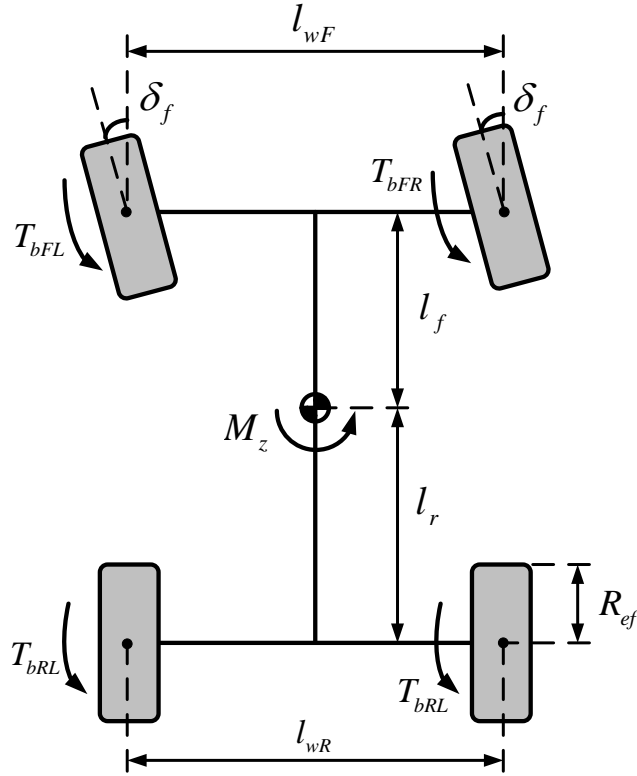


**Figure 5.4 :** Vehicle geometry for the braking torque distribution algorithm.

The main differences of the equations for front and rear wheels arise from the existence of the front wheel steering angle  $\delta_f$  in (5.9).

Six different cases are identified as seen Table 5.1 and also in Figure 5.5 and are used in determining which wheel should be braked individually [71, 86]. In Figure 5.5, the red vehicle (normal path) shows the vehicle's first uncontrolled situation, and the green vehicle (dashed path) shows the vehicle's situation after individual wheel braking occurs.

**Table 5.1 :** Different cases for braking torque distribution algorithm.

Case	Vehicle yaw rate	Desired yaw rate	Situation	Braking wheel
1	$r > 0$	$r_d \geq 0$	$r_d < r$	Front Right (FR)
2	$r \geq 0$	$r_d > 0$	$r_d > r$	Rear Left (RL)
3	$r < 0$	$r_d \geq 0$	$r_d > r$	Front Left (FL)
4	$r > 0$	$r_d < 0$	$r_d < r$	Front Right (FR)
5	$r \leq 0$	$r_d < 0$	$r_d < r$	Rear Right (RR)
6	$r < 0$	$r_d < 0$	$r_d > r$	Front Left (FL)

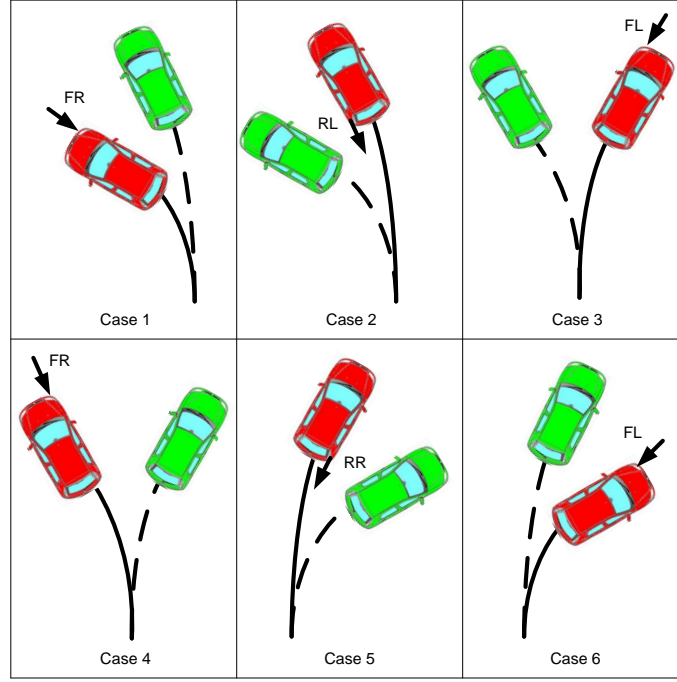


**Figure 5.5 :** Different cases for braking torque distribution algorithm.

#### 5.2.4 Electric motor torque reduction algorithm

The vehicle brake system generates limited braking torques due to physical limitations of the braking system hardware. The calculated yaw moment cannot be generated through individual braking alone in every situation. In other words, sometimes individual braking is not enough to realize the required corrective yaw moment. At these times, electric motor torque reduction is also used in order to achieve the desired vehicle lateral motion. When electric motor torque reduction is realized, the vehicle velocity reduces and the required lateral corrective maneuver of the vehicle (desired vehicle motion) occurs more easily.

For the vehicle in Figure 5.4, the maximum possible corrective yaw moment for the individual front wheel braking is calculated by the help of (5.9) as

$$M_{zf,max} = \left| \frac{T_{bf,max}}{R_{ef}} \sin(\theta_f - \delta_f) \sqrt{(l_{wF}/2)^2 + l_f^2} \right| \quad (5.11)$$

where  $\theta_f = \arctan\left(\frac{l_{wF}/2}{l_f}\right)$ .

Similarly, the maximum possible corrective yaw moment is calculated for the individual rear wheel braking by the help of (5.10) as follows:

$$M_{zr,max} = \left| \frac{T_{br,max}}{R_{ef}} \sin\theta_r \sqrt{(l_{wR}/2)^2 + l_r^2} \right| \quad (5.12)$$

where  $\theta_r = \arctan\left(\frac{l_{wR}/2}{l_r}\right)$ .

Here,  $T_{bf,max}$  and  $T_{br,max}$  denote maximum braking torques for front wheels (3500 Nm) and for rear wheels (1200 Nm), respectively. The other parameters have defined previously.

These equations are combined with the cases in Table 5.1 and Figure 5.5 to determine which of the maximum possible corrective yaw moments ( $M_{zf,max}$  or  $M_{zr,max}$ ) should be considered when the torque reduction algorithm runs. For example, if the cases 1, 3, 4 or 6 occur,  $M_{zf,max}$  is taken as  $M_{z,max}$ . If cases 2 or 5 occur,  $M_{zr,max}$  is taken as  $M_{z,max}$ .

The general torque reduction algorithm is written as follows:

$$T_{driving} = \begin{cases} T_{motorout} & \text{if } M_z^* \leq M_{z,max} \\ 0 & \text{if } M_z^* > M_{z,max} \end{cases} \quad (5.13)$$

where  $M_{z,max} = M_{zf,max}$  (for cases 1, 3, 4 or 6) and  $M_{z,max} = M_{zr,max}$  (for cases 2 or 5).

$M_z^*$  is the optimal corrective yaw moment calculated based on LQR theory.  $T_{motorout}$  is the electric motor torque before the application of torque reduction.

Note that in order to accurately simulate the electric motor dynamic response (i.e. time delay), a first order transfer function with time constant of 0.1 sec is utilized before the application of the driving torque reduction to the vehicle.

### 5.2.5 Wheel slip controller

The calculated braking torques are applied to the vehicle through regulating the wheel slip ratios. The wheel slip controller here consists of a bang-bang controller, i.e. it generates a control signal such as 0 or 1. This signal triggers the hydraulic brake modulation valve which is a solenoid-controlled, fast-acting directional control valve. As a result, the hydraulic brake actuator generates the individual wheel brake pressure. Figure 5.6 shows the control structure for wheel slip control. The slip ratios and the desired slip ratio calculations and the hydraulic brake actuator model will be explained in the following subsections.

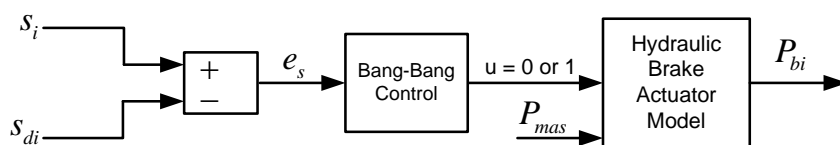


**Figure 5.6 :** Wheel slip control system structure.

### 5.2.5.1 Slip ratio calculation

During braking, the wheel slip ratio  $s_i$  is defined as

$$s_i = \frac{\omega_i R_{ef} - V_i}{V_i} \quad (5.14)$$

where  $V_i > \omega_i R_{ef}$  and  $i = FL, FR, RL, RR$ .

The angular velocities of wheels ( $\omega_i$ ) are measured by the ABS wheel speed sensors.

The longitudinal velocities of the wheel centers ( $V_i$ ) cannot be measured directly.

However, they can be calculated using [87] as follows:

$$V_{FL} = \sqrt{\left(V_x - \frac{l_{wF}}{2}r\right)^2 + (V_y + l_f r)^2} \cos \alpha_{FL} \quad (5.15)$$

$$V_{FR} = \sqrt{\left(V_x + \frac{l_{wF}}{2}r\right)^2 + (V_y + l_f r)^2} \cos \alpha_{FR} \quad (5.16)$$

$$V_{RL} = \sqrt{\left(V_x - \frac{l_{wR}}{2}r\right)^2 + (V_y - l_r r)^2} \cos \alpha_{RL} \quad (5.17)$$

$$V_{RR} = \sqrt{\left(V_x + \frac{l_{wR}}{2}r\right)^2 + (V_y - l_r r)^2} \cos \alpha_{RR} \quad (5.18)$$

where the tire slip angles  $\alpha_i$  are

$$\alpha_{FL,FR} = \delta_f - \arctan \left[ (V_y + l_f r) / \left( V_x \mp \frac{l_{wF}}{2}r \right) \right],$$

$$\alpha_{RL,RR} = -\arctan \left[ (V_y - l_r r) / \left( V_x \mp \frac{l_{wR}}{2}r \right) \right].$$

### 5.2.5.2 Desired slip ratio calculation based on scheduled LQR control

In order to obtain the desired slip ratios, the modified single track vehicle model can be written in state space representation as follows [88]:

$$\dot{x} = Ax + Bu + Ev \quad (5.19)$$

where  $x = [\beta \quad r]^T$ ,  $u = [\delta_f \quad M_z]^T$ ,  $v = s_i$ ,

$$A = \begin{bmatrix} \frac{-2(C_{yr} + C_{yf})\mu}{mV} & -1 + \frac{2(C_{yr}l_r + C_{yf}l_f)\mu}{mV^2} \\ \frac{2(C_{yr}l_r - C_{yf}l_f)\mu}{J} & \frac{-2(C_{yr}l_r^2 + C_{yf}l_f^2)\mu}{JV} \end{bmatrix}, B = \begin{bmatrix} \frac{2C_{yf}}{mV} & 0 \\ \frac{2C_{yf}l_f\mu}{J} & \frac{\mu}{J} \end{bmatrix}, E = \begin{bmatrix} 0 \\ \frac{l_{wR}C_{xi}\mu}{2J} \end{bmatrix}.$$

Here,  $C_{xi}$  denotes the longitudinal stiffness for the  $i$ th wheel (128000 N). The other parameters have been defined previously.

Define the error state between the actual state  $x$  and the desired state  $x_d$  as

$$e = x - x_d \quad (5.20)$$

Differentiating the error in (5.20) yields the tracking error dynamics:

$$\dot{e} = \dot{x} - \dot{x}_d = Ae + Ev + Ax_d + Bu \quad (5.21)$$

Treating the third and fourth terms in (5.21) as disturbances, the LQR control theory is applied and the desired slip ratios are calculated as

$$s_{di}^* = -k_1(\beta - \beta_d) - k_2(r - r_d) \quad (5.22)$$

where the gains  $k_1$  and  $k_2$  are determined based on LQR optimal control that minimizes the cost function

$$J = \int_0^{\infty} \left[ q_1(\beta - \beta_d)^2 + q_2(r - r_d)^2 \right] dt. \quad (5.23)$$

The desired slip ratios in (5.22) calculated by the LQR controller are multiplied by the braking torque conditions in order to ensure the longitudinal slip condition of the tires. If the braking torque distribution algorithm calculates a braking torque for the tire, this condition is taken as 1 and the calculated desired slip ratio ( $s_d$ ) is used in the following slip ratio control loop. If there is no braking calculated by the braking torque distribution algorithm, this condition is taken as 0. As a result, the desired slip ratio becomes zero. Since there is no braking in this situation, the absence of longitudinal slip on tires is plausible. The desired slip ratio is limited by 0.3 in absolute value (longitudinal slip is negative during braking). Larger values of longitudinal slip may result in lower lateral tire forces due to the coupling between tire longitudinal and lateral forces.

### 5.2.5.3 Hydraulic brake actuator model for calculation of tire brake pressures

The wheel slip controller determines the control signal values depending on the difference between the slip ratio and the desired slip ratio. After the determination of the control signal, this signal is used to drive the hydraulic brake actuator. The hydraulic brake model can be represented as a solenoid controlled valve and actuator.

A solenoid-flow control valve type actuator is modeled as follows [89]:

$$\dot{P}_{bi} = \begin{cases} -\frac{1}{K_{1i}}P_{bi} & \text{when solenoid is on.} \\ \frac{1}{K_{2i}}(P_{mas} - P_{bi}) & \text{when solenoid is off.} \end{cases} \quad (5.24)$$

where  $P_{bi}$  is the brake pressure of the  $i$ th wheel,  $P_{mas}$  is the master cylinder pressure,  $K_{1i}$  and  $K_{2i}$  are the coefficients of the hydraulic brake actuator model for the  $i$ th wheel.

In other words, considering the control input  $u$ , the brake actuator model can be written as in (5.25):

$$\dot{P}_{bi} = -\frac{1}{K_{1i}}P_{bi} + u_i \left[ \frac{1}{K_{2i}}(P_{mas} - P_{bi}) + \frac{1}{K_{1i}}P_{bi} \right] \quad (5.25)$$

where the solenoid on/off signal  $u_i$  is either 1 or 0. According to (5.25), if  $u_i$  is equal to 1, the tire brake pressure  $P_{bi}$  increases and if  $u_i$  is equal to 0, the tire brake pressure  $P_{bi}$  decreases.

### 5.3 RB-LSC System Structure

The second approach is based on regenerative braking based lateral stability control. In this approach, only the electric motor torque is regulated to stabilize the vehicle behavior according to the error values of side slip angle and yaw rate without individual braking. The control system is much simpler than the ILSC system. The aim of the RB-LSC system is to provide vehicle stability in a more economic and simplistic way, using fewer numbers of sensors and actuators. The RB-LSC system also provides a measure of lateral stability improvement possible with only drive motor torque reduction as compared to simultaneous use of torque reduction and individual wheel braking. Two different RB-LSC structures are presented in the following subsections.

#### 5.3.1 Bang-bang control based algorithm (RB-LSC1)

In the first algorithm, a bang-bang controller is used to regulate electric motor torque according to the error values of side slip angle and yaw rate. When these values exceed the predefined limit values, the regenerative braking is performed.

The first algorithm (RB-LSC1) can be written as follows:

$$T_{driving} = \begin{cases} T_{b,regen} & \text{if } |e_{\beta}| \geq e_{\beta,max} \text{ and } |e_r| \geq e_{r,max} \\ T_{motorout} & \text{otherwise} \end{cases} \quad (5.26)$$

### 5.3.2 PD control based algorithm (RB-LSC2)

Figure 5.7 shows the structure of the PD control based second algorithm. PD controller is utilized to regulate electric motor torque according to vehicle yaw rate error. In order to make the algorithm simpler than algorithm 1, only yaw rate error is used in the feedback loop. Note that yaw rate can be easily measured by sensors. In contrast with the yaw rate, the side slip angle must be estimated.

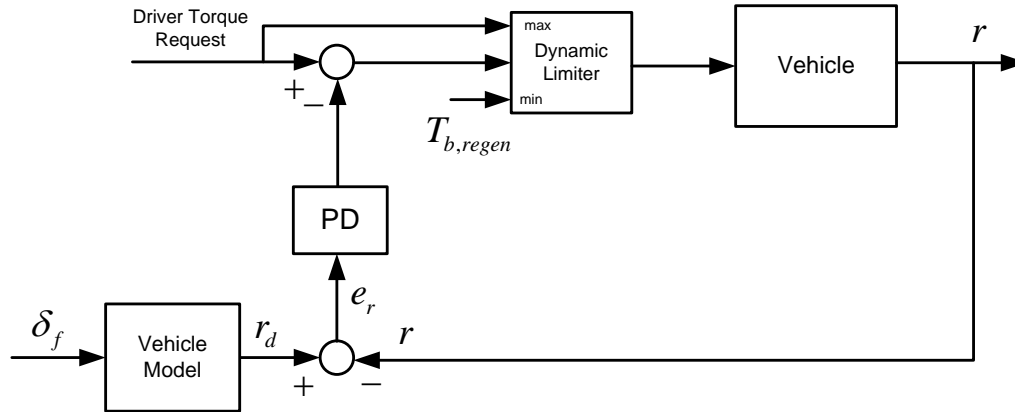


**Figure 5.7 :** The PD control based algorithm (RB-LSC2) system structure.

A dynamic limiter is used before the calculated torque value is realized by the electric motor. The upper limit of the dynamic limiter is the driver torque request and the lower limit is the maximum possible negative torque that can be generated by regenerative braking. The aim of the dynamic limiter is to prevent maximum torque values which are not requested by the driver and minimum torque values (maximum negative torque) that cannot be generated by the regenerative braking.

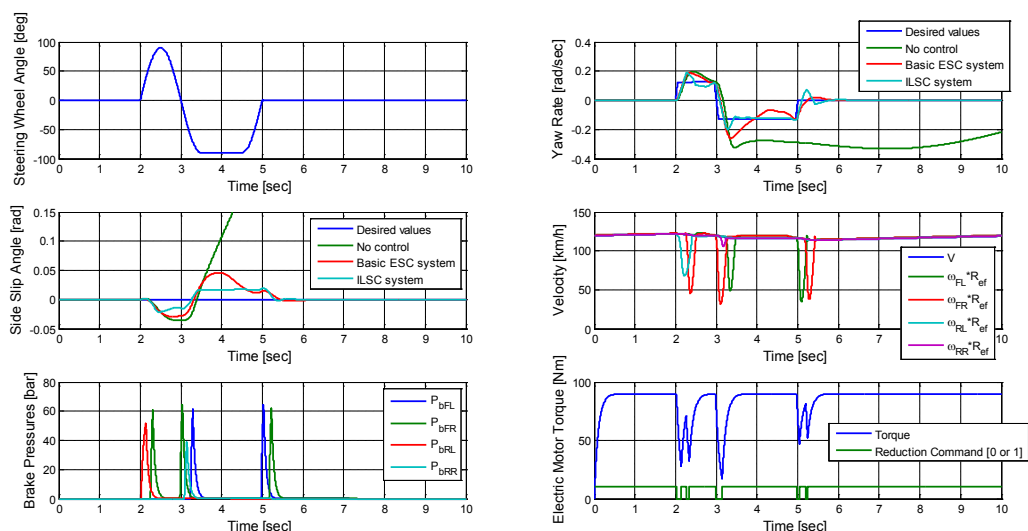
## 5.4 Simulations

The proposed lateral control systems were tested through simulations. CarSim and Matlab/Simulink software were used to carry out the simulations. A realistic, validated model of a fully electric light commercial vehicle was constructed within the CarSim environment. ILSC, RB-LSC1 and RB-LSC2 controllers and the hydraulic system model were constructed in the Simulink environment and connected to the CarSim vehicle. Exemplary simulations were reported here using this CarSim/Simulink model to test the effectiveness of the proposed control systems. The ILSC and the two RB-LSC lateral stability control systems were tested using sine-with-dwell and fishhook maneuvers on severe road conditions. A benchmark controller called the

Basic ESC was also used in comparisons. The Basic ESC is a PID based differential braking lateral stability controller. In this controller, the corrective yaw moment is calculated using yaw rate error and the calculated moment is applied to the vehicle via differential braking. Moreover, ILSC and the Basic ESC was tested and compared each other with NHTSA FMVSS No. 126 standart ESC regulation test. The results are presented in the following sections.

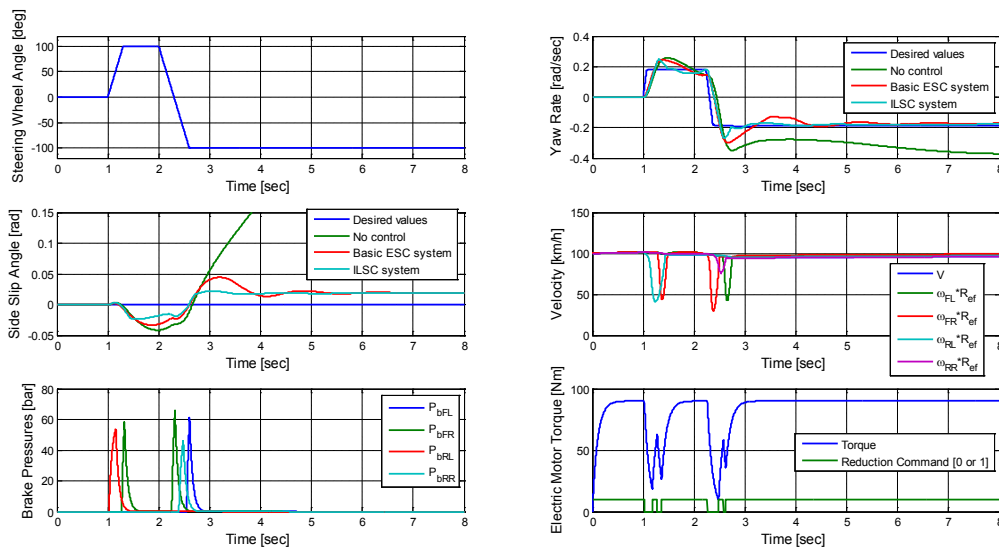
#### 5.4.1 ILSC system simulation results

Figure 5.8 depicts the simulation results for a sine-with-dwell test in the severe condition ( $\mu = 0.5$ ). The vehicle begins the motion with the initial velocity of 120 km/h and quarter open (25%) throttle. The uncontrolled vehicle becomes unstable. However, the ILSC equipped vehicle follows the desired side slip angle and the yaw rate successfully. The lateral stability of the vehicle was obtained by individual braking and electric motor torque reduction. The rear left and front right wheels were used for braking according to the braking torque distribution algorithm. For the ILSC system equipped vehicle, the wheel velocities do not take zero values. In other words, the vehicle wheels are not locking up. This shows the effectiveness of the wheel slip controller. The sine-with-dwell simulation shows that the proposed ILSC system improved the lateral stability of the vehicle significantly.



**Figure 5.8 :** The ILSC system simulation results for sine-with-dwell test ( $\mu = 0.5$ , 25% of Throttle).

Figure 5.9 depicts the simulation results for a fishhook test in the severe condition ( $\mu = 0.6$ ). The vehicle begins the motion with the initial velocity of 100 km/h and quarter open (25%) throttle. After a short duration of steering input, the uncontrolled vehicle shows an unstable behaviour. In contrast with the uncontrolled vehicle, the ILSC equipped vehicle follows the desired side slip angle and the yaw rate successfully. These simulation results show that the proposed ILSC system improves the vehicle lateral stability significantly.



**Figure 5.9 :** The ILSC system simulation results for fishhook test ( $\mu = 0.6$ , 25% of Throttle).

#### 5.4.2 RB-LSC system simulation results

Figures 5.10 and 5.11 show the simulation results which are obtained for sine-with-dwell and fishhook tests, respectively, when the RB-LSC1 system is used. The simulation conditions are the same as in the previous ILSC system tests. It is known that the uncontrolled vehicle becomes unstable for these tests (see Figures 5.8 and 5.9). The lateral stability of the vehicle was realized using the proposed RB-LSC1 system. In other words, the vehicle yaw rate and the vehicle side slip angle are bounded and they do not diverge from their desired values. Besides it must be mentioned that the tracking performance of the RB-LSC1 system is worse than that of the ILSC system, but the RB-LSC1 system is a simpler system with fewer number of sensors, estimators and actuators.

Table 5.2 shows the comparison of the proposed systems according to the sensors, estimators and actuators used in these systems. ILSC system employed six elements in total. It is three more than RB-LSC1 and four more than RB-LSC2. This is an advantage for the RB-LSC systems.

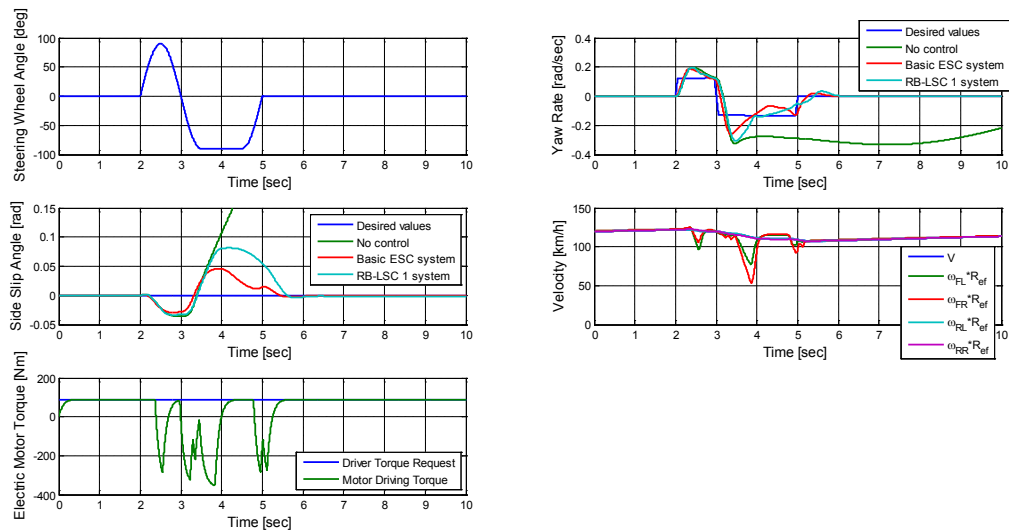


**Figure 5.10 :** The RB-LSC1 system simulation results for sine-with-dwell test ( $\mu = 0.5$ , 25% of Throttle).

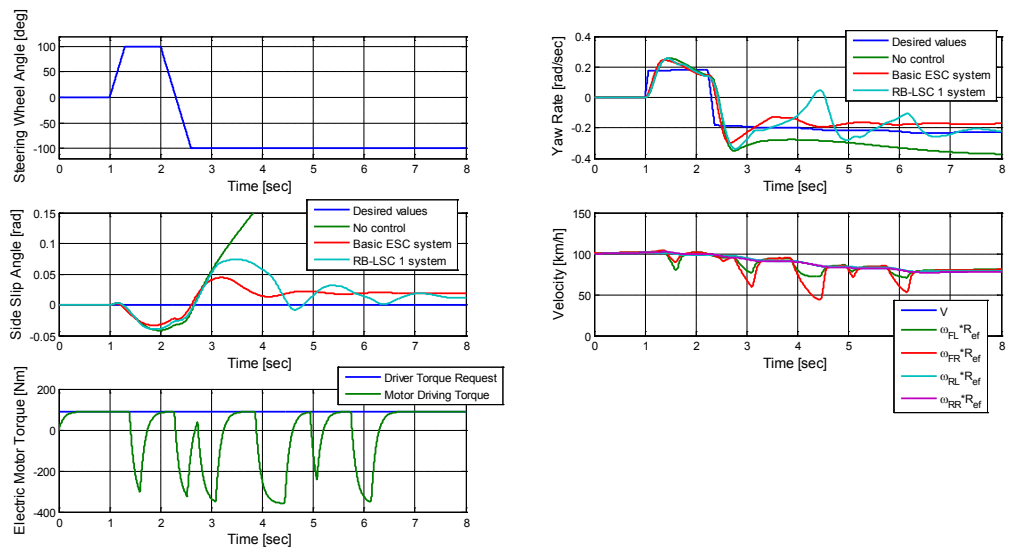


**Figure 5.11 :** The RB-LSC1 system simulation results for fishhook test ( $\mu = 0.6$ , 25% of Throttle).

Figures 5.12 and 5.13 show the simulation results which are obtained for sine-with-dwell and fishhook tests respectively when the RB-LSC2 system is used. The RB-LSC2 system equipped vehicle shows stable lateral behaviour. The vehicle yaw rate and the vehicle side slip angle do not diverge from their desired values.

**Table 5.2 :** Comparison of the ILSC and RB-LSC systems according to the sensor, estimator and actuator usage.

Sensor / Estimator / Actuator	ILSC	RB-LSC1	RB-LSC2
Yaw rate sensor	+	+	+
Steering wheel sensor	+	–	–
Side slip estimator	+	+	–
Vehicle speed estimator	+	–	–
Individual braking actuator	+	–	–
Electric motor torque reduction/regulation	+	+	+

The tracking performance of the RB-LSC2 system is similar to that of the RB-LSC1 system. However, the RB-LSC2 algorithm utilizes only the yaw rate error for the feedback control and it does not need the side slip error for the feedback control. This is an advantage for the RB-LSC2 system.

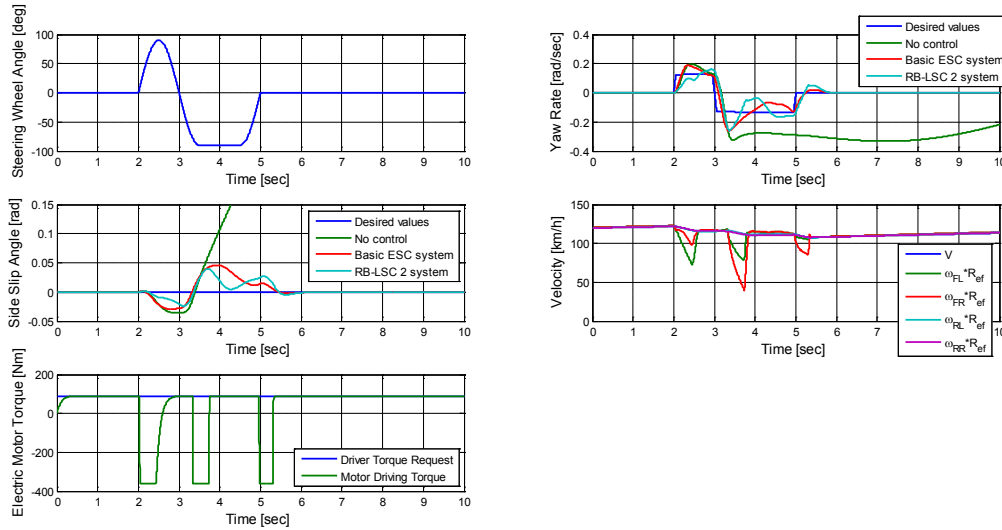


**Figure 5.12 :** The RB-LSC2 system simulation results for sine-with-dwell test ( $\mu = 0.5$ , 25% of Throttle).

The aforementioned control systems and uncontrolled case are compared each other numerically using error values. The error values are calculated using the below equation:

$$\text{error} = \frac{1}{n} \sum_{i=1}^n |\text{actual\_value}(i) - \text{desired\_value}(i)| \quad (5.27)$$

where  $n$  shows the number of data points. Error calculations are performed for the yaw rate and the side slip angle which are the most important indicators of lateral stability of the vehicle. The calculated error values are shown in Table 5.3. According to the results, the minimum errors of yaw rate and side slip angle are obtained by ILSC system both for the sine-with-dwell and the fishhook maneuvers. Basic ESC system is

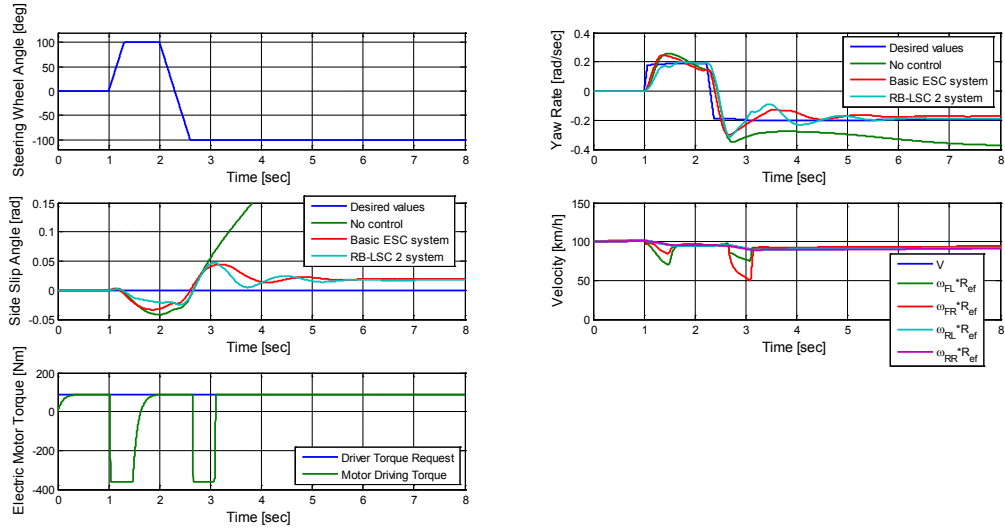


**Figure 5.13 :** The RB-LSC2 system simulation results for fishhook test ( $\mu = 0.6$ , 25% of Throttle).

better than RB-LSC1 for both maneuvers. According to the yaw rate error, Basic ESC is more preferred than RB-LSC2, but RB-LSC2 is slightly better than Basic ESC for the side slip error. Moreover, RB-LSC2 shows improved performance than RB-LSC1 by means of yaw rate and side slip errors.

**Table 5.3 :** Comparison of the proposed systems according to the error values.

	Sine-with-dwell maneuver		Fishhook maneuver	
	Yaw rate error [rad/sec]	Side slip error [rad]	Yaw rate error [rad/sec]	Side slip error [rad]
No Control	0.1871	0.3934	0.1028	0.2349
Basic ESC	0.0181	0.0080	0.0252	0.0187
ILSC	0.0110	0.0050	0.0169	0.0153
RB-LSC1	0.0217	0.0156	0.0524	0.0228
RB-LSC2	0.0219	0.0060	0.0287	0.0157

The stroboscopic plots for the sine-with-dwell and the fishhook maneuvers are depicted in Figure 5.14 and Figure 5.15, respectively. The trajectory of the vehicles can be seen from these plots. It is seen that the controlled vehicles follows the trajectory but the uncontrolled vehicle shows the unstable behaviour.

### 5.4.3 FMVSS No. 126 test simulation results

The standart NHTSA FMVSS No. 126 ESC regulation test is performed for all aforementioned control systems. In this test, 0.7 Hz sine-with-dwell maneuver is used. Steering is initiated at vehicle velocity of 80.5 km/h. Two series of tests are carried out

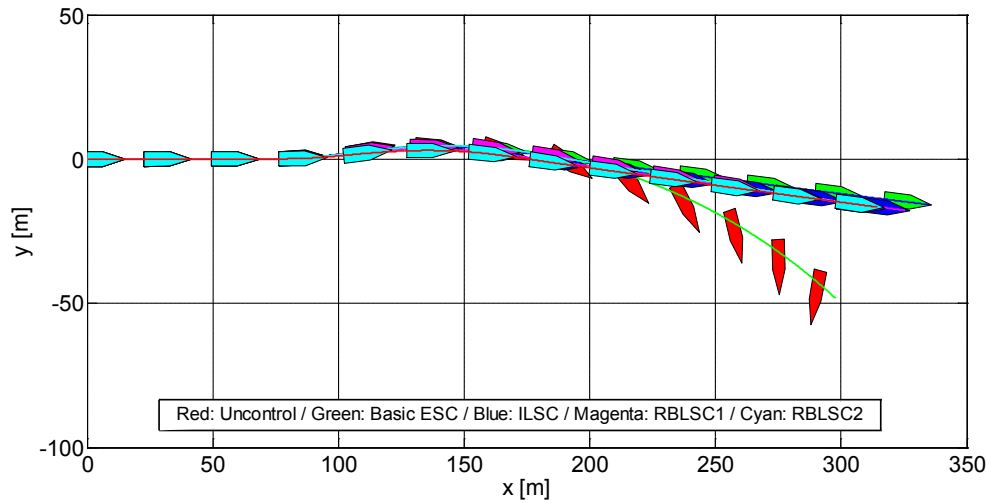


**Figure 5.14 :** Stroboscopic plots for sine-with-dwell maneuver.

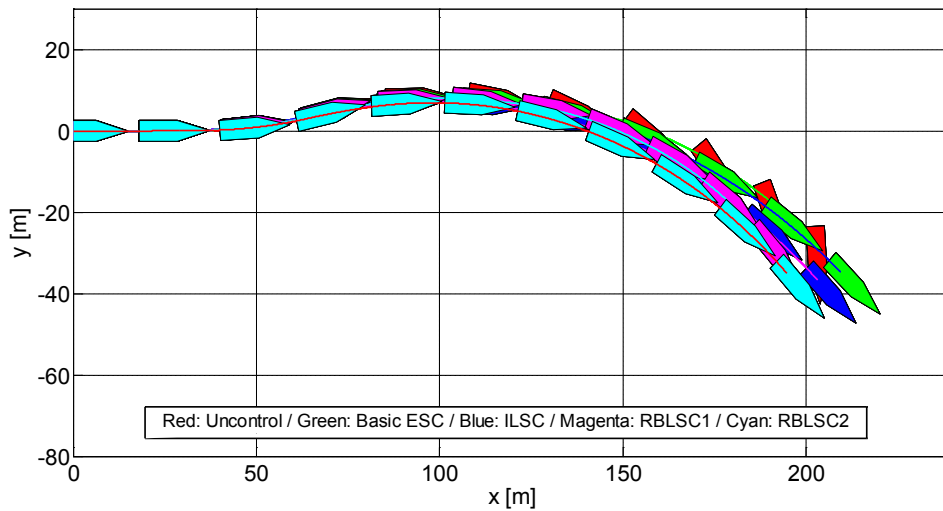


**Figure 5.15 :** Stroboscopic plots for fishhook maneuver.

with left-right and with right-left steering maneuver. Each series of tests begins with a test run with a moderate steering wheel angle. The steering wheel angle is increased from run to run in a series until a termination criterion is reached. More information about this test can be found in [90]. The Basic ESC and ILSC systems passed the FMVSS No. 126 test. The results are shown in Figure 5.16 for yaw rate, side slip angle, peak yaw rate and lateral acceleration. The numerical values are given in Table 5.4 for comparison of the Basic ESC and ILSC systems. According to the values in Table 5.4, ILSC system equipped shows less yaw rate, side slip angle and lateral acceleration values than the Basic ESC equipped vehicle while passing the FMVSS No. 126 test. Therefore, it can be stated that the stability performance of the ILSC equipped vehicle is better than the Basic ESC equipped vehicle according to the FMVSS No. 126 test.

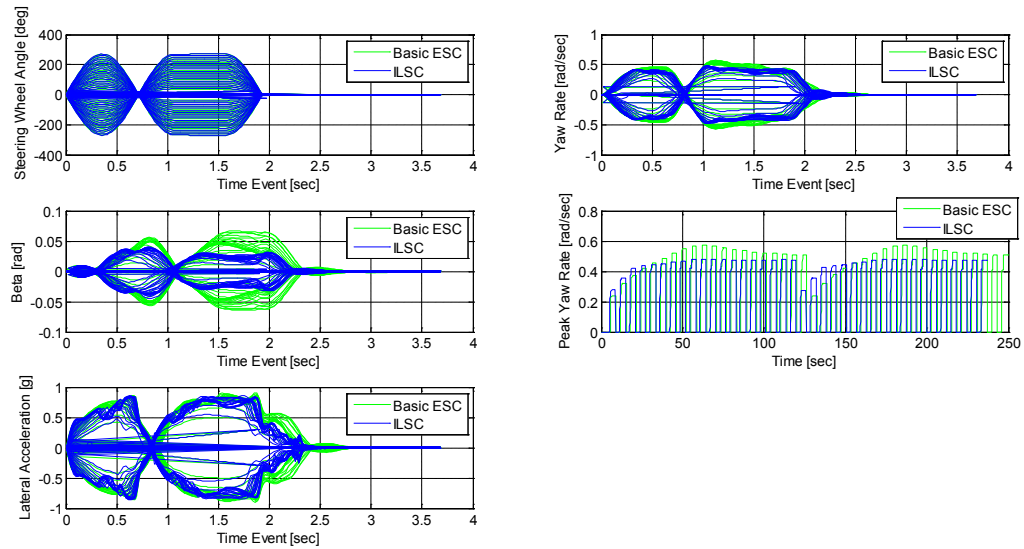


**Figure 5.16 :** The Basic ESC and the ILSC system simulation results for FMVSS No. 126 test.

**Table 5.4 :** Comparison of the Basic ESC and ILSC systems according to FMVSS No. 126 test.

	Min. yaw rate [rad/sec]	Max. yaw rate [rad/sec]	Min. side slip [rad]	Max. side slip [rad]	Min. lateral acc. [g]	Max. lateral acc. [g]
Basic ESC	-0.5715	0.5710	-0.0646	0.0667	-0.9111	0.9035
ILSC	-0.4797	0.4793	-0.0445	0.0403	-0.8555	0.8672

RB-LSC systems did not pass the FMVSS No. 126 test. However, these systems can be still used as cheaper alternative support systems in order to correct the yaw dynamics of vehicles not equipped with ESC in a limited manner. The results given in Figures 5.10 - 5.13 show that they can at least stabilize the unstable vehicle dynamics. Also, the application of these systems to the vehicle can be easily realized, only electric motor torque control is sufficient for implementing these control systems.

## 5.5 Conclusion

The ILSC and RB-LSC systems were presented in this chapter to improve the lateral stability of a fully electric vehicle. The effectiveness of the proposed control systems have been verified through realistic CarSim simulations using a validated model of a fully electric light vehicle. Several simulation studies were carried out. In the first test, a sine-with-dwell maneuver was performed and in the second test, a fishhook test was carried out for evaluating the proposed control systems. According to

these simulations, it was shown that the lateral stability of the electric vehicle was significantly improved by the proposed ILSC system. The ILSC system results were better than the Basic ESC system according to the error value comparisons. Also, unstable vehicle behaviour was stabilized using the much simpler RB-LSC approaches. It was seen that RB-LSC can be used to stabilize the vehicle unstable behaviour albeit its relatively poor performance as compared to the ILSC system. As a third test, the FMVSS No. 126 performance of ILSC and the Basic ESC was compared. Although both of them passed the test, ILSC system equipped vehicle showed better performance by means of obtained yaw rate, side slip angle and lateral acceleration.

## 6. CONCLUSIONS AND RECOMMENDATIONS

This thesis presents the discussion on advanced control methods for ground vehicles. The design of control systems for automotive applications is one of the most important application areas of advanced control systems theory. The four important vehicle control problems were investigated in this thesis from different perspectives. In general, the parameter space approach based robust control and disturbance observer based control systems were used as solution methodology for the vehicle control problems which include uncertain parameters, unmodeled dynamics and time delays.

In Chapter 2, the parameter space approach based robust control methodology was applied DC motor speed control. The tracking and disturbance rejection properties of the proposed robust PI control system were improved by using add-on disturbance observer. The disturbance observer design performed based on the stability robustness of the overall system. The improvement of the system response in terms of tracking performance and disturbance rejection was demonstrated by the simulations and experiments. Three different experiments were conducted in order to test the proposed control scheme: trajectory tracking experiment, step disturbance rejection experiment and ramp disturbance rejection experiment. The robust PI plus disturbance observer system showed better performances for all the experiments. The main contribution of this chapter is providing step-by-step robust controller design based on the parameter space and the disturbance observer based control approaches considering the multi-objective design requirements such as Hurwitz stability, D-stability, phase margin boundary and frequency domain specifications.

In Chapter 3, the time delay problems in automotive control applications were investigated. Communication disturbance observer approach based compensation of the time delay in plants was introduced. A novel robust stability condition for the cases of constant and time varying delay was established. This condition can be used to design robustly stable communication disturbance observer based delay compensation systems. The vehicle yaw stability control problem over CAN bus, which suffers from

time varying delay, was discussed. Communication disturbance observer approach was used to compensate the network-induced delays in vehicle yaw stability control over CAN bus. Using the proposed robust stability condition, the communication disturbance observer designed and first-time applied to an automotive control problem (the vehicle yaw stability control problem over CAN bus). It was seen that the time varying delay causes instability in the case of only PI control but in the case of add-on communication disturbance observer, the vehicle becomes stable and also the yaw rate of the vehicle follows the desired yaw rate successfully.

In Chapter 4, the problem of the robust automatic steering control for autonomous vehicles was discussed. The parameter space approach based robust PID control design satisfying D-stability requirements was applied to the problem. A validated nonlinear vehicle model was employed for the test of the designed controller. Two specific example tests were carried out. Then robust steering control of the automated vehicle was realized based on digital map and GPS measurements which determine the vehicle position according to the global coordinates. This methodology is different from the previous one. The lateral deviation and the yaw angle error of the vehicle are calculated by comparing the desired trajectory (the generated map) and the vehicle position in real time. High resolution digital map was generated by the solution of the constrained least square problem. An eight segments desired trajectory was followed successfully by the vehicle using the proposed algorithm. The main contribution of this chapter is using the designed robust steering controller together with the lateral deviation and the yaw angle error calculation algorithm in real time. The error calculation algorithm generates the required feedback signal (the lateral deviation of the vehicle at the preview distance) to the robust steering control system and the vehicle tracks the desired trajectory (the generated map) by using this lateral deviation information.

In Chapter 5, the lateral stability control problem of a fully electric vehicle was examined. Two novel control system structures were proposed to follow the desired vehicle side slip angle and vehicle yaw rate values successfully, thereby improving vehicle's lateral stability. The proposed first method -ILSC- is based on corrective yaw moment calculation, braking torque distribution and electric motor torque reduction. The proposed second method -RB-LSC- uses electric motor torque regulation to provide lateral stability of the vehicle without individual braking intervention. Two

different RB-LSC algorithms were proposed: bang-bang control based algorithm (RB-LSC1) and PD control based algorithm (RB-LSC2). Also, a benchmark controller -the Basic ESC- was developed for the comparison of the proposed controllers. Two specific tests (the sine-with-dwell and the fishhook tests) were carried out to analyze the designed controllers. Error calculations were performed for the yaw rate and the side slip angle which are the most important indicators of the lateral stability of the vehicle. According to the results, the minimum errors of yaw rate and side slip angle were obtained by the proposed ILSC system both for the sine-with-dwell and the fishhook tests. Also, the standard ESC regulation test (FMVSS No. 126) was performed. The Basic ESC and ILSC systems were passed the FMVSS No. 126 test. RB-LSC systems did not pass the system. However, it was determined that these systems can be used as cheaper alternative support systems in a limited manner.

There are many potential extensions to the work presented in this thesis. Possible future extensions of this study include investigating usage of different kind of filters in disturbance observer design such as fractional order filters; application of communication disturbance observer to the different automotive control problems such as cooperative adaptive cruise control; expanding lateral deviation and the yaw angle error calculation algorithm in robust steering control system to work in the case of unavailable GPS signals; and usage of different control methods such as robust  $H_\infty$  control in the lateral stability control of fully electric vehicles.



## REFERENCES

- [1] **Guzzella, L. & Onder, C.**, (2006). Past, present and future of automotive control. In B.A. Francis, M.C. Smith, J.C. Willems (Eds.), *Control of Uncertain Systems: Modelling, Approximation, and Design, Lecture Notes in Control and Information Science* (Vol. 329, pp.163–182). Berlin-Heidelberg: Springer.
- [2] **Güvenç, L.** (2004). Preventive and active safety applications, *ICAT 2004 International Conference on Automotive Technology, Future Automotive Technologies on Powertrain and Vehicle*, Istanbul, Turkey, November 26.
- [3] **Erke, A.** (2008). Effects of electronic stability control (ESC) on accidents: A review of empirical evidence, *Accident Analysis & Prevention*, 40 (1), 167–173.
- [4] **Lie, A., Tingvall, C., Krafft, M. & Kullgren, A.** (2006). The effectiveness of electronic stability control (ESC) in reducing real life crashes and injuries, *Traffic Injury Prevention*, 7 (1), 38–43.
- [5] **Özgüner, Ü., Acarman, T. & Redmill, K.A.** (2011). *Autonomous Ground Vehicles*. Artech House.
- [6] **Hori, Y.** (2004). Future vehicle driven by electricity and control-research on four-wheel-motored "UOT Electric March II", *IEEE Transactions on Industrial Electronics*, 51 (5), 954–962.
- [7] **Emirler, M.T., Kahraman, K., Şentürk, M., Acar, O.U., Aksun Güvenç, B., Güvenç, L. & Efendioğlu, B.** (2011). Integrated lateral stability control for fully electric vehicles, *9th European Workshop on Advanced Control and Diagnosis (ACD 2011)*, Budapest, Hungary, November 17-18.
- [8] **Kahraman, K., Şentürk, M., Emirler, M.T., Bozkurt, E., Aksun Güvenç, B., Güvenç, L. & Efendioğlu, B.** (2012). Offline and hardware in the loop simulation model-system development for electronic stability control of a fully electric vehicle, *6th Automotive Technologies Congress (OTEKON)*, Bursa, Turkey: Uludağ University, June 4-5.
- [9] **Ackermann, J., Blue, P., Bunte, T., Güvenç, L., Kaesbauer, D., Kordt, M., Muhler, M. & Odenthal, D.** (2002). *Robust Control: The Parameter Space Approach*. Springer.
- [10] **Güvenç, L. & Ackermann, J.** (2001). Links between the parameter space and frequency domain methods of robust control, *International Journal of Robust and Nonlinear Control*, 11 (15), 1435–1453.

- [11] **Natori, K., Tsuji, T., Ohnishi, K., Hace, A. & Jezernik, K.** (2004). Robust bilateral control with internet communication. *Proceedings of the 30th Annual Conference of IEEE Industrial Electronics Society (IECON 2004)*, 3, (pp.2321–2326). Busan, Korea, November 2-6.
- [12] **Rossetter, E.J.** (2003). *A potential field framework for active vehicle lanekeeping assistance* (Ph.D. thesis). Stanford University, CA, USA.
- [13] **Zollo, L., Roccella, S., Guglielmelli, E., Carrozza, M.C. & Dario, P.** (2007). Biomechatronic design and control of an anthropomorphic artificial hand for prosthetic and robotic applications, *IEEE/ASME Transactions on Mechatronics*, 12 (4), 418–429.
- [14] **Yang, S.F. & Chou, J.H.** (2009). A mechatronic positioning system actuated using a micro DC-motor-driven propeller–thruster, *Mechatronics*, 19 (6), 912–926.
- [15] **Wu, W.** (2012). DC motor drive speed regulation: Using a repetitive control application in a flatbed scanner, *IEEE Industry Applications Magazine*, 18 (2), 38–46.
- [16] **Huang, Q., Huang, Z. & Zhou, H.** (2009). Nonlinear optimal and robust speed control for a light-weighted all-electric vehicle, *IET Control Theory & Applications*, 3 (4), 437–444.
- [17] **Murtaza, G. & Bhatti, A.** (2012). Control of DC motors using sliding mode. *Proceedings of the 9th IEEE International Bhurban Conference on Applied Sciences and Technology (IBCAST 2012)*, (pp.37–42). Islamabad, Pakistan, January 9-12.
- [18] **Ambesange, S.V., Kamble, S.Y. & More, D.** (2013). Application of sliding mode control for the speed control of DC motor drives. *Proceedings of the IEEE International Conference on Control Applications (CCA 2013)*, (pp.832–836). Hyderabad, India, August 28-30.
- [19] **Chang, S.Y., Yu, P.H. & Su, W.C.** (2013). Pre-and post-filtering approach to sensorless VSS speed control of a permanent magnet DC motor subject to Hammerstein and Wiener nonlinearities, *Control Engineering Practice*, 21 (11), 1577–1583.
- [20] **Cepeda, P., Ponce, P. & Molina, A.** (2012). A novel speed control for DC motors: Sliding mode control, fuzzy inference system, neural networks and genetic algorithms. *Proceedings of the 11th IEEE Mexican International Conference on Artificial Intelligence (MICAI 2012)*, (pp.116–121). San Luis Potosi, Mexico, October 27 - November 4.
- [21] **Lu, R., Li, S. & Xue, L.** (2008). Robust  $H_\infty$  optimal speed control of DC motor using LMI approach. *Proceedings of the IEEE Chinese Control and Decision Conference, (CCDC 2008)*, (pp.4350–4354). Yantai, China, July 2-4.

- [22] **Yasoobi, M., Khosravi, A. & Lari, A.** (2011). Mixed  $H_2/H_\infty$  fixed structure speed control of DC motor using IPSO algorithm. *Proceedings of the 2nd IEEE International Conference on Control, Instrumentation and Automation (ICCIA 2011)*, (pp.451–456). Shiraz, Iran: University of Shiraz, December 27-29.
- [23] **El-Samahy, A.** (2000). Speed control of DC motor using adaptive variable structure control. *Proceedings of the 31st IEEE Annual Power Electronics Specialists Conference, (PESC 2000)*, 3, (pp.1118–1123). Galway, Ireland, June 18-23.
- [24] **El-Sharkawi, M. & Weerasooriya, S.** (1990). Development and implementation of self-tuning tracking controller for DC motors, *IEEE Transactions on Energy Conversion*, 5 (1), 122–128.
- [25] **Rahman, M.A. & Ashraful Hoque, M.** (1997). Online self-tuning ANN-based speed control of a PM DC motor, *IEEE/ASME Transactions on Mechatronics*, 2 (3), 169–178.
- [26] **Bhushan, B. & Singh, M.** (2011). Adaptive control of DC motor using bacterial foraging algorithm, *Applied Soft Computing*, 11 (8), 4913–4920.
- [27] **Peng, J. & Dubay, R.** (2011). Identification and adaptive neural network control of a DC motor system with dead-zone characteristics, *ISA transactions*, 50 (4), 588–598.
- [28] **Muresan, C.I., Folea, S., Mois, G. & Dulf, E.H.** (2013). Development and implementation of an FPGA based fractional order controller for a DC motor, *Mechatronics*, 23 (7), 798–804.
- [29] **Öncü, S., Karaman, S., Güvenç, L., Ersolmaz, S.S., Öztürk, E.S., Çetin, E. & Sinal, M.** (2007). Robust yaw stability controller design for a light commercial vehicle using a hardware in the loop steering test rig. *Proceedings of the IEEE Intelligent Vehicles Symposium, (IV 2007)*, (pp.852–859). Istanbul, Turkey, June 13-15.
- [30] **Aksun Güvenç, B., Güvenç, L. & Karaman, S.** (2009). Robust yaw stability controller design and hardware-in-the-loop testing for a road vehicle, *IEEE Transactions on Vehicular Technology*, 58 (2), 555–571.
- [31] **Aksun Güvenç, B., Güvenç, L. & Karaman, S.** (2010). Robust MIMO disturbance observer analysis and design with application to active car steering, *International Journal of Robust and Nonlinear Control*, 20 (8), 873–891.
- [32] **Ohnishi, K.** (1987). A new servo method in mechatronics, *Trans. Jpn. Soc. Elect. Eng*, 107, 83–86.
- [33] **Umeno, T. & Hori, Y.** (1991). Robust speed control of DC servomotors using modern two degrees-of-freedom controller design, *IEEE Transactions on Industrial Electronics*, 38 (5), 363–368.

- [34] **Güvenç, L. & Srinivasan, K.** (1994). Friction compensation and evaluation for a force control application, *Mechanical Systems and Signal Processing*, 8 (6), 623–638.
- [35] **Aksun Güvenç, B., Necipoğlu, S., Demirel, B. & Güvenç, L.** (2013). Robust control of atomic force microscopy. In J.P. Davim (Ed.), *Mechatronics* (pp.103–132). Hoboken, NJ, USA: Wiley.
- [36] **Fan, X. & Tomizuka, M.** (2010). Robust disturbance observer design for a power-assist electric bicycle. *Proceedings of the IEEE American Control Conference (ACC 2010)*, (pp.1166–1171). Baltimore, Maryland, USA, June 30 - July 2.
- [37] **Satoh, T., Kaneko, K. & Saito, N.** (2012). Improving tracking performance of predictive functional control using disturbance observer and its application to table drive systems, *International Journal of Computers, Communications & Control*, 7 (3), 550–564.
- [38] **Luo, Y., Zhang, T., Lee, B., Kang, C. & Chen, Y.** (2013). Disturbance observer design with Bode's ideal cut-off filter in hard-disc-drive servo system, *Mechatronics*, 23 (7), 856–862.
- [39] **Aksun Güvenç, B. & Güvenç, L.** (2002). Robust two degree-of-freedom add-on controller design for automatic steering, *IEEE Transactions on Control Systems Technology*, 10 (1), 137–148.
- [40] **Åström, K., Apkarian, J. & Lacheray, H.** (n.d.). *Quanser engineering trainer (QET) series: DC motor control trainer (DCMCT) manual*. Quanser Inc., Ontario, Canada.
- [41] **Richard, J.P.** (2003). Time-delay systems: An overview of some recent advances and open problems, *Automatica*, 39 (10), 1667–1694.
- [42] **Gu, K. & Niculescu, S.I.** (2003). Survey on recent results in the stability and control of time-delay systems, *ASME Journal of Dynamic Systems, Measurement, and Control*, 125 (2), 158–165.
- [43] **Smith, O.J.** (1959). A controller to overcome dead time, *ISA Journal*, 6 (2), 28–33.
- [44] **Rao, A.S. & Chidambaram, M.** (2005). Enhanced Smith predictor for unstable processes with time delay, *Industrial & Engineering Chemistry Research*, 44 (22), 8291–8299.
- [45] **Normey-Rico, J.E. & Camacho, E.F.** (2009). Unified approach for robust dead-time compensator design, *Journal of Process Control*, 19 (1), 38–47.
- [46] **Kempf, C.J. & Kobayashi, S.** (1999). Disturbance observer and feedforward design for a high-speed direct-drive positioning table, *IEEE Transactions on Control Systems Technology*, 7 (5), 513–526.
- [47] **Zhong, Q.C. & Normey-Rico, J.E.** (2002). Control of integral processes with dead-time. Part 1: Disturbance observer-based 2DOF control scheme, *IEE Proceedings-Control Theory and Applications*, 149 (4), 285–290.

- [48] **Natori, K. & Ohnishi, K.** (2008). A design method of communication disturbance observer for time-delay compensation, taking the dynamic property of network disturbance into account, *IEEE Transactions on Industrial Electronics*, 55 (5), 2152–2168.
- [49] **Åström, K.J., Hang, C.C. & Lim, B.** (1994). A new Smith predictor for controlling a process with an integrator and long dead-time, *IEEE Transactions on Automatic Control*, 39 (2), 343–345.
- [50] **Matausek, M. & Micic, A.D.** (1999). On the modified Smith predictor for controlling a process with an integrator and long dead-time, *IEEE Transactions on Automatic Control*, 44 (8), 1603–1606.
- [51] **Hrovat, D. & Sun, J.** (1997). Models and control methodologies for IC engine idle speed control design, *Control Engineering Practice*, 5 (8), 1093–1100.
- [52] **Jankovic, M. & Kolmanovsky, I.** (2009). Developments in control of time-delay systems for automotive powertrain applications. In B. Balachandran, T. Kalmár-Nagy, D.E. Gilsinn (Eds.), *Delay Differential Equations: Recent Advances and New Directions* (pp.55–92). Newyork: Springer.
- [53] **Di Cairano, S., Yanakiev, D., Bemporad, A., Kolmanovsky, I.V. & Hrovat, D.** (2012). Model predictive idle speed control: Design, analysis, and experimental evaluation, *IEEE Transactions on Control Systems Technology*, 20 (1), 84–97.
- [54] **Baumann, J., Torkzadeh, D.D., Ramstein, A., Kiencke, U. & Schlegl, T.** (2006). Model-based predictive anti-jerk control, *Control engineering practice*, 14 (3), 259–266.
- [55] **Güvenç, L., Uygan, I.M.C., Kahraman, K., Karaahmetoğlu, R., Altay, İ., Şentürk, M., Emirler, M.T., Hartavi Karçı, A.E., Aksun Güvenç, B., Altuğ, E., Turan, M.C., Taş, Ö.Ş., Bozkurt, E., Özgüner, Ü., Redmill, K., Kurt, A. & Efendioğlu, B.** (2012). Cooperative adaptive cruise control implementation of Team Mekar at the grand cooperative driving challenge, *IEEE Transactions on Intelligent Transportation Systems*, 13 (3), 1062–1074.
- [56] **Öncü, S., van de Wouw, N. & Nijmeijer, H.** (2011). Cooperative adaptive cruise control: Tradeoffs between control and network specifications. *Proceedings of the 14th International IEEE Conference on Intelligent Transportation Systems (ITSC 2011)*, (pp.2051–2056). Washington, DC, USA: The George Washington Univeristy, October 5-7.
- [57] **Bosch-GmbH.** (2012). *CAN with flexible data-rate specification version 1.0*. Germany.
- [58] **Latrach, C., Kchaou, M., El Hajjaji, A. & Rabhi, A.** (2014).  $H_\infty$  networked fuzzy control for vehicle lateral dynamic with limited communication. *Proceedings of the 19th IFAC World Congress (IFAC 2014)*, (pp.6313–6318). Cape Town, South Africa, August 24-29.

- [59] **Talvala, K.L., Kritayakirana, K. & Gerdes, J.C.** (2011). Pushing the limits: From lanekeeping to autonomous racing, *Annual Reviews in Control*, 35 (1), 137–148.
- [60] **Broggi, A., Medici, P., Zani, P., Coati, A. & Panciroli, M.** (2012). Autonomous vehicles control in the VisLab intercontinental autonomous challenge, *Annual Reviews in Control*, 36 (1), 161–171.
- [61] **Ünyelioğlu, K.A., Hatipoğlu, C. & Özgüner, Ü.** (1996). Design and stability analysis of a lane following controller, *IEEE Transactions on Control Systems Technology*, 5 (1), 127–134.
- [62] **Broggi, A., Bertozzi, M., Fascioli, A., Bianco, C.G.L. & Piazzzi, A.** (1999). The ARGO autonomous vehicle’s vision and control systems, *International Journal of Intelligent Control and Systems*, 3 (4), 409–441.
- [63] **Ackermann, J., Guldner, J., Sienel, W., Steinhauser, R. & Utkin, V.I.** (1995). Linear and nonlinear controller design for robust automatic steering, *IEEE Transactions on Control Systems Technology*, 3 (1), 132–143.
- [64] **Marino, R., Scalzi, S. & Netto, M.** (2011). Nested PID steering control for lane keeping in autonomous vehicles, *Control Engineering Practice*, 19 (12), 1459–1467.
- [65] **Kahraman, K., Emirler, M.T., Şentürk, M., Aksun Güvenç, B., Güvenç, L. & Efendioğlu, B.** (2010). Estimation of vehicle yaw rate using a virtual sensor with a speed scheduled observer. *Proceedings of the 6th IFAC Symposium Advances in Automotive Control*, (pp.632–637). Munich, Germany, June 12-14.
- [66] **Autonomous path following experiment.** (2014). Retrieved May 26, 2014 from [http://www.youtube.com/watch?v=6MQdX4\\_dx4U](http://www.youtube.com/watch?v=6MQdX4_dx4U)
- [67] **Altay, İ., Aksun Güvenç, B. & Güvenç, L.** (2013). A simulation study of GPS/INS integration for use in ACC/CACC and HAD. *Proceedings of the 9th IEEE Asian Control Conference (ASCC 2013)*, (pp.1–8). Istanbul, Turkey, June 23-26.
- [68] **Rossetter, E.J., Switkes, J.P. & Gerdes, J.C.** (2003). A gentle nudge towards safety: Experimental validation of the potential field driver assistance system. *Proceedings of the IEEE American Control Conference (ACC 2003)*, 5, (pp.3744–3749). Denver, Colorado, USA, June 4-6.
- [69] **Rossetter, E., Switkes, J. & Gerdes, J.** (2004). Experimental validation of the potential field lanekeeping system, *International Journal of Automotive Technology*, 5 (2), 95–108.
- [70] **Aksun Güvenç, B., Bunte, T., Odenthal, D. & Güvenç, L.** (2004). Robust two degree-of-freedom vehicle steering controller design, *IEEE Transactions on Control Systems Technology*, 12 (4), 627–636.

- [71] **Emirler, M.T.** (2010). *Vehicle yaw rate estimation and vehicle lateral stability control (In Turkish)* (Master's thesis). Istanbul Technical University, Institute of Science and Technology, Istanbul, Turkey.
- [72] **Van Zanten, A.T., Erhardt, R. & Pfaff, G.** (1995). VDC, the vehicle dynamics control system of Bosch, *SAE Technical Paper, No: 950769*.
- [73] **Van Zanten, A.T.** (2000). Bosch ESP systems: 5 years of experience, *SAE Technical Paper, No: 2000-01-1633*.
- [74] **Tchamna, R. & Youn, I.** (2013). Yaw rate and side-slip control considering vehicle longitudinal dynamics, *International Journal of Automotive Technology, 14* (1), 53–60.
- [75] **Yim, S.** (2014). Fault-tolerant yaw moment control with steer-and brake-by-wire devices, *International Journal of Automotive Technology, 15* (3), 463–468.
- [76] **Canale, M., Fagiano, L., Milanese, M. & Borodani, P.** (2007). Robust vehicle yaw control using an active differential and IMC techniques, *Control Engineering Practice, 15* (8), 923–941.
- [77] **Chen, B.C. & Kuo, C.C.** (2014). Electronic stability control for electric vehicle with four in-wheel motors, *International Journal of Automotive Technology, 15* (4), 573–580.
- [78] **Feiqiang, L., Jun, W. & Zhaodu, L.** (2009). Motor torque based vehicle stability control for four-wheel-drive electric vehicle. *Proceedings of the 5th IEEE Vehicle Power and Propulsion Conference (VPPC 2009)*, (pp.1596–1601), Dearborn, MI, USA, September 7-11.
- [79] **Piyabongkarn, D., Rajamani, R., Grogg, J.A. & Lew, J.Y.** (2009). Development and experimental evaluation of a slip angle estimator for vehicle stability control, *IEEE Transactions on Control Systems Technology, 17* (1), 78–88.
- [80] **Rajamani, R., Piyabongkarn, D., Lew, J.Y., Yi, K. & Phanomchoeng, G.** (2010). Tire-road friction-coefficient estimation, *IEEE Control Systems Magazine, 30* (4), 54–69.
- [81] **Jiang, F. & Gao, Z.** (2000). An adaptive nonlinear filter approach to the vehicle velocity estimation for ABS. *Proceedings of the IEEE International Conference on Control Applications (CCA 2000)*, (pp.490–495). Anchorage, Alaska, USA, September 25-27.
- [82] **Kiencke, U. & Nielsen, L.** (2000). *Automotive Control Systems for Engine, Driveline, and Vehicle*. Springer-Verlag, Berlin.
- [83] **Rajamani, R.** (2006). *Vehicle Dynamics and Control*. Springer, New York.
- [84] **Geng, C., Uchida, T. & Hori, Y.** (2007). Body slip angle estimation and control for electric vehicle with in-wheel motors. *Proceedings of the 33rd Annual Conference of the IEEE Industrial Electronics Society, (IECON 2007)*, (pp.351–355). Taipei, Taiwan, November 5-8.

- [85] **Falcone, P., Eric Tseng, H., Borrelli, F., Asgari, J. & Hrovat, D.** (2008). MPC-based yaw and lateral stabilisation via active front steering and braking, *Vehicle System Dynamics*, 46 (S1), 611–628.
- [86] **Yang, X., Wang, Z. & Peng, W.** (2009). Coordinated control of AFS and DYC for vehicle handling and stability based on optimal guaranteed cost theory, *Vehicle System Dynamics*, 47 (1), 57–79.
- [87] **Naderi, P., Bathaee, S. & Hoseinnezhad, R.** (2008). A multi objective fuzzy-based controller for front differential vehicles by electrical traction system. *Proceedings of the 4th IEEE International Conference on Wireless Communications, Networking and Mobile Computing (WiCOM 2008)*, (pp.8088–8097). Dalian, China, October 12-17.
- [88] **Zheng, S., Tang, H., Han, Z. & Zhang, Y.** (2006). Controller design for vehicle stability enhancement, *Control Engineering Practice*, 14 (12), 1413–1421.
- [89] **Choi, S. & Cho, D.W.** (2001). Design of nonlinear sliding mode controller with pulse width modulation for vehicular slip ratio control, *Vehicle System Dynamics*, 36 (1), 57–72.
- [90] **National Highway Traffic Safety Administration** (2007). *FMVSS No.126 Electronic stability control systems, Final Regulatory Impact Analysis*. USA: U.S. Department of Transportation.

## CURRICULUM VITAE



**Name Surname:** Mümin Tolga EMİRLER

**Place and Date of Birth:** Istanbul, November 4, 1983

**E-Mail:** tolgaemirler@yahoo.com

**B.Sc.:** Mechanical Engineering, Istanbul Technical University

**B.Sc.:** Manufacturing Engineering (Double Major), Istanbul Technical University

**M.Sc.:** Mechatronics Engineering, Istanbul Technical University

### List of Publications and Patents:

- **Emirler, M.T.**, Kahraman, K., Şentürk, M., Aksun Güvenç, B., Güvenç, L. & Efendioğlu, B. (2013). Vehicle yaw rate estimation using a virtual sensor, *International Journal of Vehicular Technology*, Article ID 582691, doi:10.1155/2013/582691, (No APC paid).
- Güvenç, L., Uygan, I.M.C, Kahraman, K., Karahmetoğlu, R., Altay, İ, Şentürk, M., **Emirler, M.T.**, Karcı Hartavi, A.E., Aksun Güvenç, B., Altuğ, E., Turan, M.C., Taş, Ö.Ş, Bozkurt, E., Özgüner, Ü, Redmill, K., Kurt, A. & Efendioğlu, B. (2012). Cooperative adaptive cruise control implementation of Team Mekar at the grand cooperative driving challenge, *IEEE Transactions on Intelligent Transportation Systems*, 13 (3), 1062–1074.
- Demirel, B., **Emirler, M.T.**, Sönmez, Ü. & Yörükoğlu, A. (2010). Semicompliant force generator mechanism design for a required impact and contact forces, *ASME Transactions on Journal of Mechanisms and Robotics*, 2 (4).
- Kahraman, K., **Emirler, M.T.**, Şentürk, M., Aksun Güvenç, B., Güvenç, L. & Efendioğlu, B. (2010). Estimation of vehicle yaw rate using a virtual sensor with a speed scheduled observer. *Proceedings of the 6th IFAC Symposium Advances in Automotive Control*, (pp.632–637). Munich, Germany, June 12-14.
- **Emirler, M.T.**, Kahraman, K., Aksun Güvenç, B., Güvenç, L. & Efendioğlu, B. (2009). Estimation of road vehicle yaw rate using a virtual sensor and an observer, *European Control Conference (ECC 2009)*, Budapest, Hungary, August 23-26.
- Demirel, B., **Emirler, M.T.**, Yörükoğlu, A., Koca, N. & Sönmez, Ü. (2008). Compliant impact generator for required impact and contact force, *Proceedings of the ASME International Mechanical Engineering Congress and Exposition (IMECE 2008)*, (pp.373–379). Boston, Massachusetts, USA, October 31 - November 6.
- **Emirler, M.T.**, Uygan, I.M.C., Gelbal, Ş.Y., Gözü, M., Böke, T.A., Aksun Güvenç, B. & Güvenç, L. (2014). Vehicle dynamics modelling and validation for

a hardware-in-the-loop vehicle simulator (in Turkish), *7th Automotive Technologies Congress (OTEKON)*, Bursa, Turkey, May 26-27.

- Şentürk, M., **Emirler, M.T.**, Kahraman, K., Aksun Güvenç, B., Güvenç, L. & Efendioğlu, B. (2010). Road vehicle virtual yaw rate sensor application (in Turkish), *5th Automotive Technologies Congress (OTEKON)*, Bursa, Turkey, June 7-8.
- **Emirler, M.T.**, Şentürk, Kahraman, K., M., Aksun Güvenç, B., Güvenç, L. & Efendioğlu, B. (2009). Estimation of road vehicle yaw rate using a virtual sensor (in Turkish), *Turkish Annual Meeting on Automatic Control (TOK 2009)*, Istanbul, Turkey: Yıldız Technical University, October 13-16.
- Efendioğlu, B., **Emirler, M.T.**, Şentürk, Kahraman, K., M., Aksun Güvenç, B. & Güvenç, L. (2009). Virtual yaw rate sensor design using Matlab-Simulink, *14th Conference for Computer-Aided Engineering and System Modeling*, Ankara, Turkey: Middle East Technical University, November 5.

## PUBLICATIONS/PRESENTATIONS ON THE THESIS

- **Emirler, M.T.** & Aksun Güvenç, B. (2014). Robust DC motor speed control using parameter space approach and add-on disturbance observer, *submitted, under review*.
- **Emirler, M.T.**, Kahraman, K., Şentürk, M., Acar, O.U., Aksun Güvenç, B., Güvenç, L. & Efendioğlu, B. (2015). Lateral stability control of fully electric vehicles, *International Journal of Automotive Technology*, 16, (2), 317–328.
- **Emirler, M.T.**, Uygan, I.M.C., Aksun Güvenç, B. & Güvenç, L. (2014). Robust PID steering control in parameter space for highly automated driving, *International Journal of Vehicular Technology*, Article ID 259465, doi:10.1155/2014/259465, (No APC paid).
- **Emirler, M.T.**, Uygan, I.M.C., Altay, İ, Acar, O.U., Keleş, T., Aksun Güvenç, B. & Güvenç, L. (2013). A cooperating autonomous road vehicle platform. *Proceedings of the IFAC Workshop on Advances in Control and Automation Theory for Transportation Applications (ACATTA 2013)*, 1, (pp.194–201). Istanbul, Turkey: Istanbul Technical University, September 16-17.
- **Emirler, M.T.**, Aksun Güvenç, B. & Güvenç, L. (2013). Communication disturbance observer approach to control of integral plant with time delay. *Proceedings of the 9th IEEE Asian Control Conference (ASCC 2013)*, (pp.1–6). Istanbul, Turkey, June 23-26.
- Kahraman, K., Şentürk, M., **Emirler, M.T.**, Bozkurt, E., Aksun Güvenç, B., Güvenç, L. & Efendioğlu, B. (2012). Offline and hardware in the loop simulation model-system development for electronic stability control of a fully electric vehicle, *6th Automotive Technologies Congress (OTEKON)*, Bursa, Turkey: Uludağ University, June 4-5.
- **Emirler, M.T.**, Kahraman, K., Şentürk, M., Acar, O.U., Aksun Güvenç, B., Güvenç, L. & Efendioğlu, B. (2011). Integrated lateral stability control for fully electric vehicles, *9th European Workshop on Advanced Control and Diagnosis (ACD 2011)*, Budapest, Hungary, November 17-18.